UC-427

BEHAVIOR OF THE REVERSED FIELD PINCH WITH NONIDEAL BOUNDARY CONDITIONS

Yung-Lung Ho

DOE/ER/53212-131

November 1988

NOTICE

Printed in the United States of America
Available from
National Technical Information Service
U.S. Department of Commerce
5285 Port Royal Road
Springfield, VA 22161

NTIS Price codes
Printed copy: A07
Microfiche copy: A01

BEHAVIOR OF THE REVERSED FIELD PINCH WITH NONIDEAL BOUNDARY CONDITIONS

by

Yung–Lung Ho

A thesis submitted in partial fulfillment of the
requirements for the degree of

Doctor of Philosophy
(physics)

at the
University of Wisconsin – Madison
1988

BEHAVIOR OF THE REVERSED FIELD PINCH WITH NONIDEAL BOUNDARY CONDITIONS

Yung–Lung Ho

Under the supervision of Professor Stewart C. Prager

The linear and nonlinear magnetohydrodynamic stability of current-driven modes are studied for a reversed field pinch with nonideal boundary conditions. The plasma is bounded by a thin resistive shell surrounded by a vacuum region out to a radius at which a perfectly conducting wall is situated. The distant wall and the thin shell problems are studied by removing either the resistive shell or the conducting wall.

Linearly, growth rates of tearing modes and kink modes are calculated by analytical solutions based on the modified Bessel function model for the equilibrium. The effects of variation of the shell resistivity and wall proximity on the growth rates are investigated. The modes that may be important in different parameter regimes and with different boundary conditions are identified. These results then help to guide the nonlinear study, and also help to interpret the quasilinear aspect of the nonlinear results.

The nonlinear behaviors are studied with a three-dimensional magnetohydrodynamics code. The fluctuations generally rise with increasing distance between the conducting wall and the plasma. The enhanced fluctuation induced $\mathbf{v} \times \mathbf{b}$ electric field primarily oppose toroidal current; hence, loop voltage must increase to sustain the constant. If the

loop voltage is held constant, the current decreases and the plasma evolves toward a nonreversed tokamak-like state. Quasilinear interaction between modes typically associated with the dynamo action is identified as the most probable nonlinear destabilization mechanism.

The helicity and energy balance properties of the simulation results are discussed. The interruption of current density along field lines intersecting the resistive shell is shown to lead to surface helicity leakage. This effect is intimately tied to stability, as fluctuation induced $\mathbf{v} \times \mathbf{b}$ electric field is necessary to transport the helicity to the surface. In this manner, all aspects of helicity balance, i.e., injection, transport, and dissipation, are considered self-consistently. The importance of the helicity and energy dissipation by the mean components of the magnetic field and current density is discussed.

Approved:

Date

Professor Stewart C. Prager
Department of Physics

Acknowledgment

First of all, I would like to thank all the people who helped me stay in physics. May your spouse, sons, daughters, and two generations of grand children all become physicists. I would especially like to thank Dr. Prager; this research would not be possible without his support and foresight. Also, I thank John Sarff for useful discussions, my fellow graduate students who always kept my spirit up, and Amy for her help with the figures. In addition, I am grateful to Dr. Schnack who generously provided his excellent 3D MHD code for use in this research. The contributions of the readers on my thesis committee (in particular, Dr. Callen) should also be mentioned; this thesis greatly benefited from their suggestions. Finally, I would like to treat all the people mentioned above to dinner. Well,...maybe not!

This research was financially supported by the U. S. Department of Energy.

Contents

Chapter 1
INTRODUCTION

1.1 MOTIVATION

The reversed field pinch (RFP) has been the subject of substantial theoretical and experimental investigation for many years. Early experiments on devices based on the pinch effect (in which the plasma is compressed by the magnetic field generated by currents carried by the plasma itself) were motivated by simplicity. Stability problems of these early devices led eventually to the developments of the RFP and the tokamak. Theoretically, it was noted early on that reversal of the toroidal field (hence the name "reversed field" pinch) could stabilize the pinch[1]. Since then, experiments have demonstrated spontaneous self-generation and sustainment of such a reversed field by the plasma. The fascinating mechanism behind this effect, called the "dynamo[2]" (in analogy to the astrophysical and the geomagnetic dynamo[3]), motivated much of the subsequent theoretical work. The majority of these works showed that nonlinear interaction of magnetohydrodynamic (MHD) instabilities with the equilibrium is sufficient to produce the dynamo effect[4,5,6,7,8]; however, kinetic effects have also been suggested as a possible cause[9]. The complete solution may include a composite of the two effects. Our investigation expands on the body of MHD theories.

Most RFP experiments and theories of the dynamo have, until recently, included a highly conducting wall near the plasma surface. Such

a boundary is necessary for linear MHD stability[10] (even with field reversal), for the minimum energy "Taylor state[11]", and perhaps for the dynamo. Generalizing the boundary condition is useful to elucidate the essential physics ingredients of RFP sustainment. Moreover, the ability to confine a plasma with a resistive boundary and/or a conducting wall that is separated from the plasma surface is of great practical importance to the operation of an RFP. The work presented here may also lead to a better understanding of the dynamo effects occurring in nature, and nonlinear behavior of MHD instabilities in general.

1.2. BRIEF DESCRIPTION OF A REVERSED FIELD PINCH

The RFP is an axisymmetric, toroidal magnetic fusion device similar to the tokamak[12], and the spheromak[13]. The plasma is confined by a toroidal magnetic field and a poloidal magnetic field generated by toroidal plasma currents. Although tokamaks have achieved the best parameters for controlled thermonuclear fusion, the RFP is at a relatively early stage of development, but potentially offers some practical advantages. Unlike tokamaks, the ratio of the toroidal current to the toroidal magnetic field is relatively high in an RFP. Stability is achieved mainly through strong shear in the magnetic field, which appears to suffice even at relatively high β (=plasma pressure/magnetic field energy density). These differences may lead to a more efficient reactor in terms of heating, reactor size, and utilization of the externally applied magnetic field.

The strong shear necessary for RFP stability is equivalent to the

condition that the toroidal field reverses sign. The poloidal current necessary to sustain the strong shear arises from a combination of paramagnetic[14], and dynamo effects. However, the paramagnetic effect alone cannot cause reversal; thus, dynamo action is essential for the existence of the RFP state. The dynamo is most likely the dissipative dynamical process by which the plasma relaxes towards the "Taylor state[11]". Experimental RFP states are not fully relaxed, but are close enough to exhibit much of the macroscopic features of the Taylor state (which includes reversal). Although most of the fundamental topics are still being scrutinized, several review articles exists and should be referred to for additional background on the RFP[15,16,17]. As stated earlier, most of the research (and hence literature) on RFP's to date include a close-fitting perfectly conducting boundary.

1.3. THE BOUNDARY CONDITION PROBLEM / THESIS TOPIC

Next generation long pulse RFP experiments, such as the upcoming ZT-H[18] (as well as a reactor) will operate with a shell that has a magnetic field penetration time much shorter than the plasma lifetime. This "thin shell problem" is now being experimentally studied in the OHTE[19], HBTX-1C[20], and the Reversatron[21] devices. In particular, experiments on OHTE have demonstrated the possibility of operation with a resistive shell. Of similar practical import is the determination of the required proximity of the conducting wall to the plasma surface (the "distant wall problem"). Experiments in HBTX-1B[22] displayed an anomalous increase

in the toroidal loop voltage, V_L, with the insertion of limiters. The rise in V_L shortens the possible pulse length of the experiments. The new device at Wisconsin (MST[23]) will also investigate this problem as one of its main objectives.

1.4. RESEARCH APPROACH AND THESIS OUTLINE

We study both the thin shell and the distant wall problems using resistive MHD models. The use of MHD models to describe macroscopic phenomena in toroidal fusion devices is well-established. For the RFP, MHD models have accounted for the observed magnetic fluctuation energy spectrum[24], and resistive MHD codes have successfully simulated the RFP sustaining "dynamo"[7].

The plasma in our model is bounded by a thin resistive shell at minor radius $r = a$, which is itself surrounded by an outer perfectly conducting wall at $r=r_w$; a "vacuum" region of width r_w-a separates the resistive shell and conducting wall. The thin shell problem and the distant wall problem can both be studied by removing either the outer conductor or the resistive shell. Similar physics dominates each case. The resistive shell presumably affects only the time evolution, not the final state.

In the absence of a large surrounding vacuum, cylindrical theories are adequate[15] for RFP plasmas, and are typically used. We also use the cylindrical approximation, but must additionally assume that, for the thin shell problem, the outer conducting wall can be considered effectively

removed when r_w is large but does not yet approache the major radius R. Otherwise, cylindrical vacuum solutions for the region $a < r < r_w$ are inadequate. This simplification implies that cylindrical thin shell effects are minimally affected by toroidicity. Possible thin shell instabilities that exist only in the toroidal geometry, such as the tilt mode[25], are not considered in this thesis.

A force-free assumption is used throughout this thesis. It is valid for low β plasmas, and is widely used in simulations of the "dynamo"[7]. Moreover, since pressure-driven interchange modes are radially localized, they should be relatively unaffected by boundary condition variations.

Both linear and nonlinear results are presented in this thesis. The linear results (Chapter 2) illustrate detailed calculations of the influence of the proximity and resistance of the boundary on stability and growth rates for realistic equilibria. The goal is to estimate what modes might become important as the boundary condition is varied. An accurate determination of the growth rate, which is neither possible nor meaningful since most instabilities tend to exist in a nonlinearly saturated state in typical RFPs, is not sought. The linear instability regime results are used for comparison with experiment and interpretation of nonlinear computations.

A three-dimensional MHD code is used for the nonlinear computations (Chapter 3). These calculations are necessary since the MHD behavior of an RFP, indeed "dynamo" sustainment itself, is known to be robustly nonlinear. The plasma generally evolves to state of enhanced

fluctuations with increasing conducting wall radius. The increased amplitude of these modes yields an increase in the induced electric field, given by $\mathbf{v} \times \mathbf{b}$. The electric field, which ordinarily produces the dynamo effect with a close-fitting conducting boundary, reduces the toroidal current as the amplitude increases. Thus, an increase in the applied V_L is necessary to maintain a constant toroidal current. In the absence of a conducting wall (the thin-shell problem), these results cast doubt on whether the plasma could be maintained in a steady state.

The principal destabilizing mechanism that prevents the instabilities from nonlinearly saturating at a low amplitude is probably quasilinear mode coupling of $m = 1$, $n < 0$ modes. This is inferred from the result of nonlinear simulations with only a single mode present (quasilinear effect). We also investigate quasilinear effects of other nonideal boundary modes. In general, all the modes are found to reduce the toroidal current. Preliminary comparison with experimental results, and summaries of the key nonlinear results are included in the summary and discussion section at the end of Chapter 3.

In the final chapter (Chapter 4), we discuss the helicity balance properties of our model. This is compared with other models of RFP behavior based on the helicity balance. Better understanding of the helicity balance may lead to much simpler models of plasma behavior.

The physical mechanisms identified here should exist under realistic experimental conditions. However, a comprehensive understanding of how various elements of our results scales with the key parameters,

(plasma resistivity, viscosity, current,...etc.,) will require the completion of more thorough computational scans through the parameter space. Nevertheless, we can gain significant insights through physical considerations and scaling arguments based on the MHD equations. These arguments, suggestions for experiments, and other possible future endeavors will also be discussed in Chapter 4.

Finally, Chapter 5 briefly summarizes the major conclusions of this research.

REFERENCES

[1]M. N. Rosenbluth in *Proceedings of the 2nd International Conference on Peaceful uses of Atomic Energy,* 1958, Vol 31, p. 85.

[2]E. J. Caramana and D. A. Baker, Nucl. Fusion **24**, 423 (1984).

[3]H. K. Moffatt, *Magnetic Field Generation in Electrically Conducting Fluids* (Cambridge Univ. Press, Cambridge 1978).

[4]A. Sykes and J. A. Wesson, in *Proceedings of the 8th European Conference on Controlled Fusion and Plasma Physics,* Prague (Czechoslovak Academy of Science, Prague, 1977), Vol, 1, p. 80.

[5]A. Y. Aydemir and D. C. Barnes, Phys. Rev. Lett. **52**, 930 (1984).

[6]H. R. Strauss, Phys. Fluids **27**, 2580 (1984).

[7]A. Y. Aydemir, D. C. Barnes, E. J. Caramana, A. A. Mirin, R. A. Nebel, D. D. Schnack, and A. G. Sgro, Phys. Fluids **28**, 898 (1985).

[8]A. Bhattacharjee and E. Hameiri, Phys. Rev. Lett. **57**, 206 (1986).

[9]A. R. Jacobson and R. W. Moses, Phys. Rev. A **29**, 3335 (1984).

[10]D. C. Robinson, Nucl. Fusion **18**, 939 (1978).

[11]J. B. Taylor, Rev. Mod. Phys. **58**, 741 (1986).

[12]H. P. Furth, Nucl. Fusion **15**, 487 (1975).

[13]M. N. Rosenbluth and M. N. Bussac, Nucl. Fusion **19**, 489 (1979).

[14]S. C. Prager and L. Turner, Phys. Fluids **28**, 1155 (1985).

[15]H. A. B. Bodin and A. A. Newton, Nucl. Fusion **20**, 1255 (1980).

[16]H. Dreicer, Physica Scripta **T2/2**, 435 (1982).

[17]H. A. B. Bodin, Nuclear Instruments and Methods **207**, 1 (1983).

[18]H. Dreicer, in *Physics of Mirrors, Reversed Field Pinches and Compact Tori*, Proceedings of the International School of Plasma Physics Course and Workshop, Varenna, Italy, 1987, Vol. I, edited by S. Ortolani and E. Sindoni (Società Italiana di Fisica, Bologna, 1988), p. 359.

[19]T. Tamano, W. D. Bard, C. Chu, Y. Kondoh, R. J. La Haye, P. S. Lee, M. T. Saito, M. J. Schaffer, and P. L. Taylor, Phys. Rev. Lett. **59**, 1444 (1987).

[20]B. Alper, in *Proceedings of the IEEE International Conference on Plasma Science*, Seattle, 1988 (IEEE, New York, 1988), paper 5P17.

[21]S. Robertson and P. Schmid, Phys. Fluids **30**, 884 (1987).

[22]B. Alper and H. Y. W. Tsui, in *Proceedings of the 14th European Conference on Controlled Fusion and Plasma Physics*, Madrid, 1987 (European Physical Society, Budapest, 1987), Vol. II, p. 434.

[23]R. N. Dexter, D. W. Kerst, T. W. Lovell, S. C. Prager, and J. C. Sprott, Bull. Am. Phys. Soc. **29**, 1332 (1984).

[24]P. Kirby, Phys. Fluids **31**, 625 (1988).

[25]S. C. Jardin, M. S. Chance, R. L. Dewar, R. C. Grimm, and D. A. Monticello, Nucl. Fusion **21**, 1203 (1981).

Chapter 2
LINEAR STABILITY

2.1. INTRODUCTION

In this chapter, we illustrate detailed results on the influence of the proximity and resistance of the boundary on the stability of realistic equilibria. The goal is to estimate which modes might become important as the boundary condition is varied. The results are used for comparison with experiment and interpretation of nonlinear computations.

In general, MHD unstable configurations cannot be fully stabilized by introducing walls of finite electrical conductivity[1,2]. However, evaluation of growth rates is useful to assess whether a mode will arise during an experimental lifetime. Much of the previous growth rate calculations with a thin resistive shell employed skin-current pinch configurations[3,4]. Nonresonant modes (modes with $-m/n \neq q(r)$ for $0 < r < a$, where q is the inverse of the field line pitch, m and n are poloidal and toroidal mode numbers respectively) dependent on a conducting shell for stability were shown to grow on the shell resistive time scale $\tau_s = \mu_0 a \Delta / \eta_s$, where Δ is the thickness of the shell, and η_s is the shell resistivity. For modes weakly dependent on τ_s, growth rates can be greater than $a\pi^2/\Delta\tau_s$ and the shell thickness cannot be ignored[5]. Resonant instabilities were included in a study using the resistive high beta ($\beta = 30\%$ on axis) pitch-and-pressure model (PPM)[6] and a thick shell approximation. Rotational effects were studied in Refs. 1 and 7.

In the present calculation, we describe the equilibrium by the force-free modified Bessel function model[8] (MBFM). This model approximates reasonably well the experimental profiles[9] and the final states of force-free numerical simulations[10] with a conducting boundary. Thus, for the purpose of comparison with both the experiments and numerical results, the MBFM is an appropriate model to use as a starting point when considering additional effects due to a resistive shell.

The thin-shell approximation is found to be appropriate here for modes of interest. It is only violated for equilibrium profiles that are unstable or nearly unstable to ideal modes in the presence of a close-fitting conducting wall. For the MBFM profiles used here, these modes do not occur in the range of expermental interest.

The approach we use is to extend the Δ' analysis of tearing modes[11,12] to include a thin resistive shell and vacuum region between the shell and a perfectly conducting wall. The basic equations and the equilibrium model are described in Sec. 2.2. We also introduce an additional staircase approximation that allows analytical solutions. This also avoids the usual numerical singularity problem at tearing surfaces. Similar approximations have been used for stability analyses of tokamaks[13]. Results are presented in Sec. 2.3 and Sec. 2.4. Since $m > 1$ modes remain stable regardless of the boundary condition for realistic equilibrium profiles, we only present results for $m = 0$ and $m = 1$. A summary of the linear instability results and discussion of its experimental relevance are included in Section 2.5.

2.2. MODEL DESCRIPTION

a. Initial equilibrium

The equilibrium, depicted in Fig. 2.1, is that of a one-dimensional cylinder in which the plasma surface at $r = a$ is bounded by a resistive shell. The shell is surrounded by a vacuum region which extends to radius $r = r_w$ at which a perfectly conducting wall is situated. Our model ignores resistivity away from tearing surfaces. This implies that magnetic flux frozen into the plasma could not penetrate the resistive shell unless we additionally take into account plasma resisitivity at the surface[4,5]. For this reason, an infinitessimally thin vacuum region is inserted between the plasma and resistive shell as the simplest mean of simulating the high edge resistivity present in experiments.

The plasma equilibrium considered is force-free and described by $\nabla \times \mathbf{B} = \lambda \mathbf{B}$, where $\mathbf{B}$ and λ depend on radius r only. This λ is taken to be a spacial constant at $\lambda = \lambda_o$ for $r < r_b$ and decreases linearly to zero from $r = r_b$ to $r = a$ [the so-called Modified Bessel Function Model, (MBFM)], as shown in Fig. 2.1. The relationship between the breakpoint radius r_b and λ_o can be determined from the relationship between the reversal parameter F and the pinch parameter Θ, where $F = B_z(a) / \langle B_z \rangle$, $\Theta = B_\theta(a) / \langle B_z \rangle$, B_θ and B_z are the poloidal and axial equilibrium magnetic field, and $\langle\ \rangle$ denotes a volume average. Using experimentally determined F-Θ curves[8], this model has the following properties:

(i) For $\lambda_o a \leq 2.4$, the model is identical to the Bessel Function Model (BFM) where λ is constant out to $r = a$ and Θ varies from 0 to 1.2.

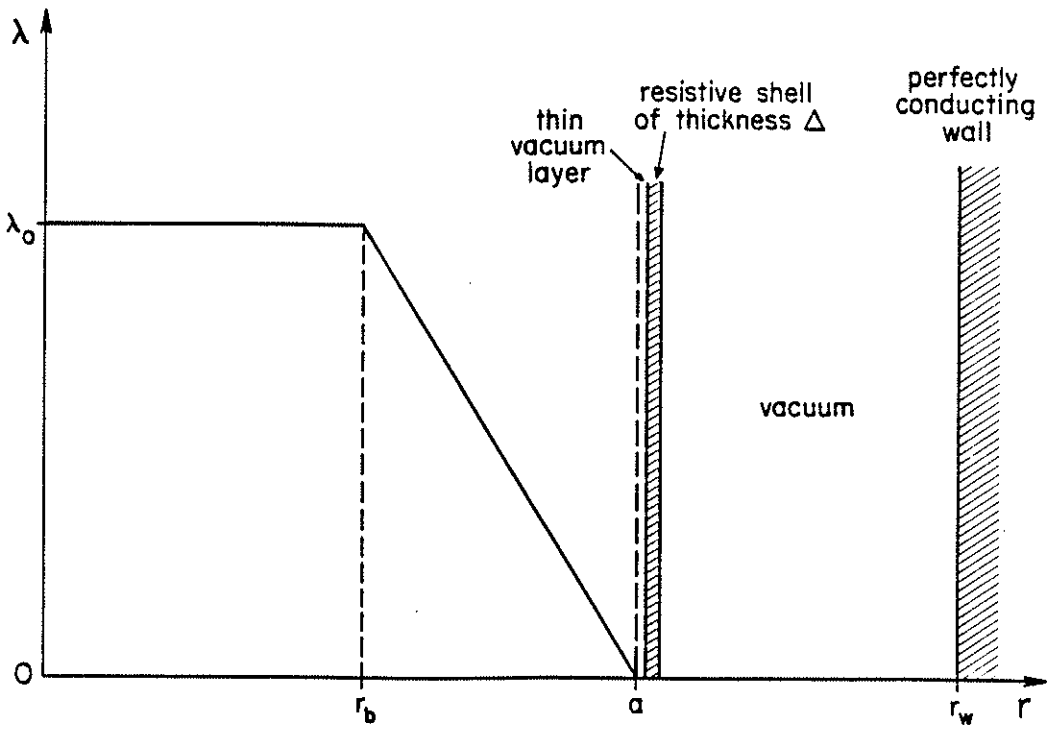

Fig. 2.1. Equilibrium model with Modified Bessel Function Model λ profile, resistive shell, vacuum regions and conducting wall.

(ii) For $2.4 < \lambda_o a <\sim 3.84$, as $\lambda_o a$ increases toward its maximum value, F decreases to -1.223 and Θ increases to 2.546; r_b decreases linearly from $r_b = a$ at $\lambda_o a = 2.4$ to $r_b = 0.446a$ at $\lambda_o a = 3.84$.

(iii) For $3.84 < \lambda_o a < 5$, increasing $\lambda_o a$ leads to increasing F and decreasing Θ with r_b decreasing linearly to zero at $\lambda_o a = 5$.

Although the above model includes $\lambda_o a$ from 0 to 5, the typical experimental steady-state parameter Θ is between 1.4 and 2.0, which corresponds to $\lambda_o a = 2.75$ to 3.4. Both the resistivity η and mass density ρ are assumed to be constant for simplicity.

b. Equations for growth rates and eigenfunctions

The equations used are de-dimensionalized by writing time in units of the resistive diffusion time $\tau_R = a^2\mu_o/\eta$, the magnetic induction in units of the characteristic field B_o, and r in terms of a. The equation for the perturbed radial magnetic field, b_r, within the plasma is[14]

$$(rb_r)'' + \frac{1}{r}\frac{m^2 - k^2r^2}{m^2 + k^2r^2}(rb_r)' + \left(\lambda^2 - k^2 - \frac{m^2}{r^2} + \frac{2km\lambda}{m^2 + k^2r^2}\right)rb_r - \frac{mB_z - krB_\theta}{f}\lambda' b_r = 0, \qquad (2.1)$$

where k is the Fourier mode number in the z direction, $f = (mB_\theta/r) + kB_z$, and the prime $= \partial/\partial r$. Solutions on either side of a tearing resonant surface (where $f = 0$) are matched by the jump condition[11,15]

$$[\, b_r'/b_r \,] \approx (\gamma/.55)^{5/4} S^{-1/2} f'^{-1/2}, \qquad (2.2)$$

where [ ] denotes a jump across the surface, γ is the growth rate, $S = \tau_R/\tau_{A\theta}$,

and $\tau_{A\theta}$ is the poloidal Alfvén transit time [$= a(\mu_o\rho)^{1/2}/B_o$]. The plasma solution is matched to the vacuum solution by replacing the resistive shell with the jump condition[4]

$$\left[b_r'/b_r \right] = \gamma \tau_s. \tag{2.3}$$

For the vacuum region outside the shell, we use the radial component of the Bessel function solutions to the equation $\nabla \times \mathbf{b} = 0$.

Equation (2.1) can be derived from the linear force-free condition, $\mathbf{j} \times \mathbf{B} + \mathbf{J} \times \mathbf{b} = 0$ ($\mathbf{j}$ and $\mathbf{J}$ are the perturbed and equilibrium current densities), which neglects plasma inertia. The force-free assumption is valid for modes with growth times much longer then the Alfvén time (i.e., $\gamma \ll S$ in dimensionless units).

Equation (2.2) is based on the $\eta^{3/5}$ scaling of tearing modes[12]. It implies the constant ψ approximation used in Ref. 12, large S, and γ on the order of $S^{2/5}$. For resonant modes with stability characteristics dependent on the presence of a conducting wall, a range of ordering schemes [η^0 (resonant ideal modes), $\eta^{1/3}$ (resistive kink modes),...] is possible depending on the values of τ_s and r_w[1,11]. We generally use tearing ordering and then check for self-consistency.

The thin shell approximation used in Eq. (2.3) is valid for $\Delta\,[k^2 + (m/a)^2]^{1/2} \ll 1$ and $\gamma \ll a\pi^2/4\Delta\tau_s$ (see Appendix). Here, $4\Delta\tau_s\,/a\pi^2$ is the characteristic L / R decay time of radial inhomogeneities of induced eddy currents in the slab limit ($a \gg \Delta$). In this approximation, the eddy current distribution in the shell is approximately constant with radius.

Although the use of the thin shell approximation and the neglect of

inertia precludes the calculation of γ for modes ideally (resonant or nonresonant) unstable even with a close fitting conducting wall (γ on the order of S and weak resistive effects), Eq. (2.1) can be straight forwardly used to identify these modes by the usual Newcomb method[17]. Modes that may become ideally unstable with a distant conducting wall ($r_w > a$) as $\tau_s \rightarrow 0$ can be similary identified using Newcomb's method by setting $\tau_s = 0$ in the thin-shell matching condition [Eq. (2.3)]. However, for these modes, as r_w increases and τ_s decreases, γ would generally increase and begin to approach S in our calculation; in which case, the calculated γ becomes invalid. Hence, Newcomb's method is not additionally needed, unless one is interested in precisely when a mode becomes mathematically defined as ideal. Physically, the crossover point is imprecise.

For modes near marginal stability, Eq. (2.2) (and many other approximations) cannot be used to estimate γ. This is not a problem since these modes are, by definition, unimportant.

c. Staircase approximation

To facilitate solving Eq. (2.1) analytically, we introduce the step-like λ profile shown in Fig. 2.2 to approximate the MBFM profile. The λ' term in Eq. (2.1) can now be set to zero, and the solution satisfies $\nabla \times \mathbf{b}_i = \lambda_i \mathbf{b}_i$ in the i^{th} step. Besides having well known solutions[16], this configuration can be easily modified to include multiple resistive shells and thick vacuum layers inside the resistive shell.

One additional matching condition now becomes necessary at each of

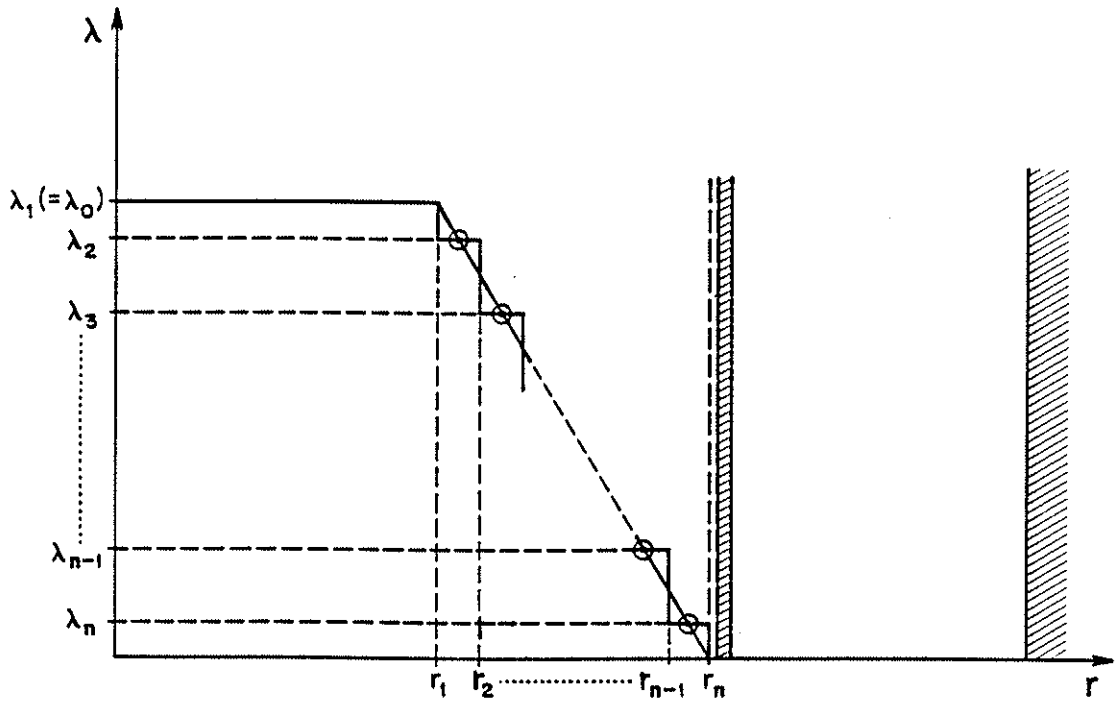

Fig. 2.2. Staircase approximation to the original model in Fig.1. All steps at $r > r_1$ have equal width.

the λ profile discontinuities. By matching b_z and b_θ at the perturbed surfaces[4], using the continuity of b_r, and assuming incompressibility and ideal motion [$\partial \mathbf{b}/\partial t = \nabla \times (\mathbf{v} \times \mathbf{B})$], we obtain

$$\left[b_r'/b_r \right] = (\lambda_{i+1} - \lambda_i) \{(m/r)B_z - kB_\theta\} / f. \tag{2.4}$$

Assumptions used for the derivation of Eq. (2.4) [incompressibility and ideal motion (i.e., $\gamma \gg 1$) away from tearing surfaces] were also utilized in obtaining Eq. (2.2). Thus, for resonant modes the use of the step model imposes no additional constraint beyond the necessity for it to be an accurate representation of the original MBFM. The incompressible assumption does not affect stability[14]. Moreover, for the relatively slow growing modes in low β plasmas considered, the assumption should minimally affect instability growth rates[11].

The infinite λ' exerts strong influences on the stability properties of modes resonant near each jump in λ. This produces spurious localized modes not present in continuous λ models. Thus in the tapered λ region, the growth rate is calculated only for modes whose resonant surfaces are located on the flat portion of each λ step at the point of intersection with the original MBFM profile (i.e., at circled points of Fig. 2.2). The step approximation essentially group all λ' effects within a step width into a single jump. For the circled points, all the λ' influences that were on one side of the resonant surface in the continous λ model remain on that same side after switching to the step model. Thus, not surprisingly, the least amount of errors are introduced for these points. For $m \geq 1$, the staircase model implies that the k spectrum of resonant modes become discretized.

For $m = 0$, where all k modes are resonant at the same location, the $\lambda_o a$ parameter specifying the equilibrium becomes discretized. Thus, we require enough steps to accomodate all k and $\lambda_o a$ values of interest. Convergence tests are performed to insure that no additional information can be obtained by increasing the number of steps. The localized modes, requiring finer step-size, determines the minimum number of steps required. In general, 20 steps are used for the results shown here.

The usual method utilized to solve Eq. (2.1) is numerical, where one recasts the equation into a finite difference form and applies the shooting method. Upon reexamination of Eq. (2.4) we find it to be similar to the finite differenced form of the λ' term in Eq. (2.1). Hence, our method can be considered partially numerical. As for the resonant modes for which growth rates were calculated, in numerical terms they tend to have solutions that converge most rapidly with decreasing spacial grid size.

The sign of the right-hand-side of Eq. (2.4) near resonant surfaces where $f = 0$ is easily determined for typical RFP profiles. In general, negative $\lambda_{i+1} - \lambda_i$ just outside a resonant surface contributes positively to the growth rates of $m = 0,1$ modes. Just inside the resonant surface, f changes sign and the opposite is true. A BFM plasma (and MBFM plasmas that have $\Theta < 1.2$) with a vacuum region (single $\Delta\lambda$ jump at r=a) would therefore be extremely unstable for modes resonant near the plasma surface. This is an expectedly unrealistic result obtained by using an unrealistic λ profile.

For nonresonant modes, Eq. (2.2) does not apply and the original

continuous λ model is not restricted to $\gamma \gg 1$ regimes. The staircase model is similarly unrestricted, even though Eq. (2.4) is applicable only for $\gamma \gg 1$. The reason is that γ depends only on $1/\tau_S$ for such modes. Hence evaluation of the growth rate in terms of $1/\tau_S$ can be done using any τ_R we choose, including ones for which Eq. (2.4) is valid, and the answer would apply for all τ_R.

2.3. RESULTS FOR m = 1

We will treat three types of modes that are likely of experimental interest: resistive tearing modes resonant inside the reversal surface ($+B_z$ tearing modes), tearing modes resonant outside the reversal surface ($-B_z$ tearing modes) and external kink modes (resonant in vacuum). Stability boundaries are indicated in the plots of Fig. 2.3, in which the shaded areas are unstable. For purpose of discussion, the parameter space of Fig. 2.3 can be divided into four regions [cf., Fig. 2.3(b)]. In the range of experimental interest, regions (I), (II) and (III) correspond primarily to $+B_z$ tearing modes, external kink modes and $-B_z$ tearing modes respectively. For each region and corresponding mode type, we examine the dependence of stability boundaries on conducting wall location [Figs. 2.3(a)–2.3(c)], and the dependence of growth rates on the wall location and penetration time τ_S (Figs. 2.4 - 2.9). For the growth rate calculations, we include $\lambda_o a = 3.5$ ($\Theta \approx 2.2$) cases although typical experiments operate with lower Θ. This permits the behavior of the $+B_z$ tearing modes, which are stable at lower Θ in our model but are present in experiments[18], to be examined.

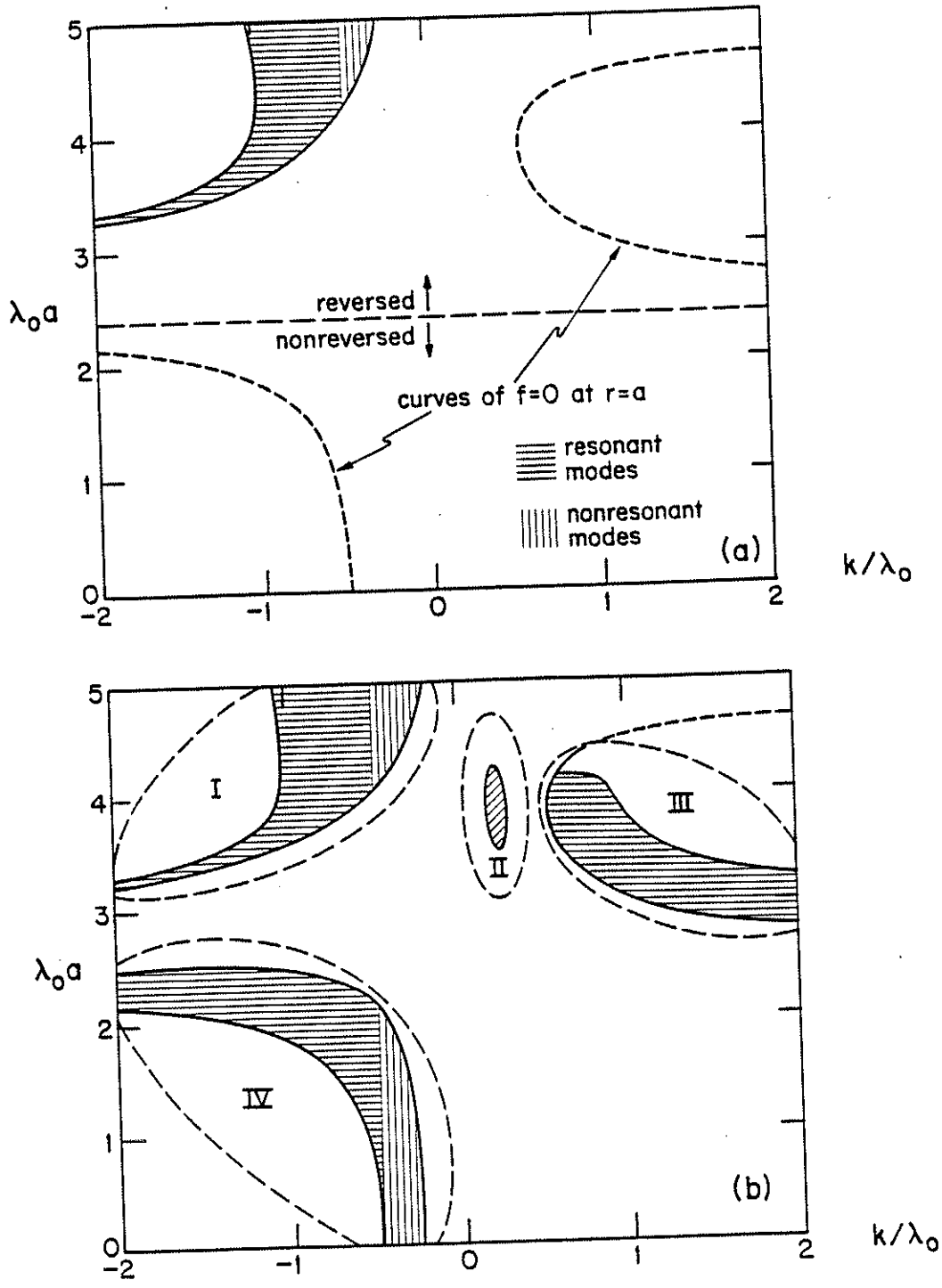

(Fig. 2.3 cont. on next page)

(Fig. 2.3 cont.)

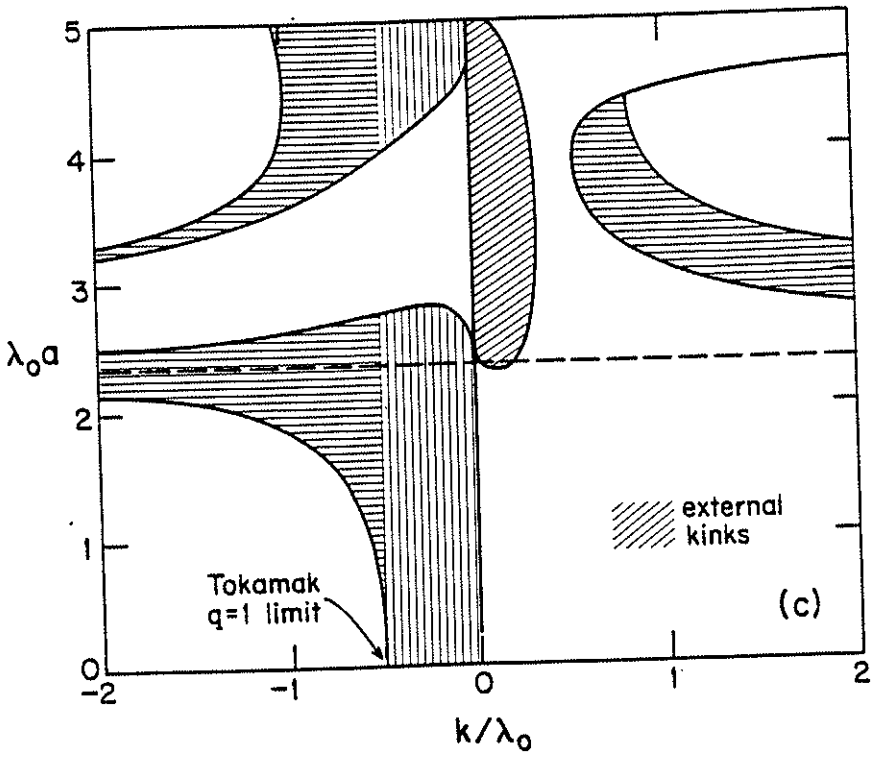

Fig. 2.3. The m = 1 stability diagram in parameter space $\lambda_o a$ versus k/λ_o (= na/R), where λ_o is the value of $\lambda = J_{||}/B$ in the constant region (cf. Fig. 2.1). Unstable regions are shown shaded for the cases: (a) close-fitting conducting wall, (b) 40% vacuum thickness [= $(r_w-a)/a$], and (c) 1900% vacuum (effectively no conducting wall). Figure 2.3(b) also identifies the four regions discussed in the text. Resonant, nonresonant, and external kink modes are indicated by horizontal, vertical and slanted lines, respectively.

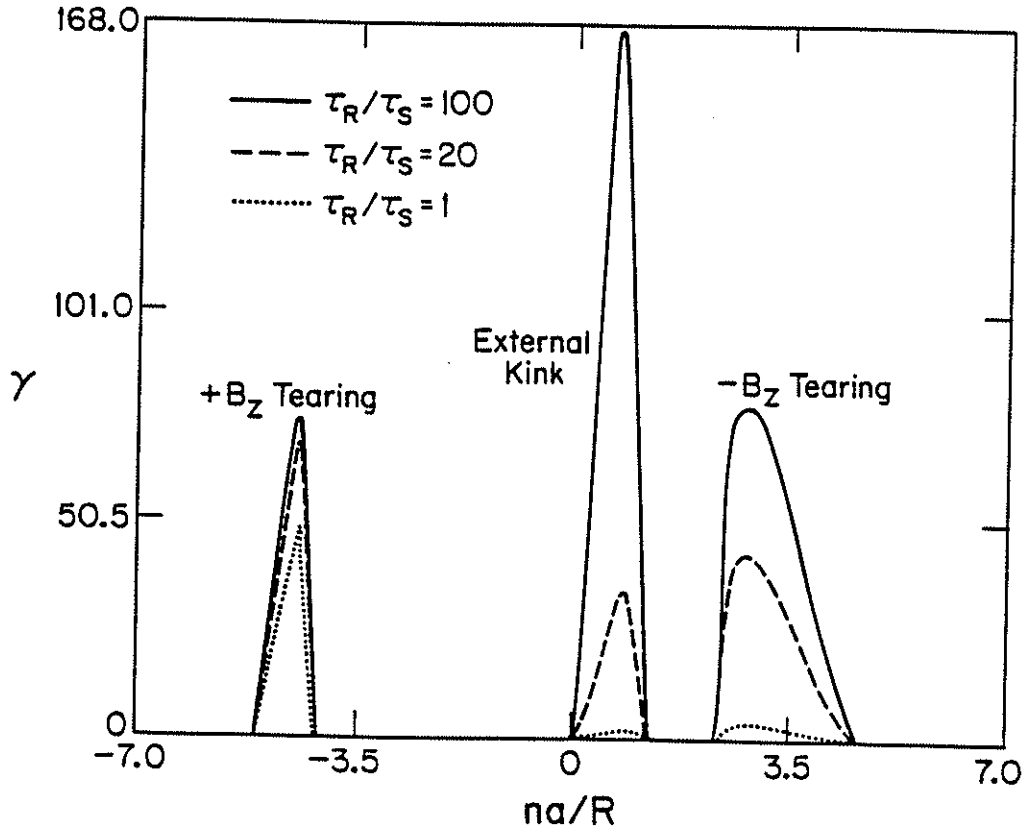

Fig. 2.4. Growth rate versus k/λ_o (= na/R) for different shell penetration times for m=1 modes. The growth rate is measured in units of resistive diffusion time τ_R. Parameters held constant are $\lambda_o a = 3.5$, $\Theta = 2.2$, $F = -1$, $S = 10^4$, and $r_w = 20$.

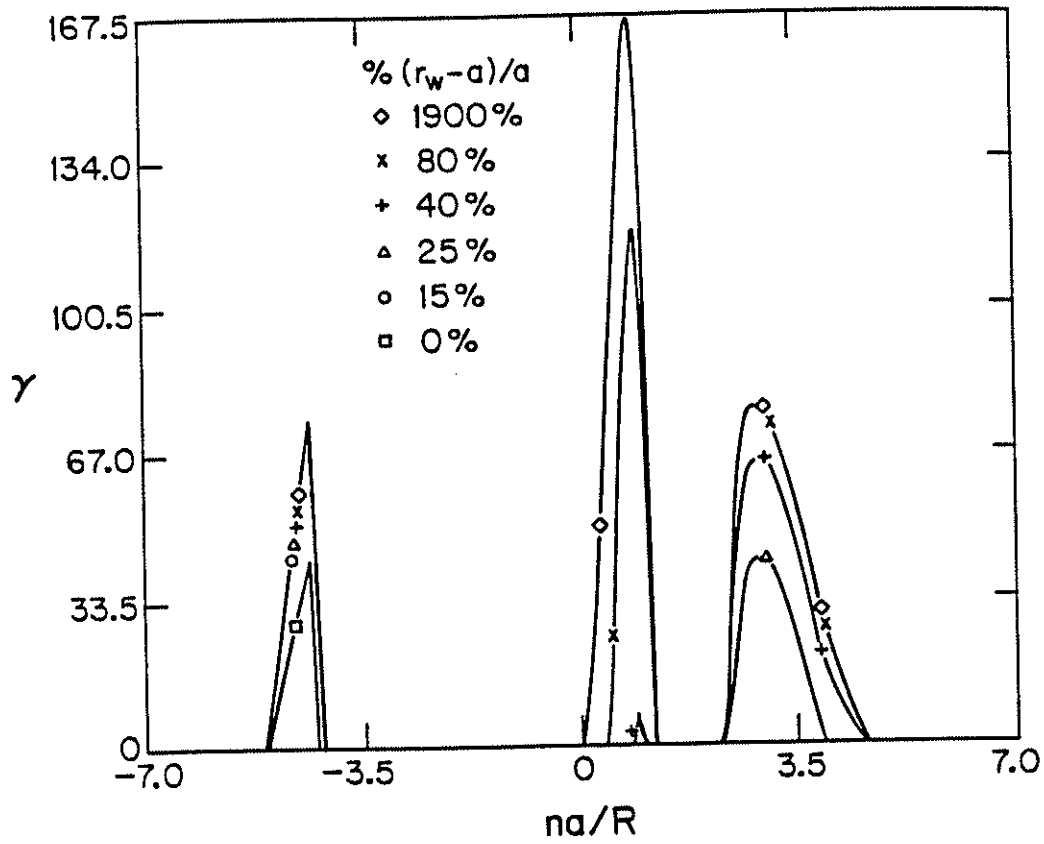

Fig. 2.5. Growth rate versus na/R for different vacuum region thicknesses for m = 1 modes. Parameters held constant are $\lambda_o a = 3.5$, $S=10^4$, and $\tau_R/\tau_S=100$.

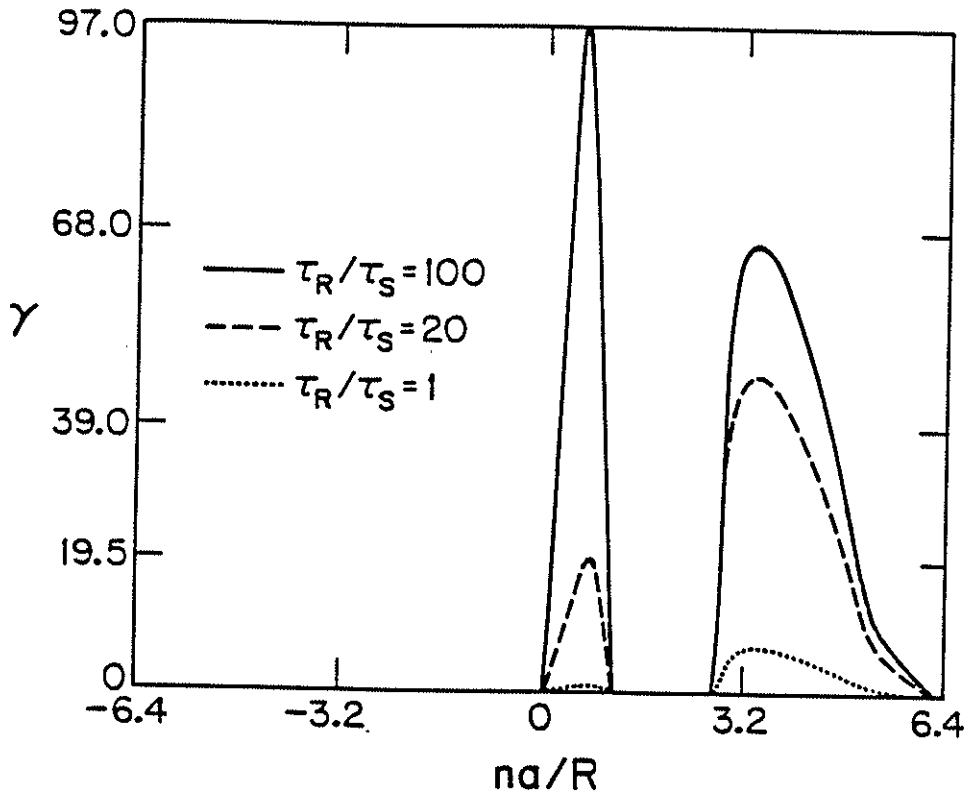

Fig. 2.6. Growth rate versus na/R for different wall penetration times for m = 1 modes. Parameters held constant are $\lambda_o a = 3.2$, $\Theta = 1.83$, $F = -0.69$, $S = 10^4$, and $r_w = 20$.

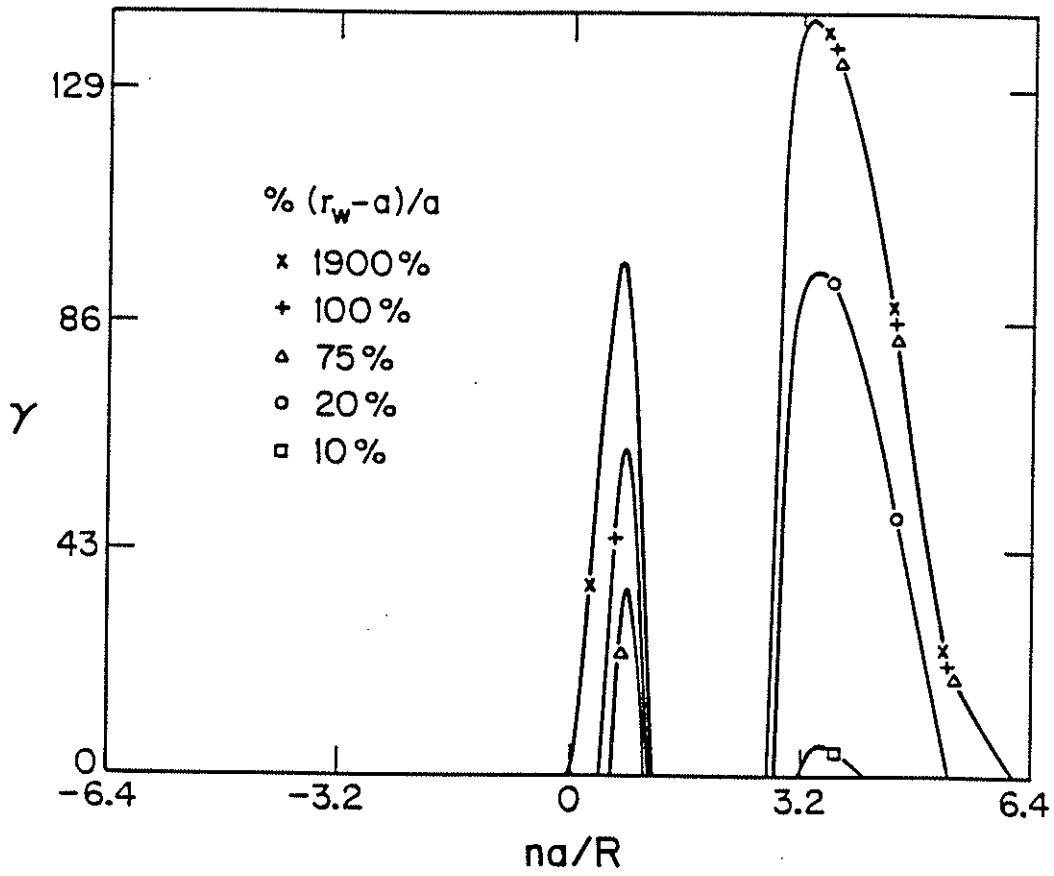

Fig. 2.7. Growth rate versus na/R for different vacuum region thickness for m = 1 modes. Parameters held constant are $\lambda_o a = 3.2$, $S = 10^4$, and $\tau_R/\tau_S = 100$.

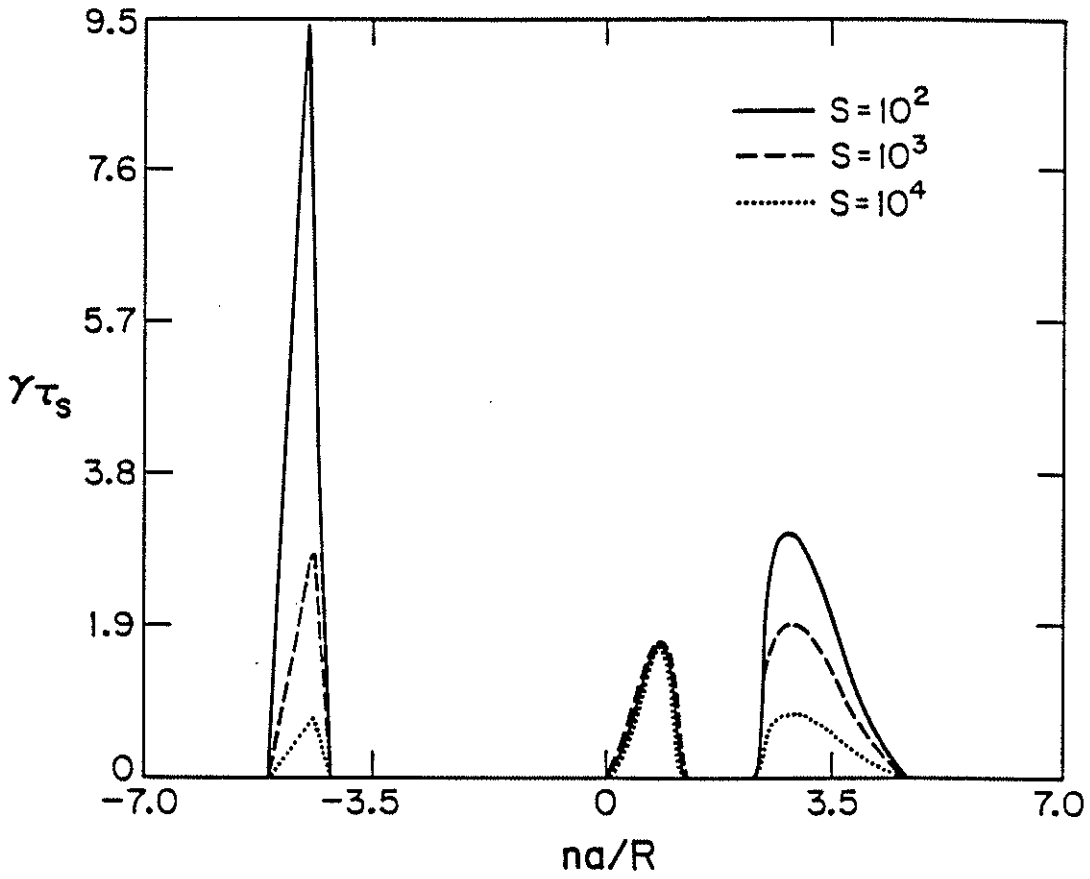

Fig. 2.8. Growth rate versus na/R for different Lundquist numbers S for m = 1 modes. The growth rate is espressed in units of wall penetration time τ_s, which is held at $100\tau_{A\theta}$. Parameters held constant are $\lambda_o a = 3.5$ and $r_w = 20$.

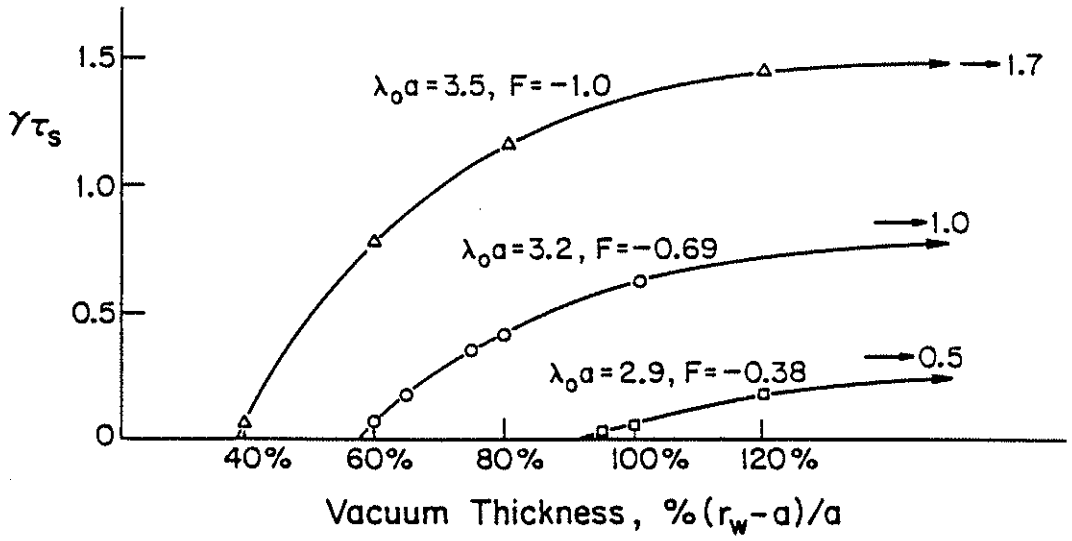

Fig. 2.9. Peak external kink growth rate versus vacuum region thickness for different $\lambda_0 a$. The growth rate is expressed in units of the wall penetration rate ($1/\tau_s$).

a. Region I ($+B_z$ tearing modes)

The experimentally relevant modes in this region are localized tearing modes resonant inside the reversal layer. Ideally unstable (resonant and nonresonant) modes occur at $\lambda_o a > 4$ and are out of the range of experimental interest. Hence, we do not separately identify the resonant ideal modes in Fig. 2.3a. The resonant surfaces of all the unstable modes are near r_b, i.e., close to the region of spatially decreasing λ. Physically, a λ which decreases with distance from a given resonant surface reduces magnetic shear near the resonant surface. This is a strong destabilizing factor in an RFP. As a group then, the modes that resonate near the axis are destabilized by a peaked λ profile. These modes and their nonlinear behavior may also play a dominant role in the RFP "dynamo"[19,20]. A more complete description of the various effects which determine stability, such as magnetic field compression and free energy sources, can be found in Ref. 21.

As a result of the spatial localization (radially) of the perturbed fluid velocity (a consequence of the relatively large toroidal mode number n) and the distance of the resonant surfaces to the boundary, these tearing modes are relatively independent of the boundary condition. This is evident from Fig. 2.3(a)–Fig. 2.3(c) where the region of instability below $\lambda_o a = 3.5$ remains essentially unchanged as the conducting wall is removed. A weak dependence on the boundary condition is further evident in the growth rate calculations shown in Figs. 2.4 and 2.5, where these modes occur at $na/R(=k/\lambda_o) \approx -4$. The parameter k/λ_o is expressed in

terms of an equivalent toroidal mode number n and major radius R, although the calculation does not assume toroidicity nor periodicity in the z direction. For Fig. 2.4, as τ_S changes from $1.0\tau_R$ to $.01\tau_R$ (at $r_w = 20$, $S = 10^4$ and $\lambda_o a = 3.5$), the growth rates increase only approximately 50%. In Fig. 2.5, τ_S was held at $.01\tau_R$ (or $100\tau_{A\theta}$), and the conducting wall moved from close fitting to essentially infinity (1900% vacuum). This caused a similar 50% change in growth rates.

Although the $\lambda_o a > 4$ region was not scrutinized, in a way this region may be more interesting; it contains both resonant and nonresonant modes with growth rates that order from S^0 (transport time scale) to S (ideal time scale), and resistive modes that may become ideal as $\tau_S \rightarrow 0$.

b. Region II (external kinks)

These modes are resonant in the vacuum outside of the plasma. They are unstable if the total toroidal flux inside the outer conducting wall is negative, consistent with previous stability analysis[22]. Therefore, without an outer conducting wall, the plasma would be kink unstable if B_z is reversed. Growth rate calculations are less pessimistic than calculations performed with skin-current pinch models[4,5]. From Figs. 2.4 – 2.8, the external kink appears at $0 < na/R < \sim 1$. For all the cases shown, γ is less than $1.7\tau_S^{-1}$.

These modes depend strongly on the wall proximity and penetration time τ_S of the resistive shell, as is evident from Figs. 2.4 – 2.7. Since they are not resonant in the plasma and therefore γ does not depend on S

(Fig. 2.8), growth rate calculations over wide ranges of boundary conditions can be usefully presented in terms of $1/\tau_s$. In Fig. 2.9, peak kink growth rates (growth rate for the kink mode with the most unstable mode number k) for each of the equilibrium configurations of $\lambda_o a = 2.9$, 3.2, and 3.5 are shown as a function of vacuum thickness. Instability is shown to appear for vacuum thickness greater than about 40% of the plasma minor radius if $F \approx -1$. For typical experimental F values, γ is only on the order of $0.5\tau_s^{-1}$ and the modes are unstable only for vacuum width greater than about 55% of plasma minor radius. In the limit of small τ_s, the unstable kink modes become ideal modes, growing on the Alfvénic time scale.

These modes are strongly global with a radial displacement nearly constant in radius. A simple test also showed that the kink growth rate depends dominantly on global parameters such as F and Θ rather than details of the current profile. Growth rate calculations with two-step λ profiles were similar to results with 20-step models.

c. Region III ($-B_z$ tearing modes)

The modes in this region within the range $2.9 < \lambda_o a < 3.5$ are localized tearing modes resonant outside the reversal surface (with their velocity eigenfunctions localized within this outer region). Despite their localized nature, the modes show strong dependence on the conducting wall for stability due to the proximity of the resonant surface to plasma boundary. Figure 2.3(a) shows that these modes are completely stable with a close-fitting conducting wall. In Figs. 2.4 – 2.8, they show up as the

rightmost modes in the growth rate plots, and occur near $na/R \approx 3.5$. Figure 2.8 shows a comparison of growth rates for three different S values with the same boundary condition. The results can also serve as an indicator of the depencence on boundary conditions. The growth rate γ enters both the tearing mode jump condition [Eq. (2.2)] and the shell jump condition [Eq. (2.3)]. The growth rate of modes independent of the boundary will contain the $S^{2/5}$ scaling resulting from the jump condition in Eq. (2.2), whereas the growth rate of modes strongly dependent upon the boundary will be S independent, due to dominance of Eq. (2.3). Kink modes in this figure are completely independent of S as indicated previously, and the $+B_z$ tearing modes show a nearly $S^{2/5}$ scaling, which indicates a weak τ_s dependence. The $-B_z$ tearing modes, however, show an S dependence somewhere in between the other two cases. This is also illustrated in Fig. 2.10 where the peak edge tearing mode growth rate for each equilibrium configuration is plotted against S. Results show scalings between $S^{2/5}$ (dashed line) and S^0 (pure τ_s dependence).

Figures 2.5 and 2.7 show the dependence of the growth rate on the vacuum region width. With weaker reversal, the $-B_z$ tearing modes have higher k values. Since the vacuum fields decay more rapidly with radius for shorter wavelength modes, such modes approach their maximum growth rate with thinner vacuum region. Thus, the peak growth rates occur at $(r_w-a)/a \sim 20\%$ for $\lambda_o a = 3.2$ cases, and at $\sim 40\%$ for $\lambda_o a = 3.5$ cases.

In Fig. 2.7, tearing instability growth rates are shown to exceed those for kink modes (for $S = 10^4$, $\lambda_o a = 3.2$, $\tau_s = 100\tau_{A\theta}$ and over 20% vacuum

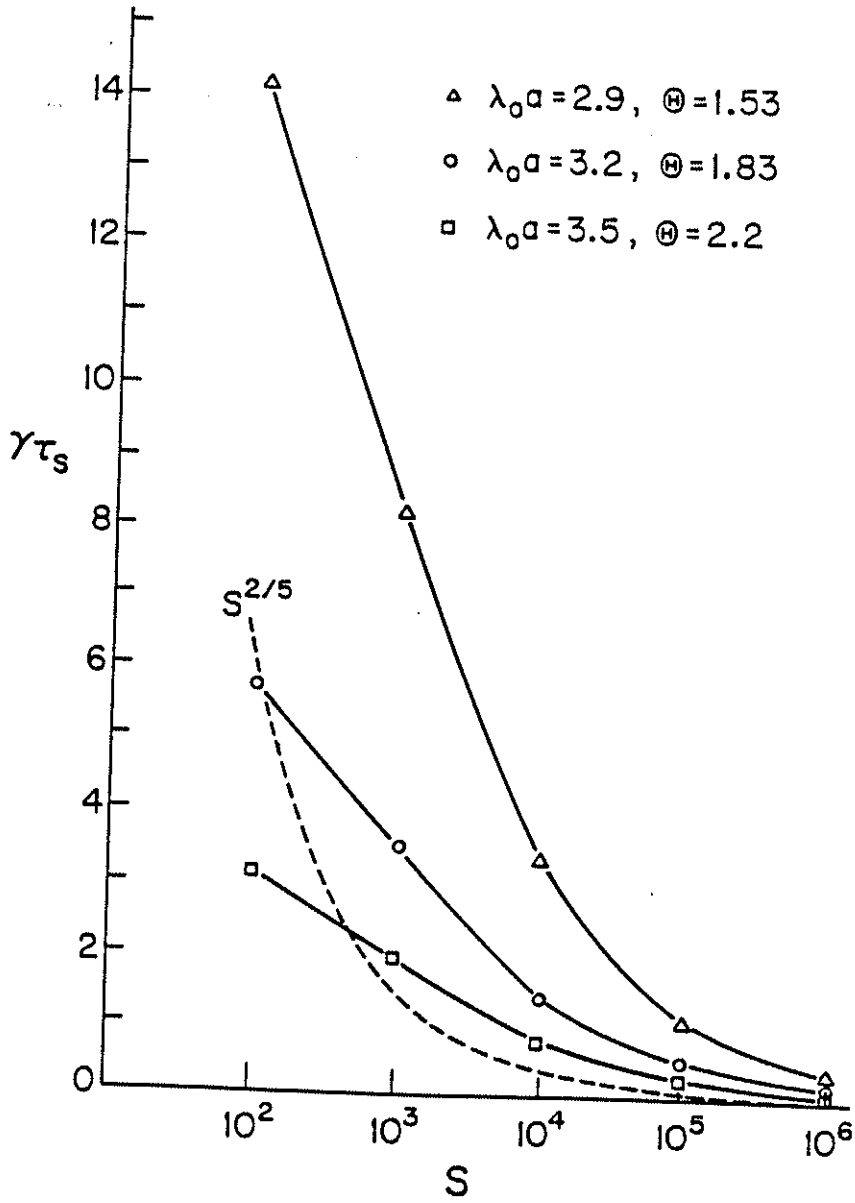

Fig. 2.10. Growth rate versus S for different $\lambda_0 a$ for m = 1, $-B_z$ tearing modes. The growth rate is expressed in units wall penetration time τ_s (= $100\tau_{A\theta}$ for these cases) and is for the peak $-B_z$ instability in each case. The dashed line shows a hypothetical case if the growth rate is equal to $S^{2/5}$ for comparison. For these cases, the conducting wall is far away ($r_w = 20$).

region). These modes are even more unstable for lower values of $\lambda_o a$ as shown in Fig. 2.10. The increased growth rates at lower values of on-axis λ, are caused by the increasing λ profile edge gradient, as the equilibrium becomes more BFM-like. Without an outer conducting wall and for $\tau_S = 100\tau_{A\theta}$, the $\lambda_o a = 2.9$ cases resemble resistive kinks more than tearing modes, i.e., the plasma displacement is mainly outside the resonant surface and an $\eta^{1/3}$ scaling may be more appropriate. However, none of the three $\lambda_o a$ cases discussed above ever become ideally unstable for any τ_S, so plasma resistivity at the resonant surface can never be ignored. Interestingly, the proper ordering of γ for the $-B_z$ mode, when $\lambda_o a = 2.9$, can vary continuously from $S^{-\infty}$ to $S^{2/3}$, depending on the boundary conditions.

d. Region IV

Instabilities in this region occur in nonreversed and weakly reversed field plasmas. The occurence of the nonreversed resonant modes can be attributed to a pitch-minimum (as discussed in Ref. 22), which is a manifestation of a flat λ profile at low $\lambda_o a$ and a edge vacuum region. More generally, instabilities occur due to the weak shear and a distant conducting wall. Aside from the unrealistic modes caused by the BFM-like profile (discussed in Sec. 2.2.c) the most dangerous modes in this region are those nearly resonant on axis[22] [i.e., $-1/n \sim q(r = 0)$]. These kink modes are typically associated with Tokamak $q = 1$ limits; if a periodic boundary condition was imposed in the z direction and $q(r = 0) > 1$, then in

the low $\lambda_0 a$ Tokamak limit, no unstable mode would satisfy the periodicity constraint. This is a well known result applicable to a wide range of current profiles. Similar to the $\lambda_0 a > 4$ region discussed in Sec. 2.3.a, instabilities in this region contain resonant ideal modes, resistive kinks, kink modes, tearing modes, etc.. However, these modes depend strongly on the boundary condition; the modes can change character (e.g., resistive kink→tearing mode, stable→unstable) as the boundary condition varies. Linear growth rate calculations will not be included here since the instabilities only occur with reversal weaker than what is seen in experiments. However, these modes can be nonlinearly important if the plasma cannot sustain a deep enough reversal due to one of the other modes discussed earlier.

2.4. RESULTS FOR m = 0

Stability boundaries for both close-fitting and far-removed conducting wall cases are indicated in Fig. 2.11, from which we see that unstable modes occur only with B_z reversed (i.e., resonant instabilities.). Thus, the modes of greatest interest, and those treated here, are tearing instabilities. In the range of experimental interest, low k modes are unstable even with no vacuum region. Aside from this fact, the unstable modes exhibit a similar sensitivity to the boundary conditions as in the $-B_z$ tearing modes discussed in the m = 1 section. The moderate dependence of these modes on the boundary is illustrated in Figs. 2.12–2.14 which display a family of growth rate curves for varying vacuum region thickness. Each figure is

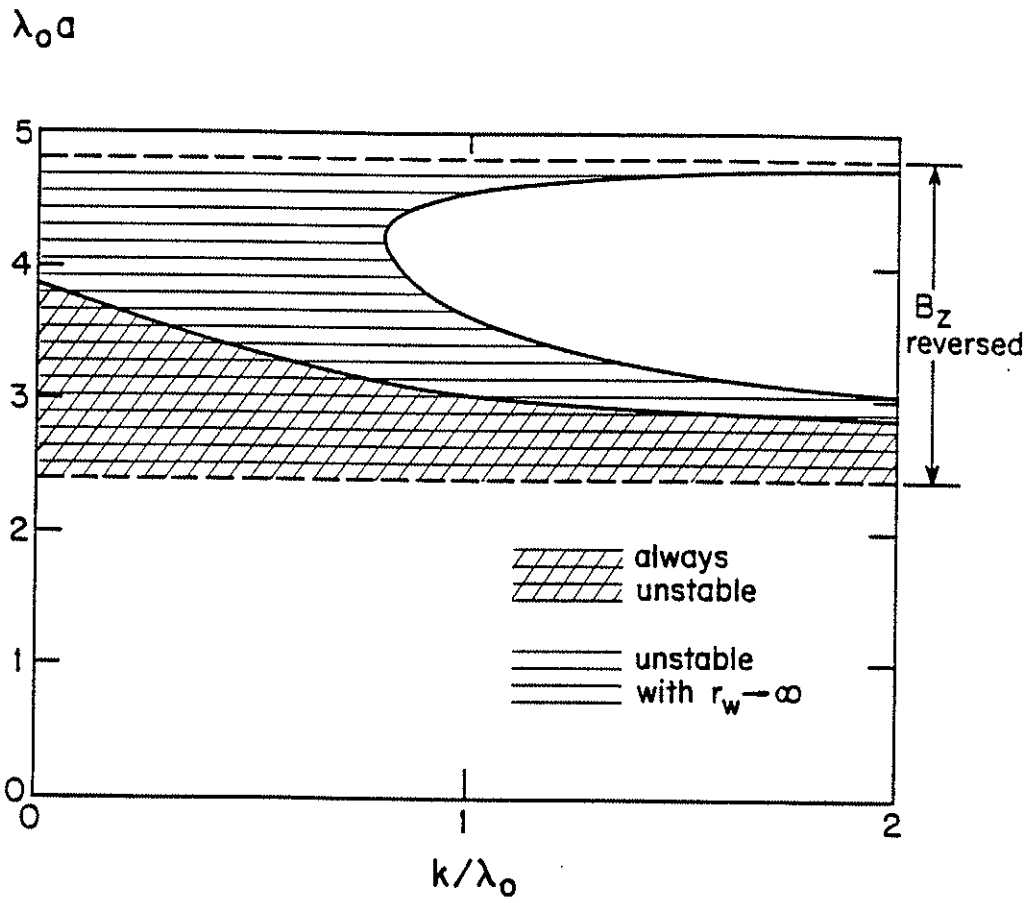

Fig. 2.11. The m = 0 stability diagram in the parameter space $\lambda_o a$ versus k/λ_o. Regions of instability are shown shaded for both close-fitting conducting wall and no conducting wall cases.

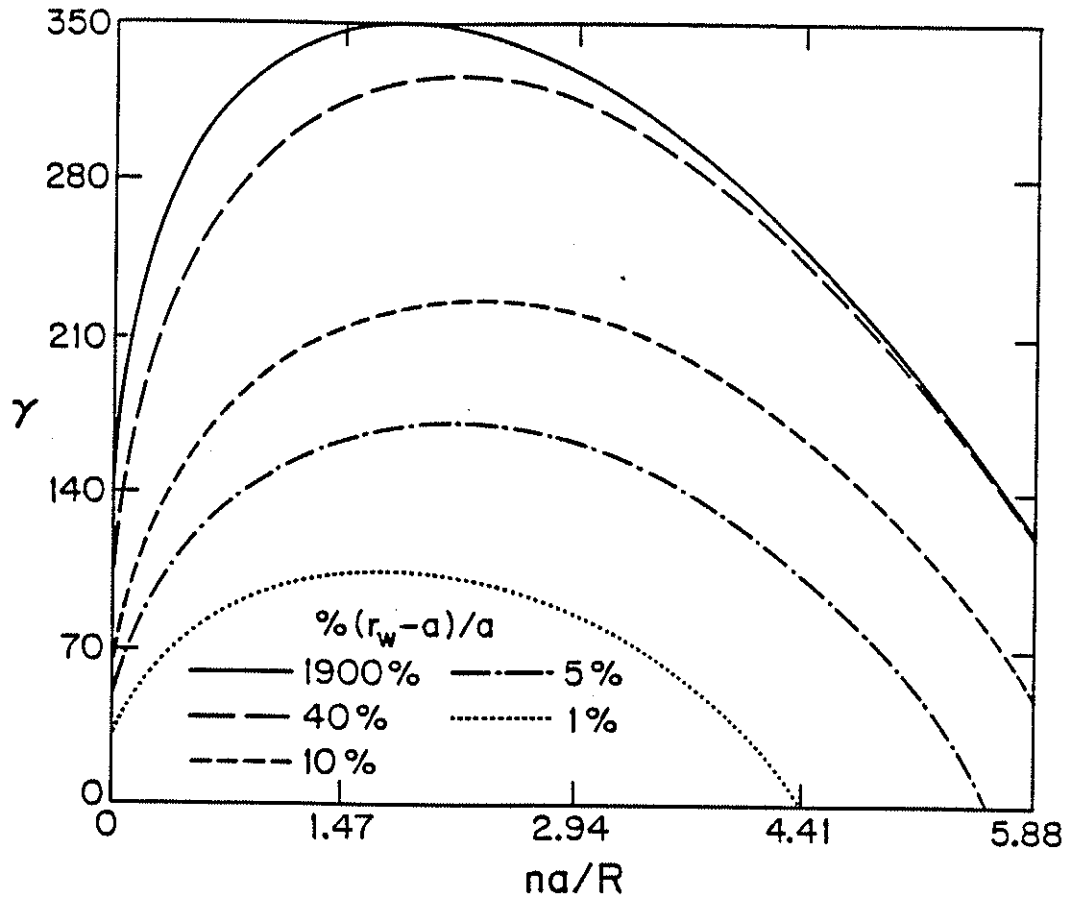

Fig. 2.12. Growth rate versus na/R for different vacuum region thicknesses for m = 0 modes. Parameters held constant are $\lambda_o a = 2.94$, $\Theta = 1.57$, $F = -0.42$, $\tau_R/\tau_S = 100$, and $S = 10^4$.

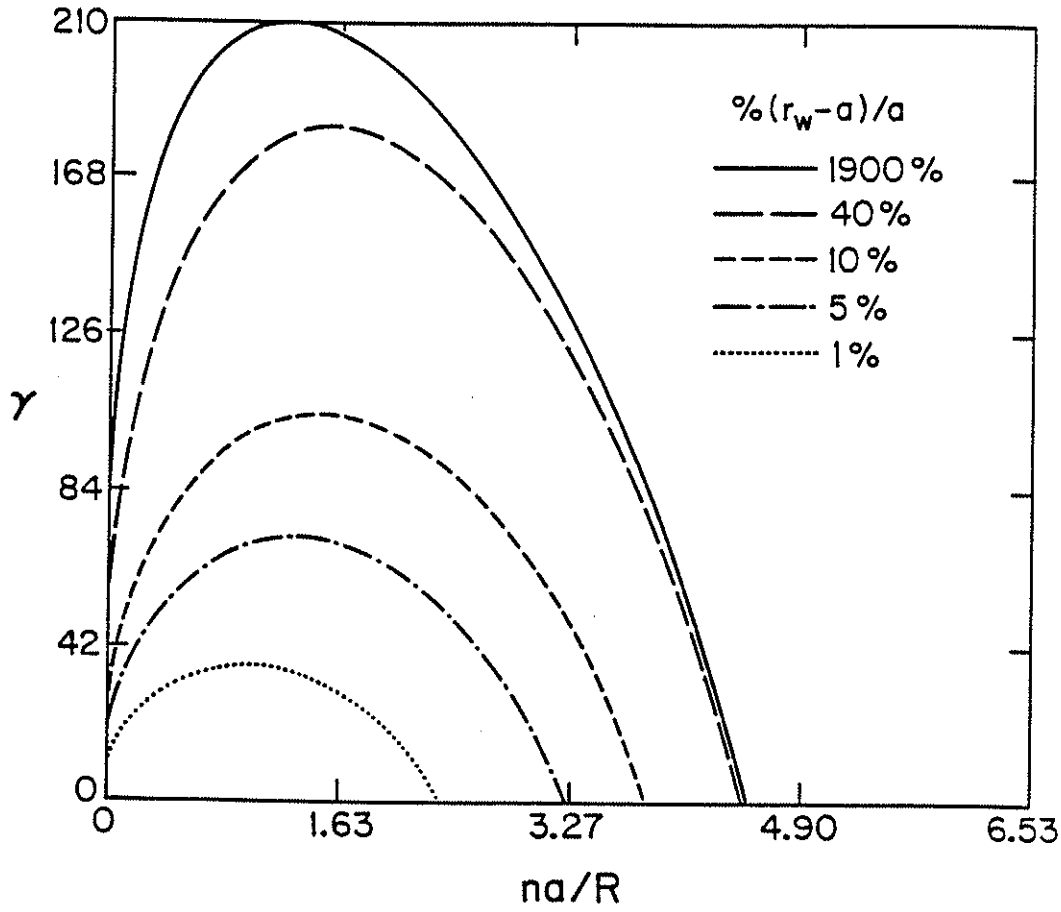

Fig. 2.13. Growth rate versus na/R for different vacuum region thicknesses for m = 0 modes. Parameters held constant are $\lambda_o a = 3.27$, $\Theta = 1.91$, $F = -0.76$, $\tau_R/\tau_S = 100$, and $S = 10^4$.

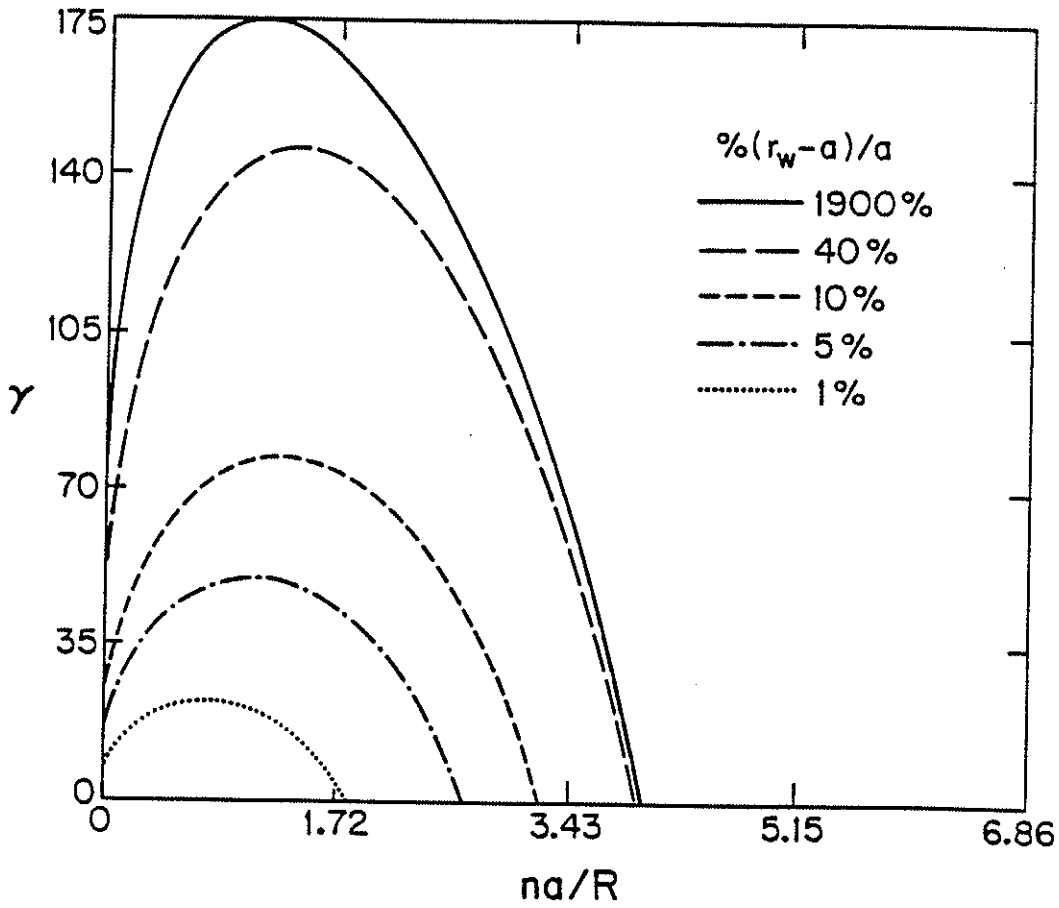

Fig. 2.14. Growth rate versus na/R for different vacuum region thicknesses for m = 0 modes. Parameters held constant are $\lambda_o a = 3.43$, $\Theta = 2.12$, $F = -0.95$, $\tau_R/\tau_S = 100$, and $S = 10^4$.

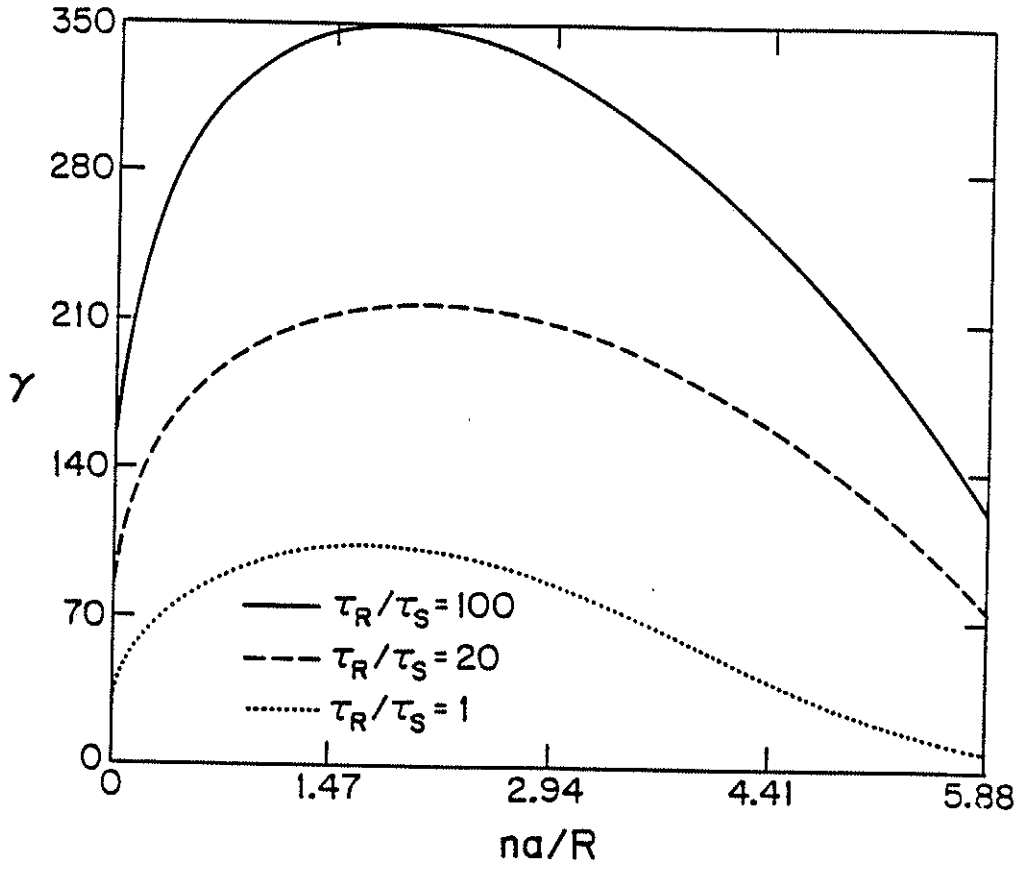

Fig. 2.15. Growth rate versus na/R for different wall penetration times for m = 0 modes. Parameters held constant are $\lambda_o a = 2.94$, $r_w = 20$, and $S = 10^4$.

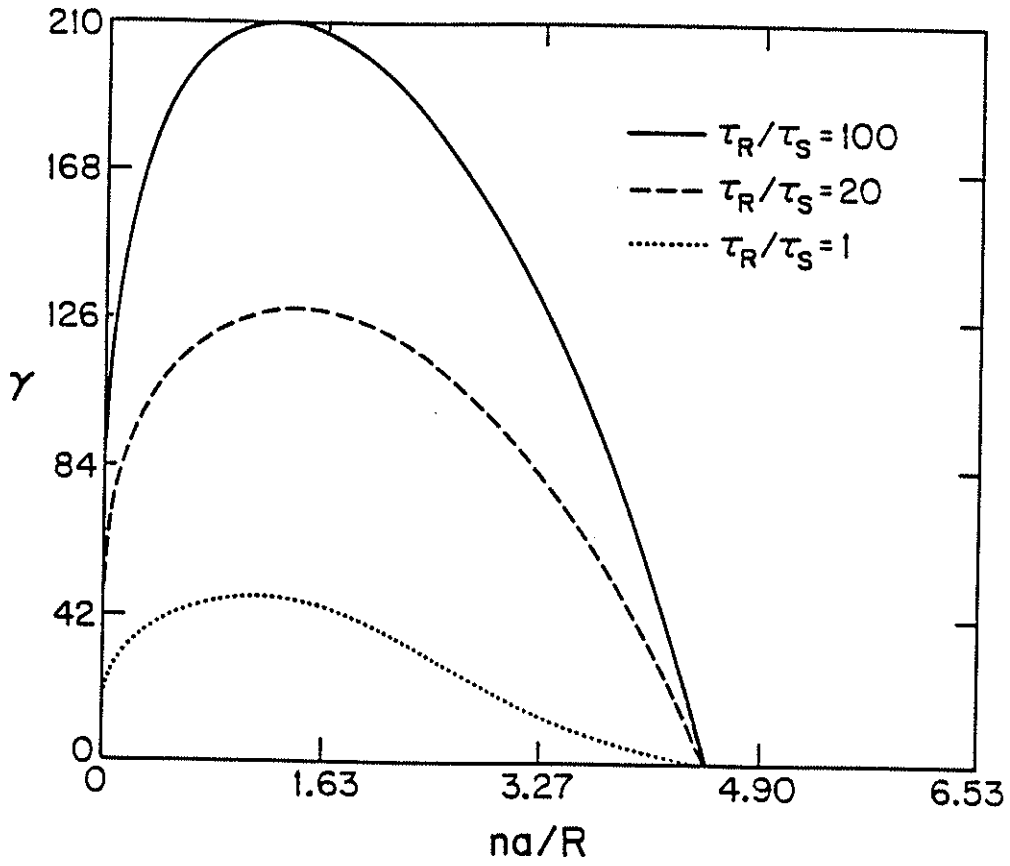

Fig. 2.16. Growth rate versus na/R for different wall penetration times for m = 0 modes. Parameters held constant are $\lambda_o a = 3.27$, $r_w = 20$, and $S = 10^4$.

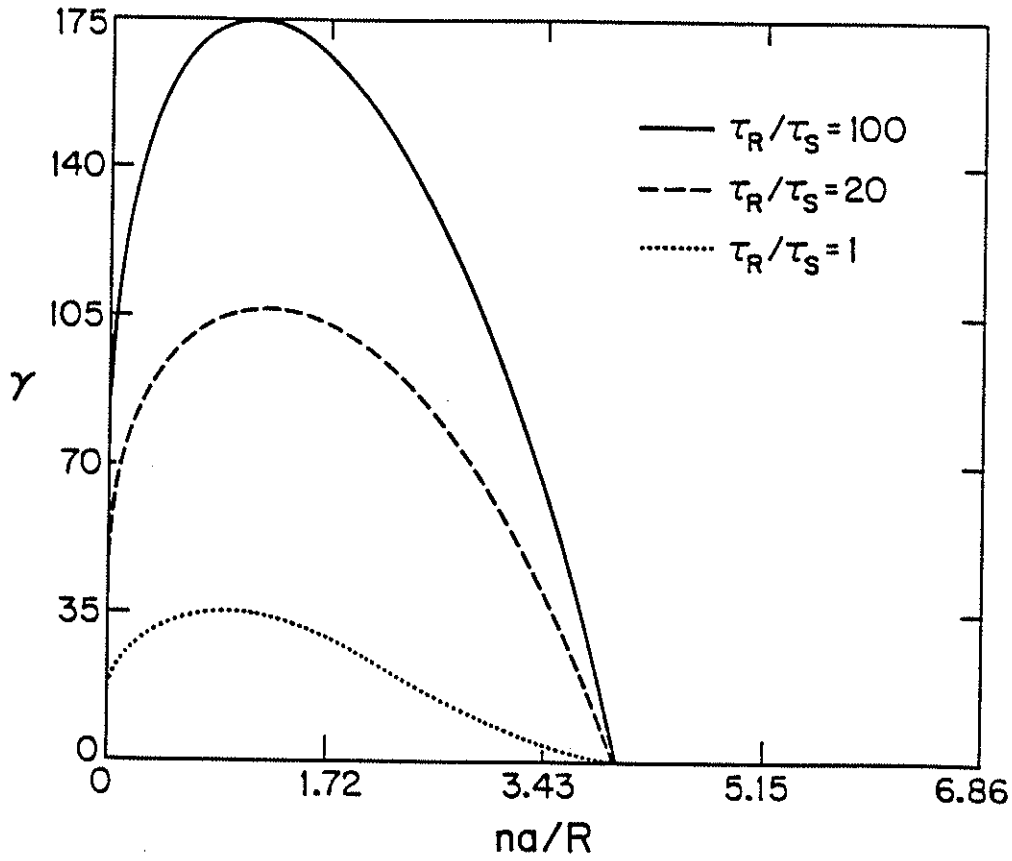

Fig. 2.17. Growth rate versus na/R for different wall penetration times for m = 0 modes. Parameters held constant are $\lambda_o a = 3.43$, $r_w = 20$, and $S = 10^4$.

for a different $\lambda_o a$ value. The growth rate variations with τ_S are similarly displayed in Figs. 2.15–2.17. Beyond $\tau_R/\tau_S = 100$ (the maximum value shown), the growth rate does not change noticeably.

At the most unstable k values, these modes can become resistive kinks ($\eta^{1/3}$ scaling) for large vacuum regions and small τ_S. For $\tau_S \sim 100\tau_{A\theta}$, the transition occurs at ~ 10% vacuum region width for the $\lambda_o a = 2.94$ case and ~ 40% for the other two $\lambda_o a$ cases. Without an outer conducting wall, the transition points are at $\tau_R/\tau_S \sim 20$ for $\lambda_o a = 2.94$ and $\tau_R/\tau_S \sim 100$ for the $\lambda_o a = 3.43$ and $\lambda_o a = 3.27$ cases. The somewhat arbitrary transition points are estimated from examination of the radial structure of the eigenfunctions and the magnitudes of the growth rates. The modes, however, never become resonant ideally unstable for any τ_S, which is similar to what was found for the m = 1, $-B_z$ tearing modes. Away from the most unstable k values, other modes remain only tearing unstable. For most of the parameter space investigated, the $S^{2/5}$ ordering is adequate.

In general, m = 0 modes show less dependence on boundary condition than the $-B_z$ tearing modes. This is clealy seen in Fig. 2.18 where growth rates scales closer to $S^{2/5}$ than results in Fig. 2.10. This indicates a weaker τ_S dependence in the absence of the outer conducting wall.

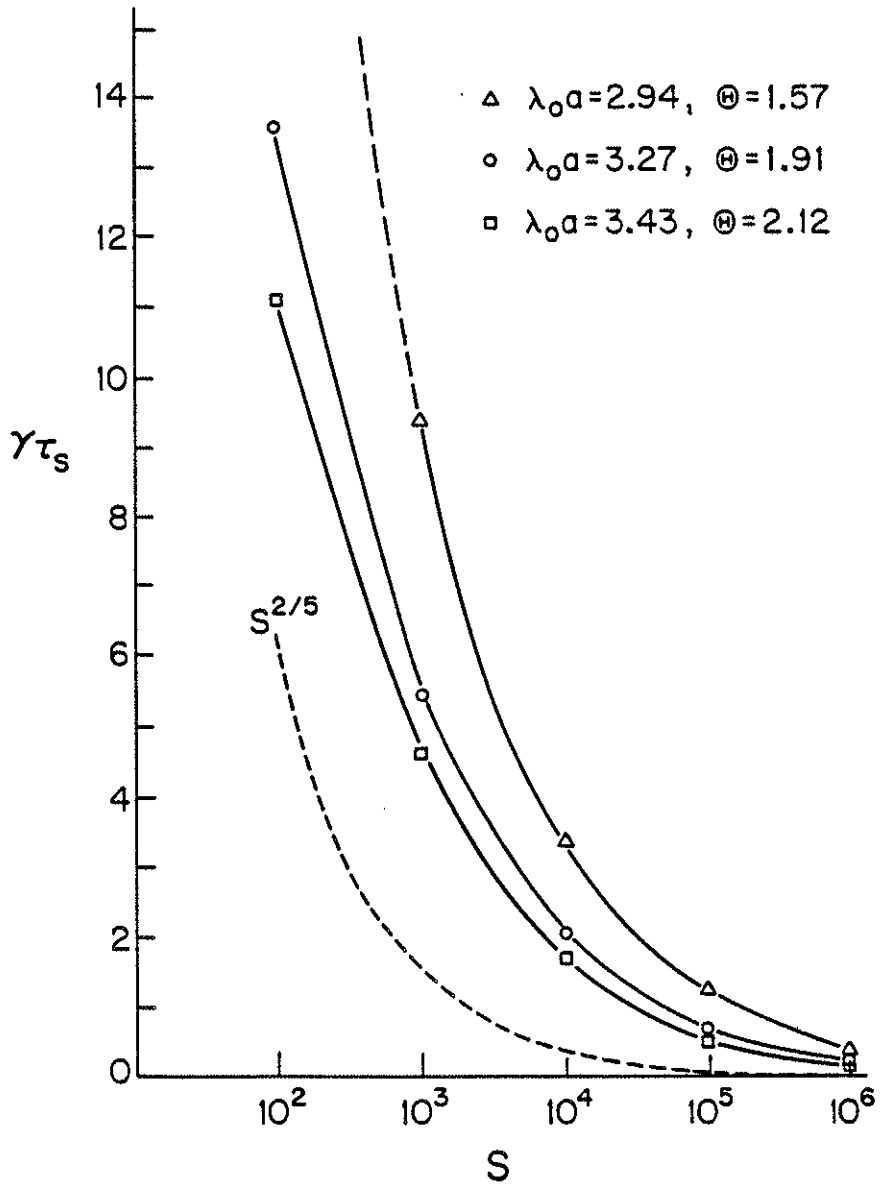

Fig. 2.18. Growth rate versus S for different $\lambda_o a$ for m = 0 modes. The growth rate is expressed in units wall penetration time τ_s (= $100\tau_{A\theta}$ for all cases here). For these cases, the conducting wall is far away ($r_w = 20$).

2.5. SUMMARY AND DISCUSSION

a. Summary

We have evaluated linear MHD stability to current driven modes for RFP plasmas for an equilibrium which fits available experimental data (the MBFM model) and for a variety of realistic boundary conditions. However, to further aid interpretation of the code results in the following chapter, we note pertinent features of linear stability based not only on the MFBM, but also on more general equilibrium profiles. The more general profiles are obtained by using relationships between r_b and $\lambda_o a$ different from the MFBM prescription.

Modes with poloidal mode number, m, greater than one are stable. Modes with large axial wave number magnitude, $|k|$, are radially localized. Hence, they are less influenced by the conducting wall, unless they are resonant near the boundary. For $m = 1$, $n < 0$ modes then, reliance on the conducting wall for stability is generally weaker for the $\Theta > 1.4$ modes in comparsion to the lower Θ cases. This is due to the greater distances of the resonant surfaces from the boundary for the lower values of q, and the corresponding shift of the spectrum toward higher $|k|$. For the modes within the $\Theta > 1.4$ range, dependence of the spectrum on q is not so easily generalized, since details of the current profile (hence q profile) become important for these relatively localized modes. In the range $\Theta \sim 1.4$ to 1.95 (which roughly corresponds to the experimental operating range), at all conducting wall positions, both stable and unstable (to the $m = 1$, $k < 0$ modes) equilibria can be found. The stable equilibria

tend to have as flat or flatter λ profiles than the MBFM; incontrast, the unstable equlibria tend to be more peaked in λ. For a plasma marginally stable to the $m = 1$, $n < 0$ modes this indicates that taking away the conducting wall can be compensated by an increase in equilibrium magnetic shear, i.e., the plasma can remain marginally stable in this crucial Θ range. For Θ below 1.4, stable profiles, not considering hollow λ profiles, exist only with a conducting wall nearby (unless $q(r) > 1$, which is the Tokamak region). The $m = 1$, $k > 0$ external kink modes (which are global and nonresonant) strongly depend on the boundary. These modes are unstable if the perfectly conducting wall encloses negative toroidal flux. Without a wall, these modes are unstable if B_Z is reversed. The growth rate increases with the depth of reversal and with $1/\tau_S$. Thus, profiles that are stable to the $m = 1$, $n < 0$ modes at $\Theta > 1.4$ may be unstable to the $n > 0$ external kinks. For the equilibria studied, $m = 0$ modes (driven by λ-gradients at the edge) are unstable in reversed plasmas with growth rates moderately sensitive to the boundary conditions. Similarly, $m = 1$, $k > 1$ tearing modes resonant in the reversed B_z region are also driven by λ-gradients at the edge, and are moderately sensitive to the boundary. These modes, however, are only unstable without a close-fitting conducting wall.

b. Discussion

As noted earlier, the MFBM may introduce inaccuracies for localized modes which depend upon details of the λ profile (particularly at the edge

for low Θ cases). Modes localized to the edge region may be additionally influenced by the high edge resistivity present in experiments, but ignored in the calculation (away from the resonant surface). In this sense, we rank the reliability of the results for different modes, in order of decreasing applicability to experiment as: $+B_z$ tearing modes and external kinks, $m = 0$ tearing modes, $-B_z$ tearing modes. Moreover, we can expect plasma rotation (assuming sub-Alfvénic flow) relative to the resistive shell to have a larger stabilizing effect on the $m = 0$ and $-B_z$ tearing modes than on the kink and the $+B_z$ tearing modes. This is obvious for the $+B_z$ tearing modes due to the weaker boundary condition dependence of its growth rate. For the external kink, it was shown in Ref. 1 that the modes lock to the wall, requiring near-Alfvénic velocity for significant reduction in its growth rate. The $m = 0$ and $-B_z$ tearing modes however, can be stabilized since a mode cannot lock to both the wall and the resonant resistive layer.

With the above caveats in mind, we apply our results to specific experimental examples, namely the OHTE and MST devices. For OHTE, assuming $S = 10^4$, $\tau_R = 3$ msec, $\Theta \sim 1.72$, $F \sim -0.58$ ($\lambda_o a = 3.1$), we consider four different shell conditions: $\tau_s = \infty$ (perfectly conducting wall), $\tau_s = 60$ms (original aluminum shell), $\tau_s = 3$ ms (thin brass shell[23]), $\tau_s = 0.25$ms (stainless-steel of same thickness as the brass case). For each case, we list in TABLE 2.1 the shortest calculated growth time for the different modes. We see that the $m = 0$ mode is unstable in all cases. The external kink and $-B_z$ tearing mode onset with the brass shell. However, the external kink mode might not grow to visibility within the plasma lifetime (~ 10–15ms).

Furthermore, if the reversal is somehow shallower ($|F|$ smaller), growth may be yet slower. This might explain why the external kinks are not seen in the OHTE experiments[24].

In the upcoming MST experiment, the "vacuum" region between the plasma and wall (5 cm thick aluminum) will be varied by the use of movable toroidal limiters. Growth-time predictions for various vacuum thickness are shown in TABLE 2.2. As the vacuum region is increased, the growth rate of the $m = 0$ tearing mode increases slowly and the $m = 1$, $-B_z$ tearing modes become unstable at about 10% vacuum. Both modes have growth-times in the range $0.1\tau_R$ to $0.01\tau_R$, which is probably sub-millisecond. When the vacuum region thickness reaches about 60%, the $m = 1$ external kinks become unstable, and grow on the Alfvén time-scale.

For all modes, increasing r_w beyond 2a has a negligible effect on the growth rate; therefore, toroidicity should have minimal effects on these results as long as $R/a > 2$.

Finally, we note that the stability analysis used here is more tolerant of errors than shooting methods (not including the matrix shooting technique[25]). We solve for the growth rates for a variety of boundary conditions, profiles, and mode numbers, then indicate the marginal stability (zero growth rate) lines with a contour plot. In contrast, shooting methods tend to solve for the conducting wall locations at which a configuration is marginally stable to a given mode. The difficulty arises near the singular surface where errors are easily introduced due to the λ'/f

TABLE 2.1. Growth times for OHTE-sized plasmas.

Wall material	m=1 $+B_z$ tearing	m=1 external kink	m=1 $-B_z$ tearing	m=0 tearing
		n=0-6	n=18-36	n=0-27
ideal ($\tau_S = \infty$)	marginally stable	stable	stable	~0.05 msec
Al (τ_S = 60 msec)	marginally stable	~76 msec	~6.4 msec	~0.05 msec
Brass (τ_S = 3 msec)	marginally stable	~3.8 msec	~0.34 msec	~0.05 msec
Stainless-steel (τ_S = 0.25 msec)	marginally stable	~0.32 msec	~0.04 msec	~0.02 msec

TABLE 2.2. Growth times for MST.

vacuum thickness	m=1 $+B_z$ tearing	m=1 external kink	m=1 $-B_z$ tearing	m=0 tearing
1%	marginally stable	stable	stable	~τ_R/60
5%	marginally stable	stable	stable	~τ_R/110
10%	marginally stable	stable	~τ_R/64	~τ_R/150
40%	marginally stable	stable	~τ_R/220	~τ_R/300
>60%	marginally stable	Unstable-Alfvénic	~τ_R/220	~τ_R/300

term in Eq. (2.1). Since many modes are weakly dependent on the boundary condition, small errors incurred while shooting across the singular surface results in a large discrepency in the conducting wall location. In our analysis, small errors in the field solution near the resonant surface results in a small error in the calculated growth rate. This does not change the contour of marginal modes significantly, since small errors in γ cannot change the stability of neighboring nonmarginal modes.

REFERENCES

[1]C. G. Gimblett, Nucl. Fusion **26**, 617 (1986).

[2]D. Pfirsch and H. Tasso, Nucl. Fusion **11**, 259 (1971).

[3]A. S. Furzer and D. C. Robinson, in *Proceedings of the 7th European Conference on Controlled Fusion and Plasma Physics*, Lausanne, 1975, (Centre de Recherches en Physique des Plasmas, Ecole Polytechnique Fédérale de Lausanne, Switzerland, 1975) Vol.I, p.114.

[4]J. P. Goedbloed, D. Pfirsch, and H. Tasso, Nucl. Fusion **12**, 649 (1972).

[5]G. F. Nalesso and S. Costa, Nucl. Fusion **20**, 443 (1980).

[6]G. F. Nalesso, Phys. Fluids **28**, 2502 (1985).

[7]T. C. Hender, C. G. Gimblett, and D. C. Robinson, in *Proceedings of the 13th European Conference on Controlled Fusion and Plasma physics*, Schliersee, Germany, 1986, (European Physical Society, Budapest, 1986), Vol.I, p.61.

[8]K. F. Schoenberg, R. F. Gribble, J. A. Phillips, Nuclear Fusion **22**, 1433 (1982).

[9]See, for example, H. A. B. Bodin, in *Proceedings of the International conference on Plasma Physics*, Lausanne, 1984 (EEC, Brussels, 1984), Vol.I, p.417.

[10]E. J. Caramana and D. D. Schnack, Phys. Fluids **29**, 3023 (1986).

[11]B. Coppi, J. M. Greene, and J. L. Johnson, Nucl. Fusion **6**, 101 (1966).

[12]H. P. Furth, J. Killeen, and M. N. Rosenbluth, Phys. Fluids **6**, 459 (1963).

[13]A. H. Glasser, H. P. Furth, and P. H. Rutherford, Phys. Rev. Lett. **38**, 234 (1977).

[14]J. P. Goedbloed, Physica **53**, 501 (1970).

[15]D. C. Robinson, Nuclear Fusion **18**, 939 (1978).

[16]S. Chandrasekhar and P. C. Kendall, Astrophys. J. **126**, 457 (1957).

[17]W. L. Newcomb, Ann. Phys. **10**, 232 (1960).

[18]See, for example, I. H. Hutchinson, M. Malacarne, P. Noonan, D. Brotherton-Ratcliffe, Nucl. Fusion **24**, 59 (1984).

[19]See, for example, A. Y. Aydemir, D. C. Barnes, E. J. Caramana, A. A. Mirin, R. A. Nebel, D. D. Schnack, and A. G. Sgro, Phys. Fluids **28**, 898 (1985).

[20]A. Y. Aydemir and D. C. Barnes, Phys. Rev. Lett. **52**, 930 (1984).

[21]J. P. Freidberg, Rev. Mod. Phys. **54**, 801 (1982).

[22]D. C. Robinson, Plasma Physics **13**, 439 (1971).

[23]R. R. Goforth, T. N. Carlestrom, C. Chu, B. Curwen, D. Graumann, P. S. C. Lee, E. J. Nilles, T. Ohkawa, M. J. Schaffer, T. Tamano, P. L. Taylor, and T. S. Taylor, Nuclear Fusion **26**, 515 (1986).

[24]R. J. La Haye, P. S. Lee, M. J. Schaffer, T. Tamano, P. L. Taylor, Nuclear Fusion **28**, 918 (1988).

[25]J. P. Freidberg and D. W. Hewett, J. Plasma Physics **26**, 177 (1981).

Chapter 3
NONLINEAR BEHAVIOR

3.1. INTRODUCTION

In this chapter we present computational results on the effect of a nonideal boundary on nonlinear resistive MHD evolution. Although the $+B_z$ instabilities (possible dynamo modes) are, in linear theory, minimally affected by boundary condition variations, nonlinear behavior couples all the modes and allows the modes to modify the equilibrium and hence affect the loop voltage. Thus, it is difficult to predict a priori the effect of the boundary variation on the "dynamo" from the earlier linear results. Also, all equilibria with resistive boundary conditions are linearly unstable to long wavelength kink modes. Such modes should be more difficult to nonlinearly saturate than localized tearing modes. The increasing instability of tearing modes resonant near the surface when the λ profile becomes more BFM-like also complicates the standard Taylor relaxation model. This should not be surprising since the helicity utilized in the Taylor model is undefined with a resistive boundary [1]. To understand the roles played by nonlinear mode coupling, quasilinear modification of the equilibrium, and the applied V_L coupled with resistive diffusion of the equilibrium, it is necessary to investigate the nonlinear behavior of the RFP with the nonideal boundary conditions. Since current computational capabilities do not yet permit us to use realistic parameters in our simulation (S, R/a,...etc.), our goal is to include

enough physics in our model to identify the key physical mechanisms that influence the plasma as the boundary is varied.

The techniques of numerical MHD modeling are well established and no further elaboration is needed (for examples, see Refs. 2, 3, and 4). As for the RFP, several three dimensional codes already exist that solve the force-free MHD equations[5] with a perfectly conducting boundary. For our investigation, we chose to modify one of the existing 3D codes[6] to include the new boundary conditions and necessary diagnostics. The code was also suitably tailored to the architecture of the Cray-II computers at the National Magnetic Fusion Energy Computing Center to permit faster execution of the large amount of computations necessary.

Section 3.2 briefly describes the code, the imposed boundary conditions, and some benchmark results. The reasons behind the choices of the key simulation parameters are also summarized. Results of the multiple helicity simulations are presented in Sec. 3.3. We first depict pertinent features of a sustained RFP plasma with a close-fitting perfectly conducting wall. These features, including the "dynamo", are monitored as the boundary conditions are varied. Plasma evolution with both the constant loop voltage and constant current constraints are investigated, each with varying boundary conditions. These runs are generally initialized with equilibrium profile and fluctuation spectra from the sustained close-fitting conducting wall state. To help understand the multiple helicity results, in Sec. 3.4 we present results of quasilinear calculations; specifically, the interaction of a single mode with the

equilibrium with varying boundary conditions is investigated. Each of a few selected modes is allowed to nonlinearly interact with an equilibrium chosen to be linearly unstable to the mode. Finally, we make preliminary comparisons with experiments, and summarize the key nonlinear results in Sec. 3.5.

3.2. CODE DESCRIPTION

a. MHD equations and algorithms

The initial value code solves the full, compressible MHD equations for a force-free, cylindrical plasma, periodic in the z direction (with periodicity $2\pi R$). The dimensionless equations advanced are

$$\partial \mathbf{A}_T/\partial t = S\mathbf{V}_T \times \mathbf{B}_T - \eta \mathbf{J}_T, \tag{3.1}$$

and

$$\partial \mathbf{V}_T/\partial t = -S\mathbf{V}_T \cdot \nabla \mathbf{V}_T + S\mathbf{J}_T \times \mathbf{B}_T + \nu \nabla^2 \mathbf{V}_T, \tag{3.2}$$

where a vector with the subscript T denotes a total vector [i.e., the mean ($m = n = 0$), and all the spatially fluctuating (m or $n \neq 0$) components are included]. The field $\mathbf{A}_T$ is the vector potential, where $\nabla \times \mathbf{A}_T = \mathbf{B}_T$, and we choose the gauge $\partial \mathbf{A}_T/\partial t = -\mathbf{E}_T$. The units of t, $\mathbf{B}_T$, S, and r are the same as in Chapter 2. $\mathbf{V}_T$ is the velocity in units the Alfvén velocity, and $\mathbf{J}_T = \nabla \times \mathbf{B}_T$. The resistivity η is measured in units of on axis resistivity η_o; ν ($=\nu_o \tau_R / a^2$, where ν_o is the characteristic viscosity) measures the ratio of the viscous damping time to τ_R. As is customary in simulations of this type, the plasma density (in units of the characteristic density ρ_o) is not evolved; the effect of density fluctuations on modal evolutions should be small.

Both viscosity and mass density are assume spatially constant. The nonlinear advective term, $-SV_T \cdot \nabla V_T$, is usually ignorable in close-fitting conducting wall runs. With a resistive shell, the small V_T assumption may not hold as the fluctuation level increases; hence, we include the advective term.

The algorithm is finite differenced radially and pseudo-spectrally (linear terms are treated in Fourier space[7] but nonlinear terms are treated in real space) in the other two dimensions. This allows easy implementation of the linear operators in implicit algorithms, while the use of the fast Fourier transform algorithm allows rapid transformation to real space, where nonlinear terms are straightforwardly handled. The implementation of the semi-implicit algorithm[8,9] (described below) is similarly simplified.

The semi-implicit algorithm removes the severe time step restrictions imposed by the shear and compressional Alfvén waves, thus permitting longer time scale nonlinear phenomena to be economically tracked. This problem is encountered whenever simulating systems in which phenomena occur with large time scale differences. It is intuitive that to faithfully track a phenomenon changing on the characteristic time scale δt (~ 1 Alfvén wave period for our problem), one cannot use time steps larger than δt. Using explicit algorithms, the systematic errors which occur by using too large a time step represent a source of free energy that drives linear numerical instabilities. For the Alfvén wave, the restriction on the allowed time step is just $\Delta t \leq \Delta / |V_A|$, where V_A is the Alfvén

wave velocity, and Δ is the numeric grid size (presumably the shortest wavelength mode that can exist in the simulation). Implicit algorithms allow a given Alfvén wave to be accurately simulated if $\Delta t \ll \delta t$. When Δt approaches or exceeds δt, the dispersion relationship of the Alfvén wave always changes sufficiently to ensure numerical stability For these cases, longer time scale phenomena (including longer period Alfvén waves) are still accurately tracked. Unfortunately, a full implicit treatment of Eqs. 3.1 and 3.2 is extremely cumbersome (except for the ηJ_T and $\nu \nabla^2 V_T$ terms, which do not give rise to the Alfvén waves) in multidimensional codes. The essence of the semi-implicit scheme is to identify and treat implicitly only the essential components of the terms that can give rise to numerical instabilities. A detailed description of this method can be found in Refs. 6 and 9.

b. Boundary conditions

The boundary conditions at $r = a$, unless otherwise specified, are as follows. The plasma is bounded by a thin resistive shell and an outer perfectly conducting wall combination similar to the linear model. Each Fourier harmonic of the vacuum fields, between the resistive shell and conducting wall, is calculated analytically (the standard modified Bessel function solutions to the scalar Laplacian in cylindrical coordinates) and matched to the plasma solution by the thin shell jump condition $[b_r'] = \tau_s \, \partial b_r / \partial t$, which is equivalent to Eq. (2.3). Using this, as opposed to the ideal boundary condition, requires no additional computing while

advancing the equations. $E_z(r = a)$ is just the applied electric field, and $E_\theta(r = a)$ is generally 0, i.e., the toroidal flux is held constant by assumption. With viscosity, the velocity boundary condition can be freely imposed as long as the radial velocity component is negative[6]. We choose the nonsymmetric components of the velocity ($\mathbf{v}$) to vanish at $r = a$, as is appropriate for a viscous plasma, so that the boundary condition does not affect the "dynamo" which depends on $\mathbf{v} \times \mathbf{b}$. The equilibrium velocity is given by $V_\theta = V_z = 0$, and $V_r = -E_z B_\theta / SB^2$. The nonzero V_r represents an adiabatic compression of the plasma column. It is required by Ohm's law for an electric-field-driven equilibrium to exist in steady state in the absence of pressure and fluctuations so as not to developing a narrow viscous layer at the wall. This is evident from Eqs. 3.1 and 3.2 since the inward Poynting flux must be non-zero to balance the resistive dissipation, which implies a nonzero $\mathbf{J} \times \mathbf{B}$ if $V_r = 0$. We assume that the radial current density also vanishes, as is appropriate if the resistive wall is insulated from the plasma, which is often the case experimentally. Moreover, the magnetic shielding properties of the resistive shell can be shown to be independent of the radial current density at the boundary (see Appendix).

c. Key simulation parameters

In the plasma the resistivity is taken to vary radially as $\eta=(1+9(r/a)^{30})^2$. The large and sharply rising edge resistivity is not only realistic, but also helps to prevent the formation of sharp velocity

boundary layers by suppressing unbalanced forces from $SJ_T \times B_T$. The magnetic Lundquist number, S, is typically $6x10^3$. The viscous term $\nu\nabla^2\mathbf{v}$ is included in the equation of motion principally for nonlinear numerical stability, although physically, ν of O(1) is probably justified[10]. We typically set ν at 2.5 with 127 radial grid points; this is, empirically, the lowest value that can be tolerated for the radial grid size, S, and Θ values used (higher S and Θ cases generally require a larger ν to radial grid size ratio) while maintaining numerical stability[10]. The aspect ratio R/a is taken to be 2.5.

Linear benchmark computations agree with analytic (inviscid) linear calculations, except that highly localized modes, and modes resonant outside the reversal surface ($-B_Z$ modes), are damped in the computation. The discrepancy is due to differences in viscosity, edge resistivity, and velocity boundary condition. Experimentally, we expect similar damping effects.

The linear benchmark results are also used as an initial guide in choosing the proper combination of numerical resolution (radial, poloidal, and axial), S, ν, R/a, and the η profile. Since using experimentally realistic values of S, ν, and R/a would require an impracticably large code, reasonable compromises are made. The final choices are based on known numerical results, current theoretical understandings, experimental evidence, and available computing resources (several hundred hours of Cray computer time have been used for this research so far). Some of the considerations are as follows. The aspect ratio should be as realistic as possible so that distances between

resonant surfaces of the dynamo modes approximate those in experiments, thus ensuring that the nonlinear coupling between modes is adequately modeled. The ranges of m and n included in the code must be wide enough so that the most important modes coupled by the dynamo modes[11] are included. Since the typical m = 1 dynamo mode spectrum peaks near na/R ~ -2 to -3, m up to 2 and -na/R up to at least 6 (usually more) are needed. Possible resistive shell modes should also be included. With these considerations and linear results as guides, numerical experiments are then carried out for fine tuning. The final considerations are that F-Θ relationship and magnetic fluctuation spectrum with a close-fitting conducting wall should approximate experimental measurements. This would indicate that initial equilibrium profile and stability characteristics are close to being realistic; these are presumed to be the most important factors influencing the plasma as the boundary is varied. In general, we find maximizing S and minimizing ν (to a degree) to be important in this respect.

Clearly, the parameters chosen based on the above considerations may not be adequate for all boundary conditions. It does, however, allow us to identify the key physical mechanisms influencing the plasma when the boundary conditions have not deviated strongly from the ideal, or for an initial period of time after a significant boundary variation. These mechanisms should remain, in varying degree, even when the boundary condition deviates strongly from the ideal. We also monitor evidence that indicates when some parameters may not be adequate. For example,

when both m = 1 and m = 2 modes are of significant amplitude, it indicates that the directly coupled m = 3 and additional m = 1 modes may need to be added in the simulation. These considerations, possible effects of S and ν scaling, and other variables that may influence scaling to realistic parameter regime will be further discussed at the end of this chapter.

3.3. MULTIPLE HELICITY RESULTS

For these runs, we generally employ 3 modes poloidally (m = 0 to 2), 43 modes axially (n = -21 to 21), and 127 points radially. In Sec. 3.3.a, we present pertinent features of a sustained RFP plasma with a close-fitting perfectly conducting wall. This case is used to compare with results of thin shell and distant wall simulations presented in Secs. 3.3.b, 3.3.c and 3.3.d. The equilibrium and fluctuation spectra from the close-fitting conducting wall state are also used to initialize the nonideal boundary runs.

a. Steady state with a close-fitting perfectly conducting wall

The ideal boundary RFP state is generated by running the code with a conducting wall boundary condition until a dynamo-sustained quasi-steady state is reached. Figure 3.1 shows the mean magnetic field and q profiles for a $\Theta \approx 1.592$ and $F \sim -0.08$ case. The parallel component of the mean electric field, $E_{||} = \mathbf{E}\cdot\mathbf{B}/|\mathbf{B}|$, is composed of the ohmic part, $\eta J_{||}$, and the fluctuation-induced electric field $E_f = -S\langle \mathbf{v}\times\mathbf{b}\rangle_{\theta,z}\cdot\mathbf{B}/|\mathbf{B}|$ (i.e., $E_{||} - E_f = \eta J_{||}$), where $\langle\ \rangle_{\theta,z}$ denotes an average over θ and z (Fig. 3.2). Near a steady state, $\nabla \times E \sim 0$ (i.e., $E_\theta \sim 0$ and E_z is nearly a spatial constant); hence,

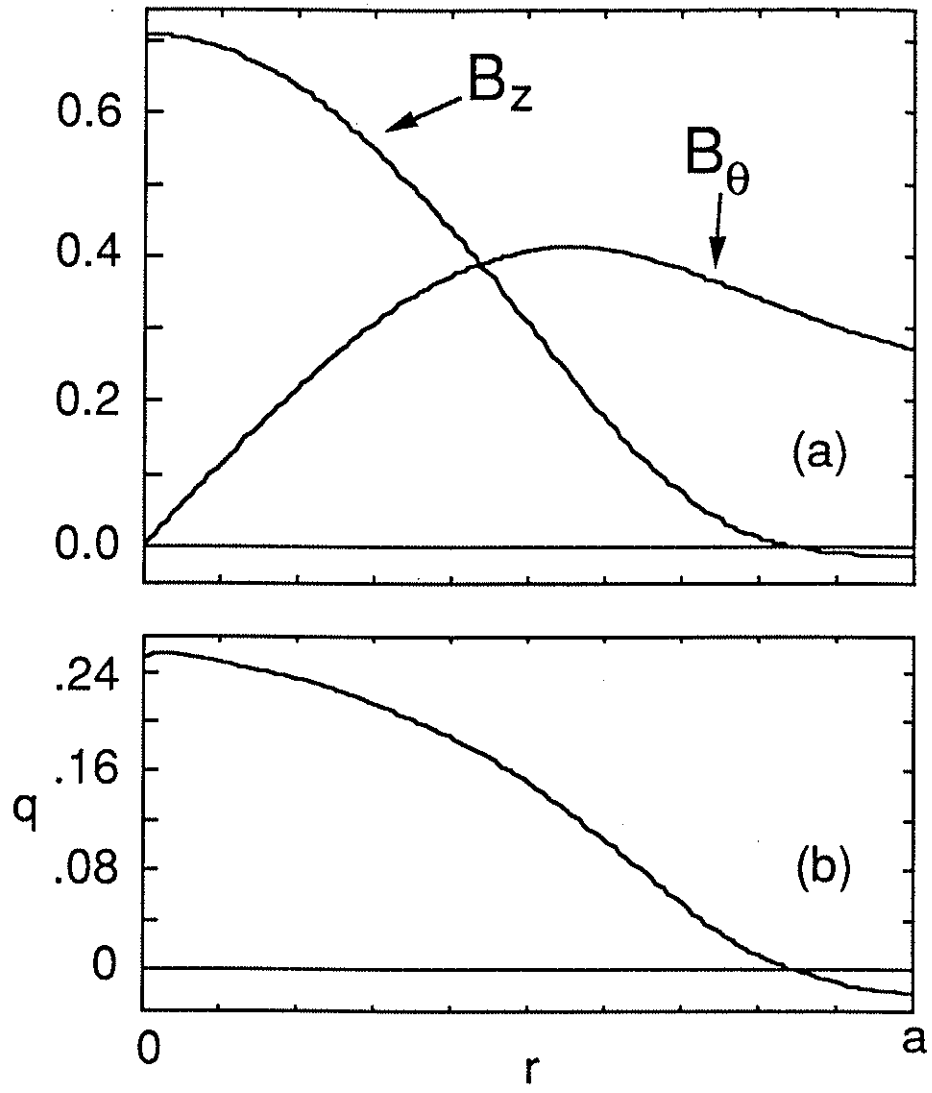

FIG. 3.1. Mean axial and poloidal magnetic field profiles (a), and q profiles (b) of the mean magnetic fields for the steady state close-fitting conducting wall case (Θ~1.59, F~-.08); mean components are averaged over the θ and z directions. The magnetic fields are in units of characteristic field strength B_o.

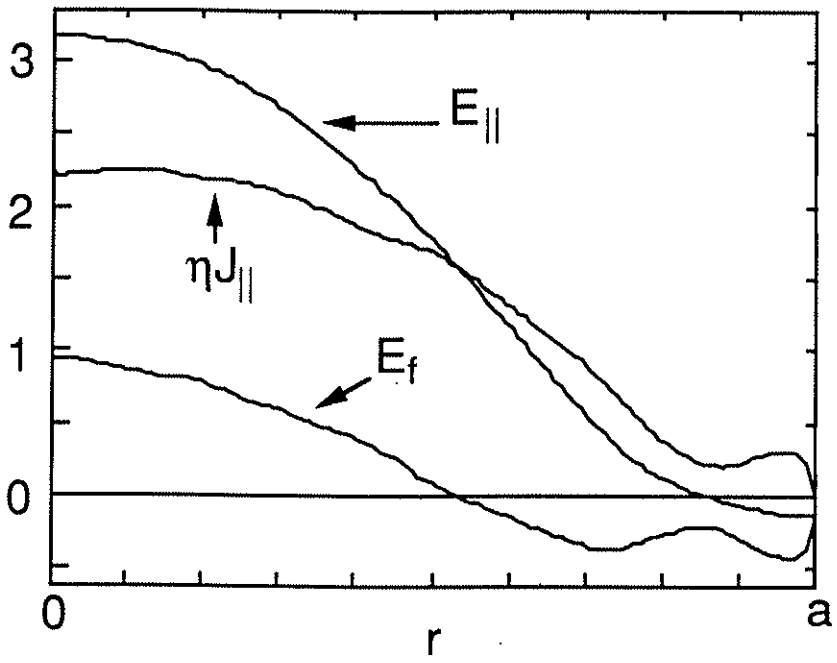

Fig. 3.2. Parallel electric field profiles for the Θ~1.59, F~-.08 steady state close-fitting conducting wall case. The total electric field, $E_{||}$, is composed of the ohmic, $\eta J_{||}$, and the fluctuation induced E_f components. Here η is in units of the characteristic resistivity η_o, and J is a nondimensional current ($\mathbf{J} = a\nabla \times \mathbf{B}$).

E is everywhere nearly equal to the applied toroidal electric field, and $E_{||}$ is just the applied $E_{||}$. Clearly, $E_{||}$ and E_f determine $J_{||}$, which in turn determines stability and the level of dynamo activity present in a force-free RFP. Hence, the sustained RFP state, even with nonideal boundary conditions, can be described based on the variations of E_f and the applied $E_{||}$.

From the radial profiles of the fields (Fig. 3.2), we see that the applied $E_{||}$ drives the plasma towards a state unstable to the $m = 1$, $n < 0$ modes. The $E_{||}$ is of a shape to create a peaked λ profile, and by itself (i.e., if $E_f = 0$), cannot produce a reversed field plasma (a well known fact[12]). The presence of E_f is necessary for reversal since $E_{||}$ reduces the $J_{||}$ (necessary for reversal) in the reversed field region (Fig 3.2).

The E_f, which not surprisingly is generated primarily by $m = 1, n < 0$ modes, is seen in Fig. 3.2 to flatten λ by current reduction near the center and enhancement near the edge. This generates reversal ("dynamo") and a more stable profile. The net flattening of the λ profile by E_f is seen in Fig. 3.3, which compares the steady state λ profiles of simulations with and without E_f. The case without E_f is obtained by running the code with all fluctuations suppressed, but with the same toroidal electric field as the case with E_f. The mode saturation is a balance between the quasilinear stabilization (as well as nonlinear coupling to stable modes[13]) of the E_f, and the destabilization by the applied $E_{||}$.

For this conducting wall case, 30% of the V_L is "anomalous", i.e., $E_f \sim 0.3E_{||}$ at $r = 0$ (see Fig. 3.2). We note, without showing, that B_z is nearly

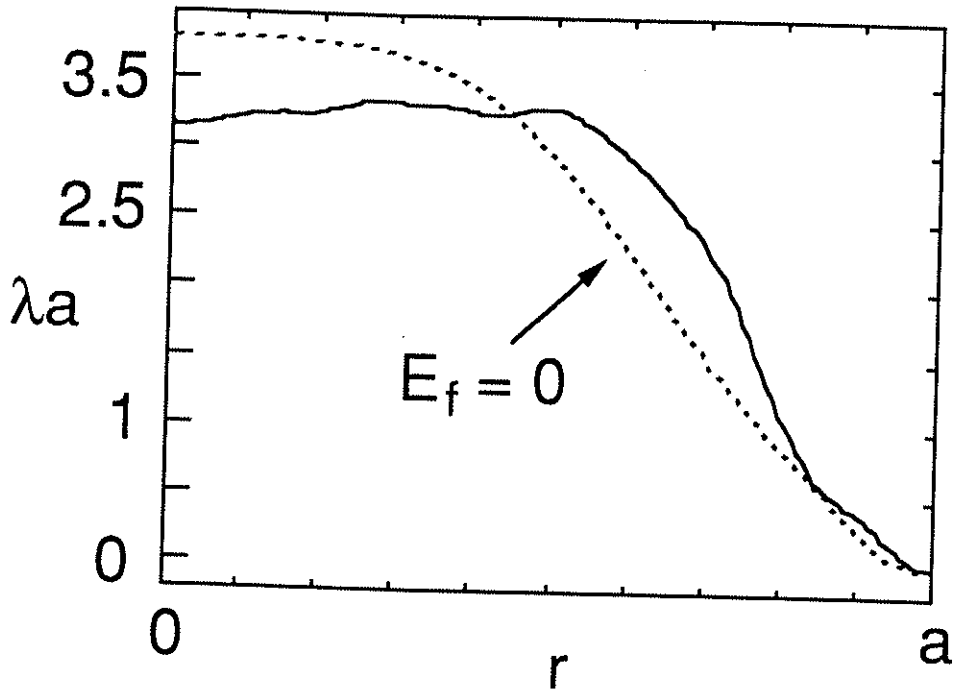

Fig. 3.3. The λ (=J/B) profiles for two different cases; one from the dynamo sustained steady state RFP (Θ~1.59, F~-.08), the other obtained from a case with fluctuations artificially suppressed. Both cases have the same applied electric field.

reversed for the case without E_f, i.e., substantial steady state poloidal current exists (as can be inferred from the λ profile as well) due to the force-free condition when an equilibrium diffusive flow is permitted to compress slowly[12] (the "paramagnetic" effect). This effect should not be ignored when considering the effect of the applied electric field.

More specifically, the effect of E_f depends on the relative strength of the positive ($E_f > 0$) and the negative portion ($E_f < 0$) of E_f. The $E_f < 0$ increases $J_{||}$, which is stabilizing to $m = 1$, $n < 0$ modes by the increased shear (with sufficient shear, equilibria at $\Theta = 1.59$ can be stable to all $m = 1$, $n < 0$ modes even without a conducting wall), and translates into deeper reversal for a given Θ. The $J_{||}$ increase is in both the toroidal (both positive and negative) and the poloidal direction (Fig. 3.1); thus, $E_f < 0$ produces the "dynamo" effect, and can also lower V_L if a constant toroidal current constraint is imposed. On the other hand, $E_f > 0$ reducess $J_{||}$. The effect is to enhance V_L if the current is held constant; the enhanced V_L prevents the $E_f > 0$ from reducing current, but weakens shear by reducing $J_{||}$ in the reversed field region.

For the close-fitting conducting wall case, the overall effect of E_f appears to lower V_L. The case without E_f has $\Theta \approx 1.55$, thus implying that if both cases have the same Θ, the case without E_f will have higher V_L. This does not violate energy conservation since the low level fluctuations with a close-fitting conducting wall dissipate only small amounts of energy; this dissipation is easily accounted for by the slightly higher mean field ohmic dissipation (due to current profile differences) of the case

without fluctuations.

Given the discussions above, it is clear that if the E_f profile can be arbitrarily tailored (not a self-consistent case), one would choose to maximize $E_f < 0$ and minimize $E_f > 0$. The $m = 1$, $n < 1$ modes would saturate at lower amplitudes, and V_L would also be lowered in comparison with the self-consistent case. Although this is purely hypothetical, it does suggest that artificial poloidal current drive schemes (e.g., neutral beam current drive) could have large beneficial effects in lowering fluctuations from the $m = 1$, $n < 0$ modes, and lowering V_L.

To distinguish the effects of various modes, in Fig. 3.4(a) we plot the contribution to E_f of different spectral bands. The dominance of the $m = 1$, $n < 0$ modes is illustrated here, and in Fig. 3.5 where magnetic energy spectra are shown. Unlike the linear calculations, it is difficult to classify the mode type of the largest mode (from Fig. 3.5, m, n = 1, -5). Figure 3.6 shows the helical flux plot for the $m/n = -1/5$ helicity. The presence of the 1, -5 magnetic island is clearly seen, suggesting a tearing mode. However, the radial flow pattern which is large at all radii and vanishes only at $r = a$ suggests a kink (the $m = 1$, $n = -5$ **v** and **b** profiles are shown in Fig. 3.7). From Ref. 11, it was shown that this mode can be nonresonant during the linear phase of its evolution, then becomes resonant via the second reconnection process[11]. The mode could also be initially resonant, then remove that resonance via a standard reconnection before starting the second reconnection. For now, it is not necessary to distinguish the individual mode types; thus, we will refer to the $m = 1$, $n < 0$ modes at

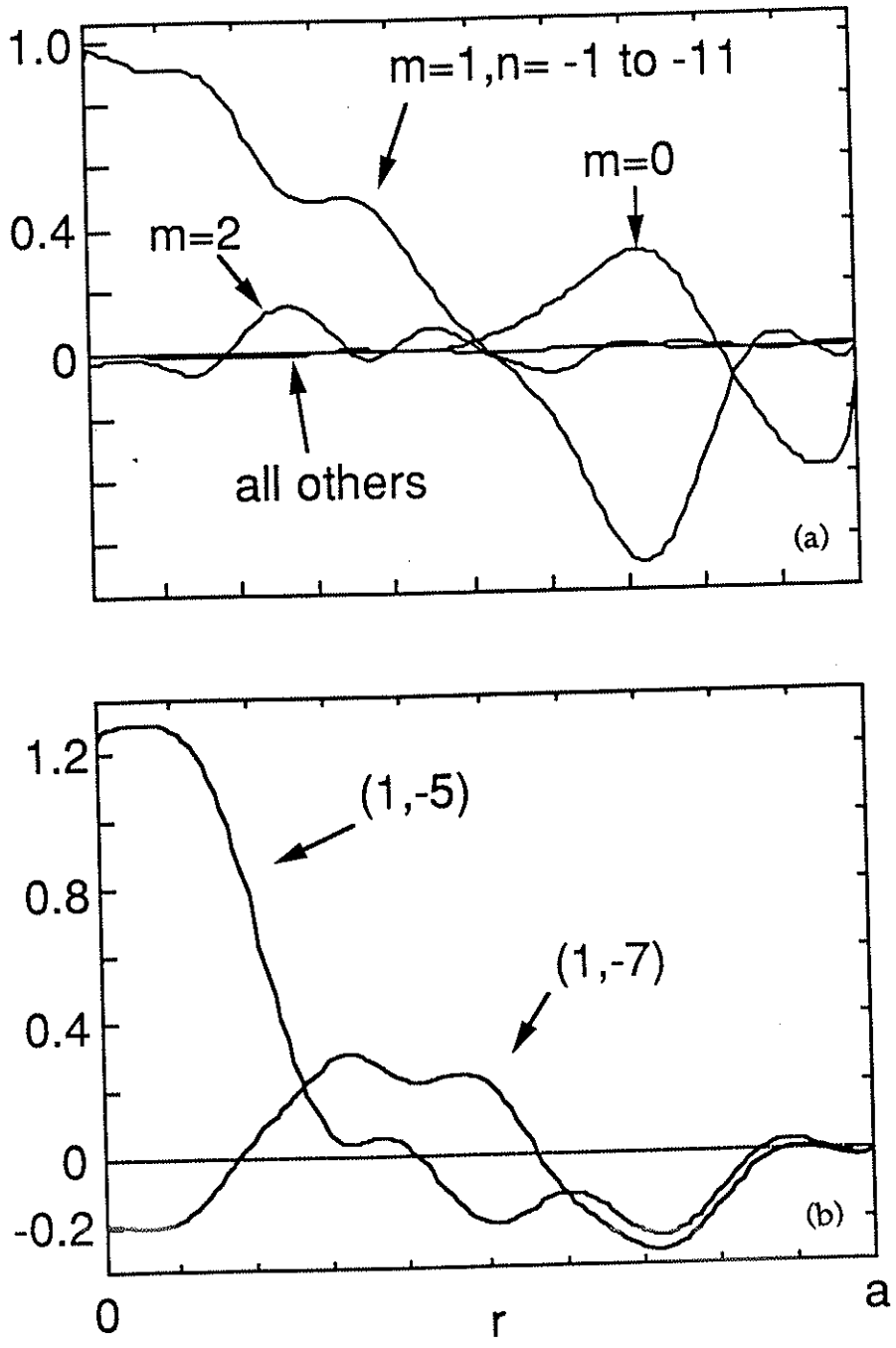

FIG. 3.4 Contributions to E_f of the case shown in Fig. 3.2 from different spectral bands (a), and contributions from only the m, n = 1, -5 and 1, -7 modes (b).

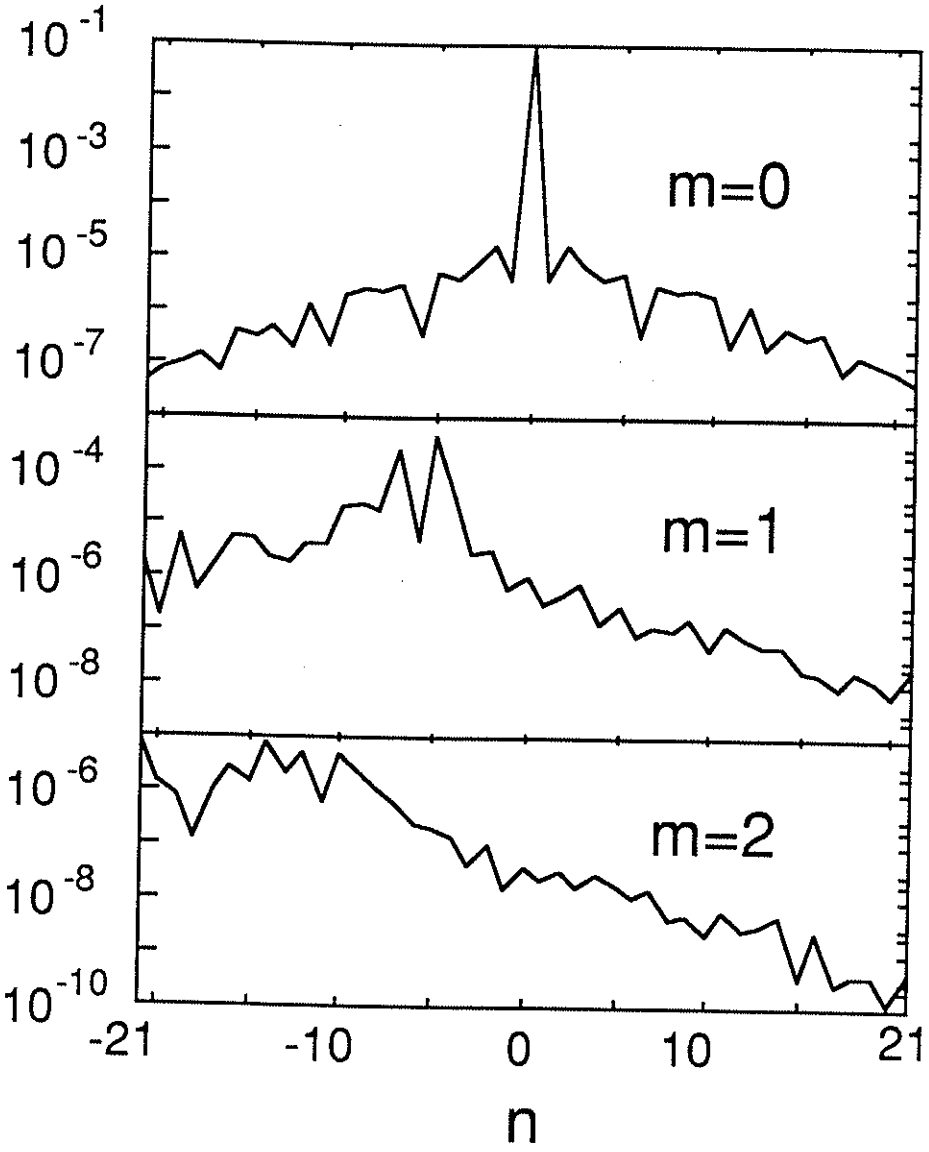

Fig. 3.5 Magnetic energy spectra of the steady state $\Theta \sim 1.59$, $F \sim -.08$ close-fitting conducting wall case. For each poloidal mode number (m = 0, 1, 2), the full axial mode energy spectrum is shown.

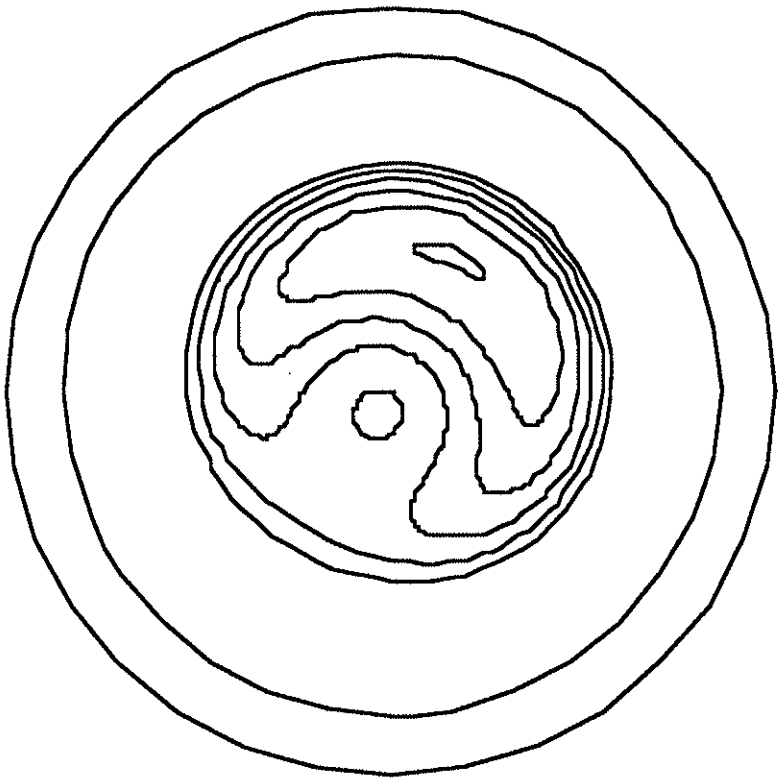

FIG. 3.6. The helical flux plot for the m/n = -1/5 helicity.

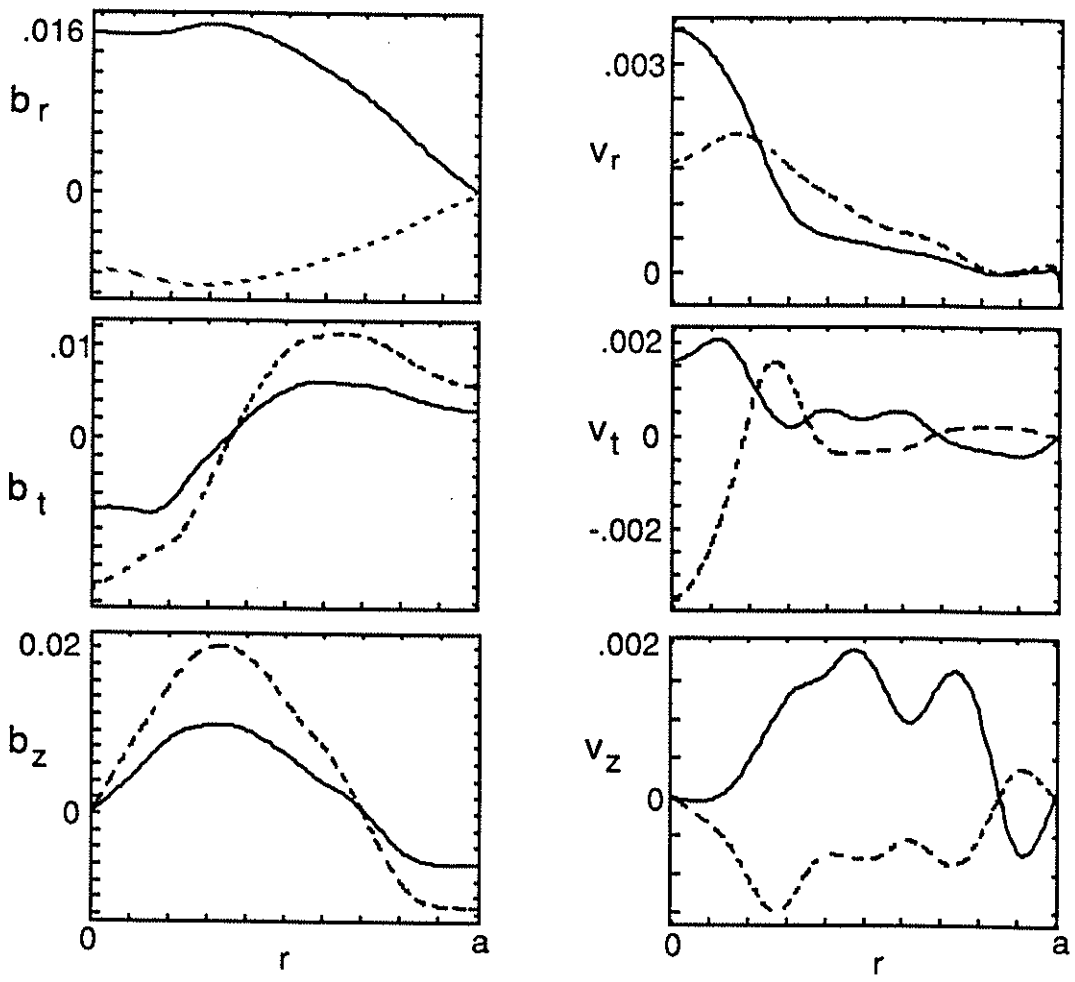

FIG. 3.7 The b and v profiles of the 1, -5 mode for the $\Theta = 1.59$ close-fitting conducting wall case at one axial position. The solid and the dashed lines represent the real and the imaginary components respectively; thus, phase information can be inferred from these figures.

$\Theta > 1.4$ only as "dynamo" modes. The m, n = 1, -5 and 1, -7 mode contributions are shown in Fig. 3.4(b). From this figure, it seems that the dynamo mode's contributions to E_f can be accounted for by a few long wavelength modes (n = -5 and -7 in this case). In general, the 1, -5 contribution is large at this aspect ratio, but it is not clear which of the higher $|n|$ mode (n ~ -6 to -10) contribution will be largest at any given time in a quasi-steady state. The $|n|$ spectrum can also depend on Θ, boundary conditions, ν, the η profile, etc.

The m = 0 contribution to E_f changes sign across the reversal surface; it reduces $J_{||}$ inside (but near) the reversal surface, but increases $J_{||}$ outside the reversal surface. This should steepen the λ gradient for modes resonant or nearly resonant near the axis; hence, m = 0 modes are quasilinearly destabilizing to the dynamo modes. However, the overall effect of the m = 0 modes, with a close-fitting conducting wall, is weakly stabilizing. Simulations with the m = 0 modes removed and Θ held constant yields slight increases in the perturbation magnetic energy and kinetic energy. Thus, the stabilizing nonlinear mode coupling is probably stronger than quasilinear destabilization. Nonlinear mode coupling through m = 0 modes is stabilizing by cascading energy to smaller scale, stable, more dissipative modes[13]. This is evident from the m = 0 broadening of the m = 1 spectrum [see Fig. 3.8(a)]. The broadened spectrum, in turn, more efficiently cascades energy to $m \neq 1$ modes. Without the m = 0 modes, the m = 1 spectrum can only be broadened by coupling with m = 2 modes, and the mode competition process (i.e.,

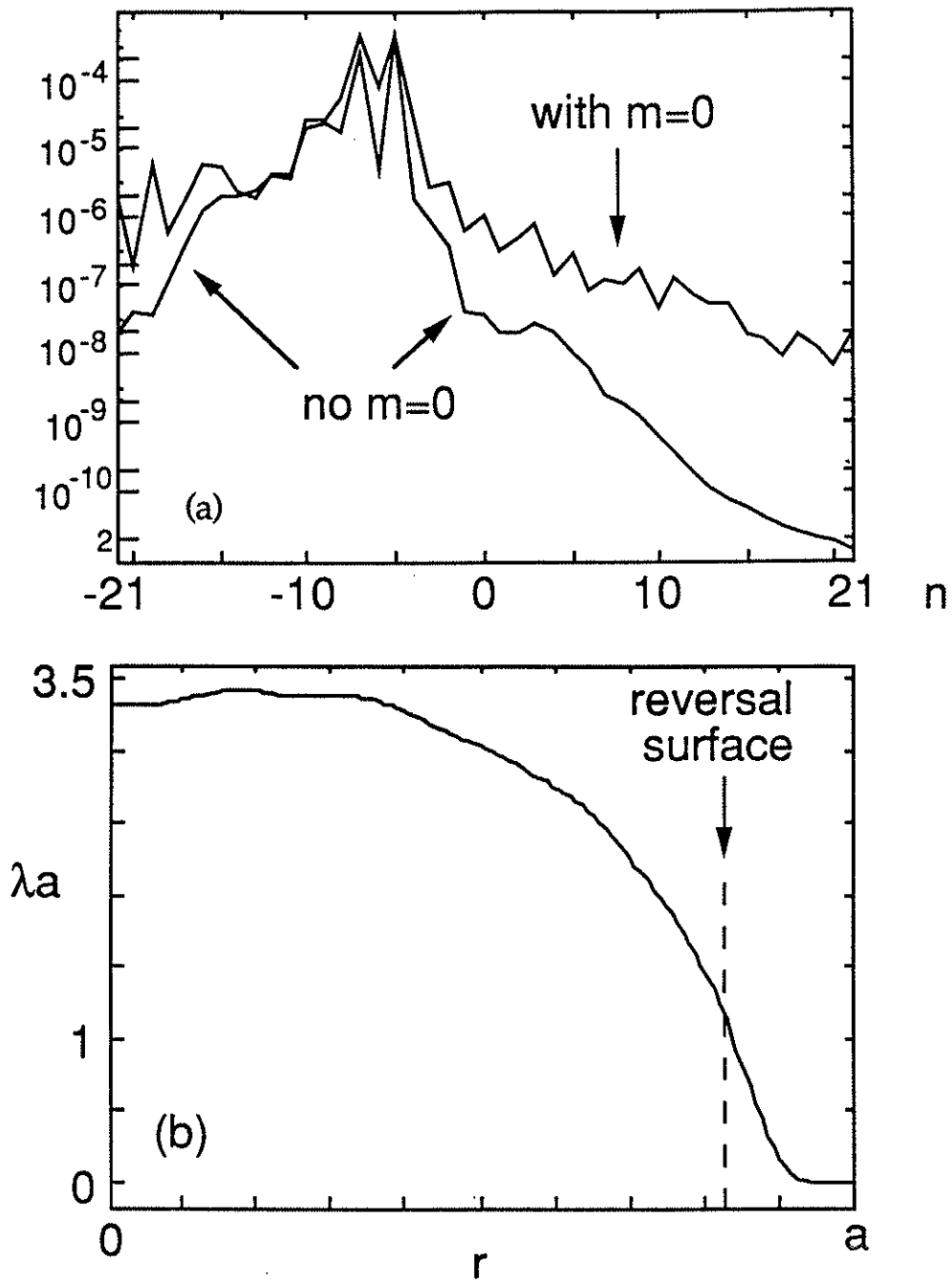

Fig. 3.8. Comparison of the m = 1 mode spectra between two close-fitting conducting wall cases (a): one with m = 0 modes intact, the other without m = 0 modes. The λ profile for the case without m = 0 modes is shown in (b).

destabilization of one m = 1 mode by another through quasilinear modification of the mean field). However, coupling of m = 1 modes through m = 2 as an intermediary is weak since m = 2 mode amplitudes are small, and the mode competition process is not as efficient in broadening the mode spectrum as nonlinear mode coupling[13]. The mode competition process principally determines the distribution of energy among the few dominant dynamo modes; hence, it plays a large role in shaping E_f. A more precise comparison of the nonlinear and quasilinear effects may be impossible since the nonlinearly modified m = 1 spectrum tends to alter quasilinear interactions involving m = 1 modes. The two effects are necessarily convoluted. Fortunately, the clear dominance of the m = 1, n ~ -5 to -7 modes is not altered by the m = 0 presence, as shown in Fig. 3.8(a) Thus, qualitatively, the key quasilinear interaction between the dynamo mode and the applied electric field is unaffected by nonlinear mode coupling to the m = 0 modes.

As for the cause of the m = 0 perturbations, both quasilinear and nonlinear interaction with the dynamo modes can be important. The dynamo modes generate reversal (a requirement for the m = 0 modes to be unstable), and quasilinearly steepen the equilibrium λ gradient near the edge, causing the m = 0 modes to be linearly unstable [cf., Fig. 3.8(b)]. In addition, the dynamo modes can drive the m = 0 perturbations by nonlinear mode coupling[13]. Both causes, however, require the presence of substantial dynamo modes; thus, m = 0 modes can help saturate, but are unlikely to affect the stability of unstable m = 1 modes. Consequently, the

$m = 1$ spectrum can be broadened but not noticeably shifted by the $m = 0$ presence. (However, $m = 0$ modes may stabilize some modes more than others.)

Given the discussion in this section, it would appear that a fully relaxed Taylor state (λ = constant) cannot be a steady state in typical RFP Θ ranges. The E_f and its dynamo effect could exist only if the dynamo modes remain slightly unstable in steady state. This is not the case for the Taylor state.

b. Thin-shell simulation with constant current

If the conducting wall is removed (to a radius of 10a) to treat the "thin shell problem", the fluctuating magnetic and kinetic energy increase by about one and two orders of magnitude respectively. They appear to reach a plateau in about a shell time for $\tau_S = 0.1\tau_R$, as shown in Fig. 3.9. The Θ value (the normalized current) is held constant at 1.592. The n spectrum of $m = 1$ fluctuations remains similar to the initial state, peaking at $n \sim -5$ (Fig. 3.10). The loop voltage, Fig. 3.9, also increases with time (~ factor of 5 in one τ_S), but develops giant excursions near the end of the computation (at $t \sim 1.2\tau_S$). This is not surprising in view of the parallel electric field profiles shown in Fig. 3.11. The E_f component is now about seven times the resistive term ($\eta J_{||}$). Thus, modest variations in **v** or **b** can, via Ohm's law, induce large current changes unless V_L adjusts accordingly. To balance the current reduction of E_f (constant current constraint), V_L is now highly anomalous.

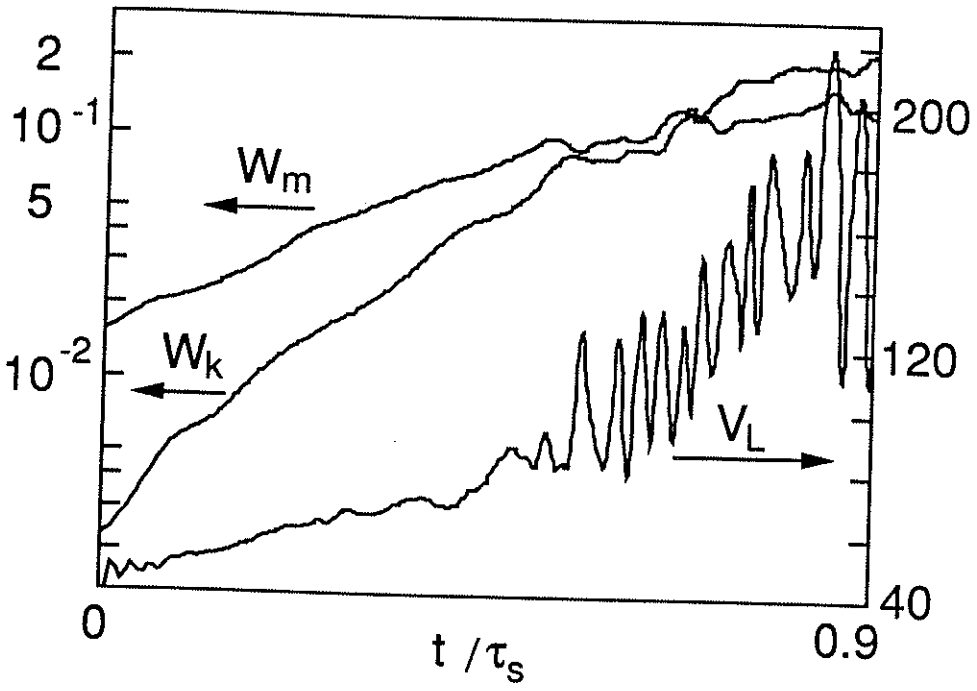

FIG. 3.9. Constant Θ evolution (initialized with a close-fitting conducting wall steady state) with a thin shell: total radial magnetic energy ($W_m=\int 0.5(b_r/B_o)^2\, d^3(r/a)$, where B_o is the characteristic field strength), total kinetic energy (W_k, same units as W_m), and loop voltage [$V_L = (2\pi R/a)E_Z(r=a)$] versus time.

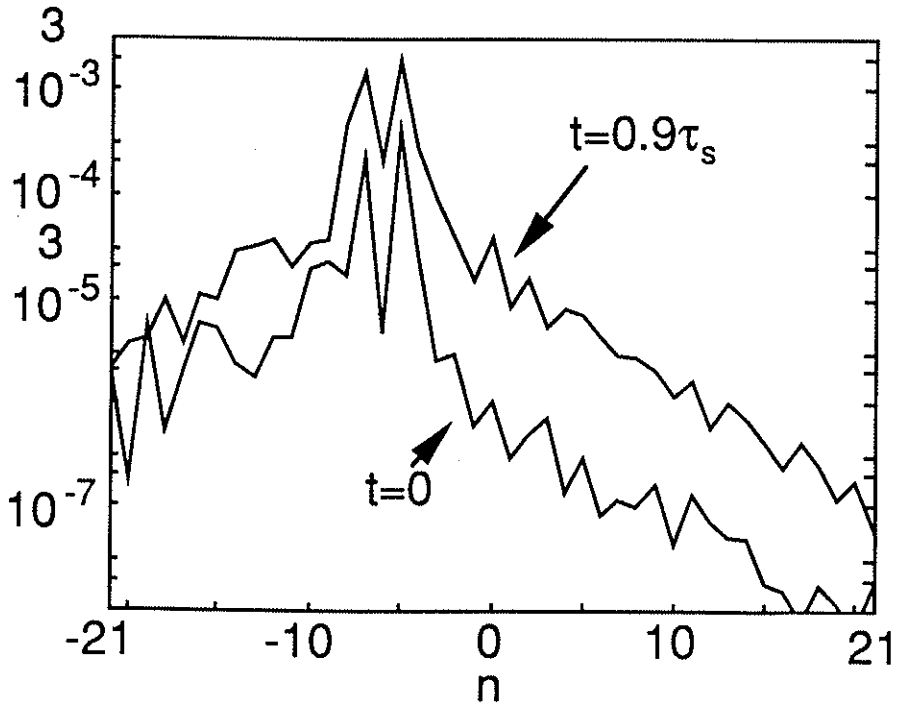

FIG. 3.10 Comparison of m=1 magnetic energy spectra at two different times of the thin-shell constant Θ case shown in Fig. 3.9.

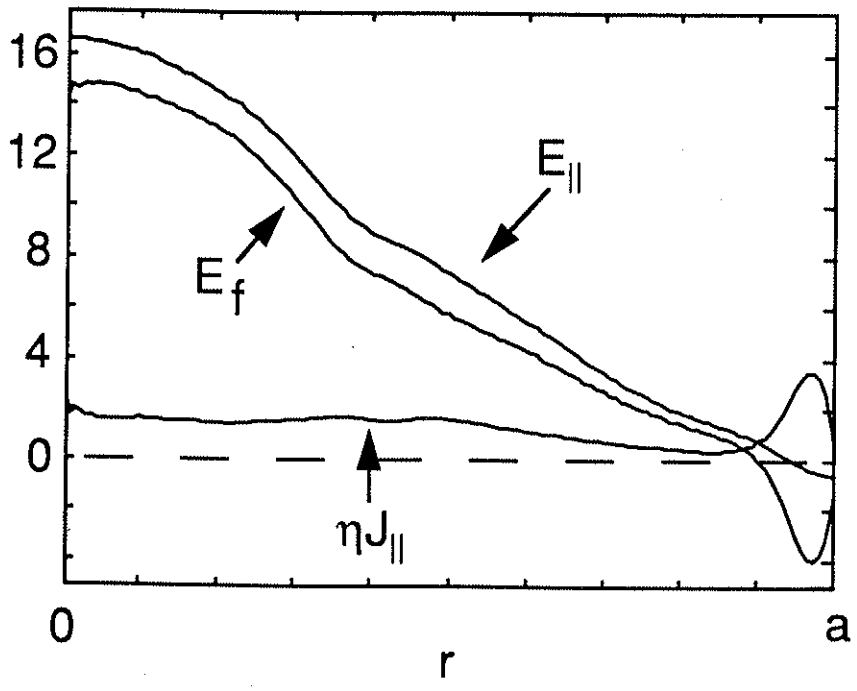

FIG. 3.11 Parallel electric field profiles at $t=0.9\tau_s$ for the constant Θ thin shell run in Fig. 3.9.

The dynamo modes, from quasilinear effects, are more strongly affected by the boundary than the linear theory implies. This is due mainly to an enhanced E_f that is mostly in the $E_f > 0$ region (Fig. 3.11), which is the opposite of our preferred hypothetical case. The enhanced $E_{||}$ mainly balanced $E_f > 0$ over most the minor radius, leaving the $J_{||}$ profile relatively unchanged. The enhanced edge current drive of $E_f < 0$ deepens reversal somewhat, so that the reversal parameter F $(= B_Z(a)/\langle B_Z \rangle)$ evolves from -0.08 to -0.15. The increase in shear, however, is insufficient to compensate for the loss of the conducting wall stabilization. The dynamo modes, $|E_f|$, and V_L thus grow to a large amplitude.

In Fig. 3.12(a) we plot the contribution of different spectral bands to E_f. The large m = 0 contribution is mainly in a direction to reduce $J_{||}$ in the periphery; thus, m = 0 modes increasingly destabilize the dynamo modes quasilinearly. However, the overall effect of m = 0 modes is strongly stabilizing; removal of m = 0 modes yields a twenty-fold increase in V_L. Thus, nonlinear mode coupling is probably the dominant stabilizing influence. The dynamo mode's contributions to E_f is again dominated by only a few modes [the n = -5 and -7 modes are shown in Fig. 3.12(b)]. The evolution of the n = -5 contribution is similar to that of the entire E_f, becoming primarily current reducing.

We generally do not observe large m = 1, n > 0 external kinks, as perhaps expected from linear theory. However, preliminary runs at higher Θ values, which produced deeper reversal, do indicate larger n > 0 kinks. They may also appear in the low Θ runs if the computations

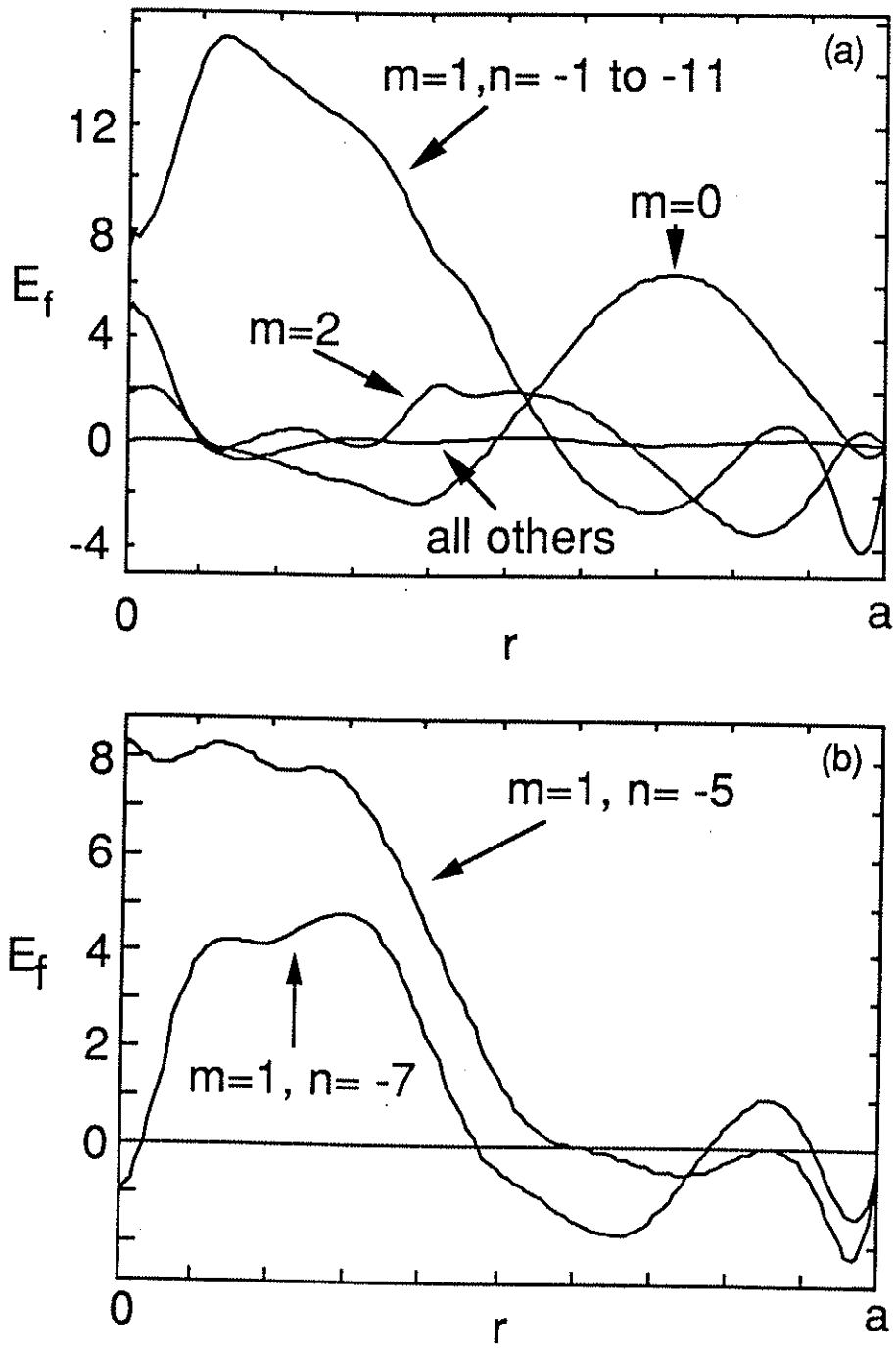

FIG. 3.12 Contributions to E_f of the case shown in Fig. 3.11 from different spectral bands (a), and contributions from only the m, n = 1, -5 and 1, -7 modes (b).

proceeded longer, but they are clearly not the most important modes. Single helicity results show that these modes also reduce $J_{||}$. Since these modes only exist with reversal, i.e., dynamo action required, their quasilinear interaction with the equilibrium is not expected to exceed that of the dynamo modes.

c. Thin-shell simulation with constant loop voltage

If the loop voltage is held constant for the initial conditions used above, Θ decreases in time as expected. Early in time the growth of fluctuations deepens reversal. However, by $t = 0.5\tau_s$ (with $\tau_s = 0.1\tau_R$) Θ has decreased to 1.37 and reversal is lost as the central current reduction overwhelms the edge current drive. After this time the $m = 1$ mode spectrum evolves through a sequence of modal growth, saturation and decay as lower $|n|$ modes become unstable as shown in Fig. 3.13. The dominant $m = 1$ mode shifts from $n = -5$ to $n = -1$ as q rises to order unity at all radii (cf., Fig. 3.14). As the symmetric part of the profile evolves, the dominant modes generally correspond to those that are linearly unstable (i.e., quasilinear interaction is sufficient to explain the behavior of the plasma here). The evolution of the plasma slows down after the $m = 1$, $n = -2$ mode becomes dominant. To shorten the run, after $t \sim 0.1\tau_R$, which corresponds to the beginning of Fig. 3.13(b) time traces, τ_s was changed to $.02\ \tau_R$.

The plasma current does not smoothly decay; it tends to step down as shown in Fig. 3.15. The hesitations in current decay may indicate existence

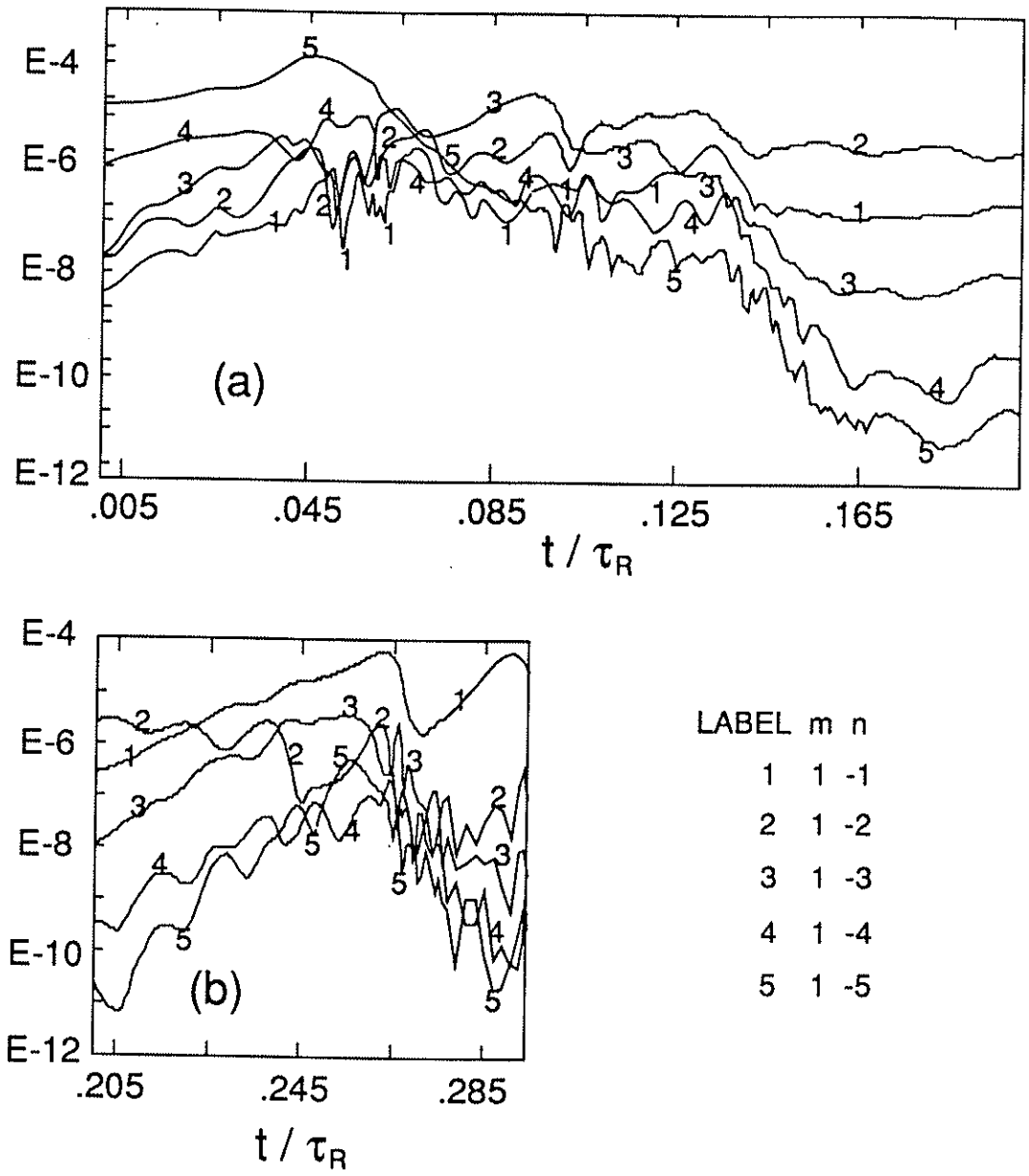

Fig. 3.13 Constant V_L modal evolution with a thin shell: (a) radial magnetic energy of various modes versus time up to $t = 0.2\tau_R$, (b) continuations of the case in (a), but with τ_s changed from $0.1\tau_R$ to $0.02\tau_R$. The radial magnetic energy is in arbitrary units for relative comparison only.

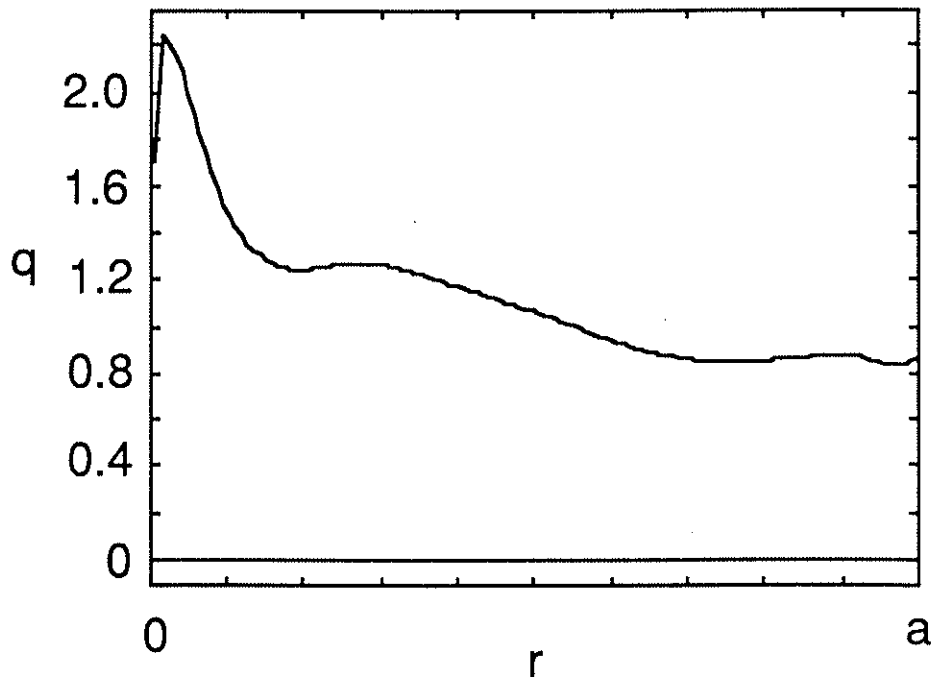

FIG. 3.14 The q profile at t = 0.295 of the constant V_L thin-shell case.

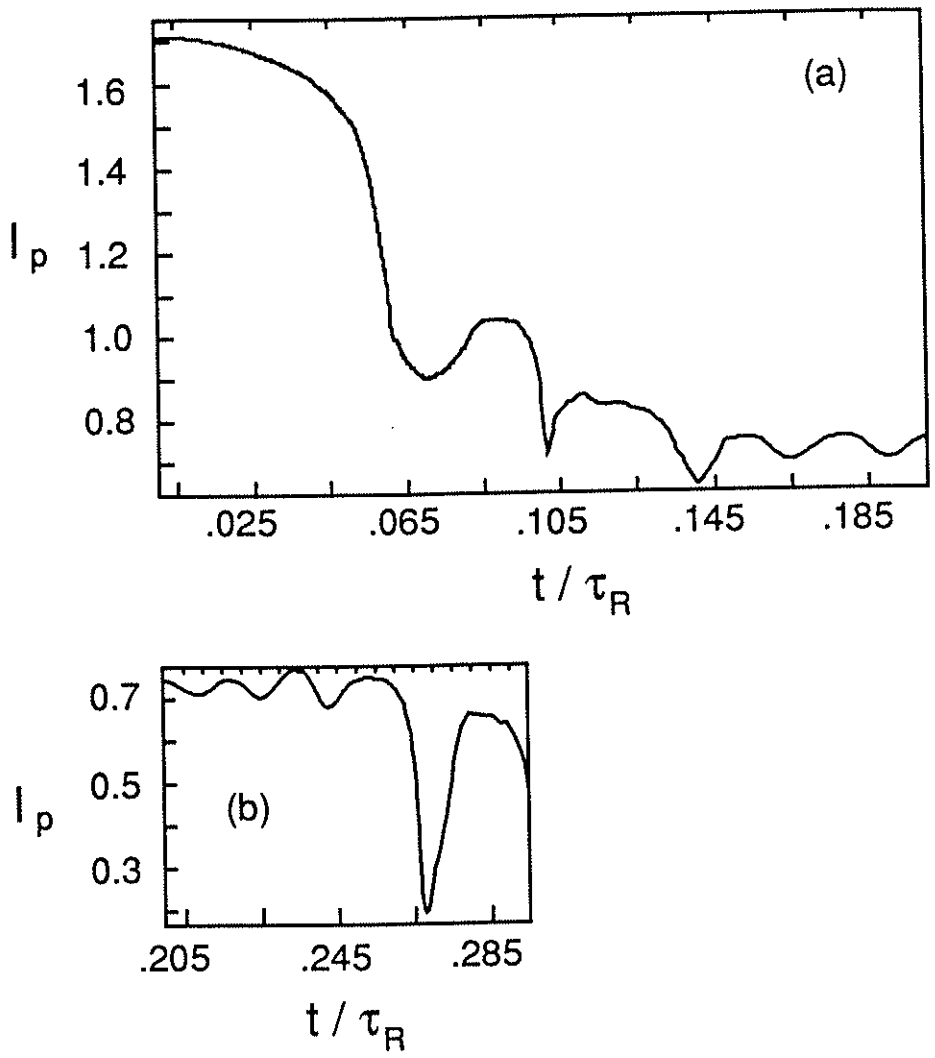

FIG. 3.15 Plasma current (I_p) evolution in the constant V_L thin-shell case. The current is just $\pi \langle J_z \rangle$.

of narrow stable windows of operation in the nonreversed $q < 1$ regime [ultra low q (ULQ) tokamak[14,15]], or may simply be due to a time delay during transitions between dominant modes. This case warrants additional investigation in the future.

Interestingly, when V_L is held at ~ 5 times the initial close-fitting conducting wall state with the plasma initialized from the $t \sim 0.9\ \tau_R$ state of the constant Θ thin-shell run, reversal was lost anyway ($\tau_s = .01\tau_R$). This indicates that steady state operation with a thin-shell may not be possible even with high loop voltage.

d. Distant conducting wall simulation with constant current

Although the distant wall and the thin shell problems are classified as distinct, the same physics determines their behavior. When the conducting wall is placed close to the plasma boundary, the fluctuations and V_L saturate at lower amplitude than in the constant Θ thin-shell simulations. To track the dependence of V_L on the wall position, r_w, we expand the wall slowly during some runs. The total electric field is in a relative quasi-steady state during the simulation (deviations of the total electric field from a curl-free steady state is much smaller than the amplitude of the electric field). Individual modal behavior for the dominant modes is also relatively quiescent, i.e., $\partial/\partial t \sim 0$. Hence, the boundary condition, Eq. (1), is independent of τ_s and this case is relevant to the experimental situation of a plasma separated from the wall by limiters. From Fig. 3.16 ($\tau_s = .01$ for the case shown, but $\tau_s = .002$ and 0.1 cases

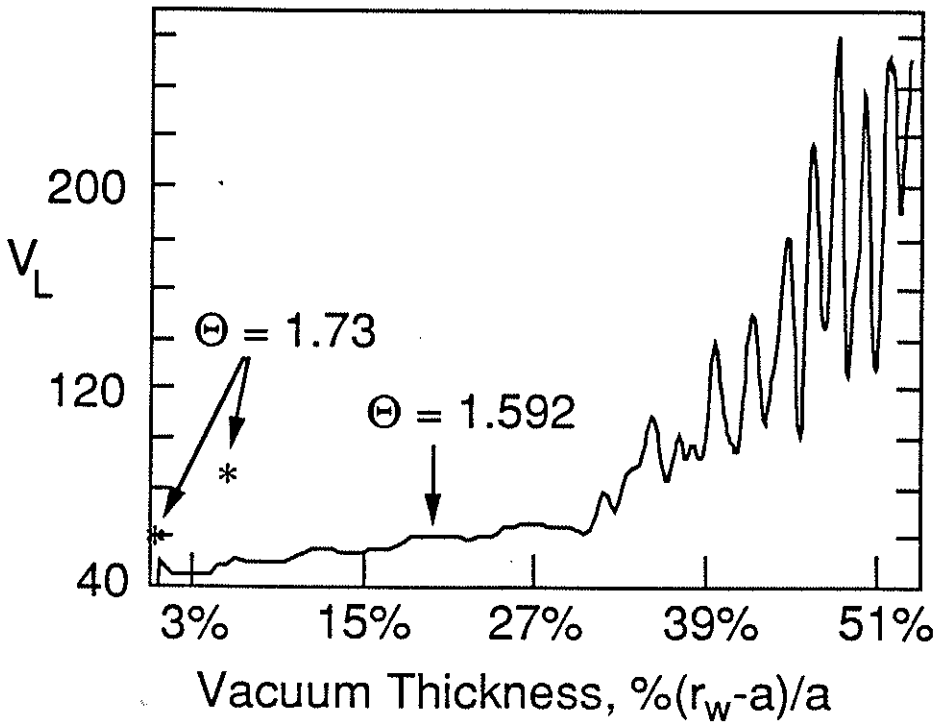

FIG. 3.16 V_L versus vacuum region thickness for two cases where the Θ is held constant while the vacuum region is expanded. The two cases have different Θ values (1.592, and 1.73). Only 2 points are shown for the Θ = 1.73 case.

behaved similarly), we see that V_L rises with r_w, increasing dramatically beyond $r_w \sim 1.33a$, at which point oscillations in V_L onset. These oscillations tend to affect only the edge electric field and current density, helping to keep the total current constant. Figure 3.17 shows the electric field profiles at $r_w = 1.15a$; the rise of the current reducing part of E_f can already be seen.

At higher Θ values the rise in V_L is more dramatic. At $\Theta = 1.73$, V_L rises by 50% as r_w increases from a to 1.05a (cf., Fig. 3.16). This is to be expected since at higher Θ values V_L and its destabilizing influence is necessarily higher to start with. The necessity for E_f to be effective in increasing shear is similarly greater. From the earlier results at lower Θ, this implies a greater reliance on the conducting wall for stability.

3.4. QUASILINEAR CALCULATIONS

These calculations are performed to help identify the role of the quasilinear interaction in the various nonideal boundary effects discussed earlier. The quasilinear effects that are self-induced by a single mode will now be investigated. Since E_f principally consists of only a few modes, one might expect quasilinear behavior to mimic the fully nonlinear runs. This is not the case.

The simulations are performed by initializing the runs with a single mode. The nonlinear MHD equations guarantee that modes with other helicity will not be generated. By choosing the spectrum of modes possible in the code judiciously, other modes of the same helicity can also be

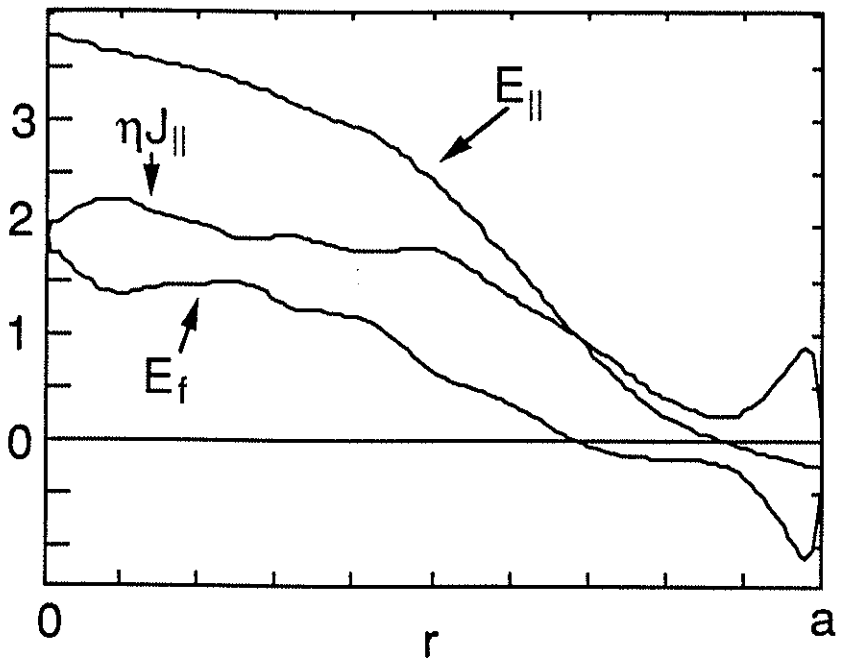

Fig. 3.17 Parallel electric field profiles for a vacuum region thickness of 15% for the $\Theta = 1.592$ distant wall case.

eliminated, leaving only one mode evolving in time.

a. Dominant dynamo mode

For this calculation, the equilibrium is initialized with the case without E_f (nonreversed) which was discussed in Sec. 3.3a. A small m = 1, n = -1 perturbation is added and allowed to grow. The aspect ratio R/a is 0.5, i.e., the plasma column is shortened by a factor of 5 as compared with the multiple helicity runs; hence, the 1, -1 mode is equivalent to the 1, -5 mode of earlier discussions. The small aspect ratio reduces the size of the code. This is not permitted for the multiple helicity runs since the spacing between resonant radii, and hence the interaction of these modes, is altered. The initial boundary conditions take a close-fitting conducting wall and hold Θ at ~ 1.55. Subsequently, after the 1, -1 mode has grown and saturated, the conducting wall radius is slowly expanded. The quasilinear run is more dynamic near the origin (due to an equilibrium which is highly unstable to the 1, -1 mode resonant near the origin); hence, ν is raised to 4 for numerical stability. The nonlinear velocity advection is suppressed to prevent the nonlinear generation of other modes; this term shows strong mode coupling near the origin and can grow other modes from numerical noise through coupling with the dynamic 1, –1 mode.

The initial evolution with a close-fitting conducting wall suggests the mode is a resistive kink. The linear growth rate is of $O(S^{2/3})$, and the initial reconnection process can be seen in Figs. 3.18(a) and (c) where the

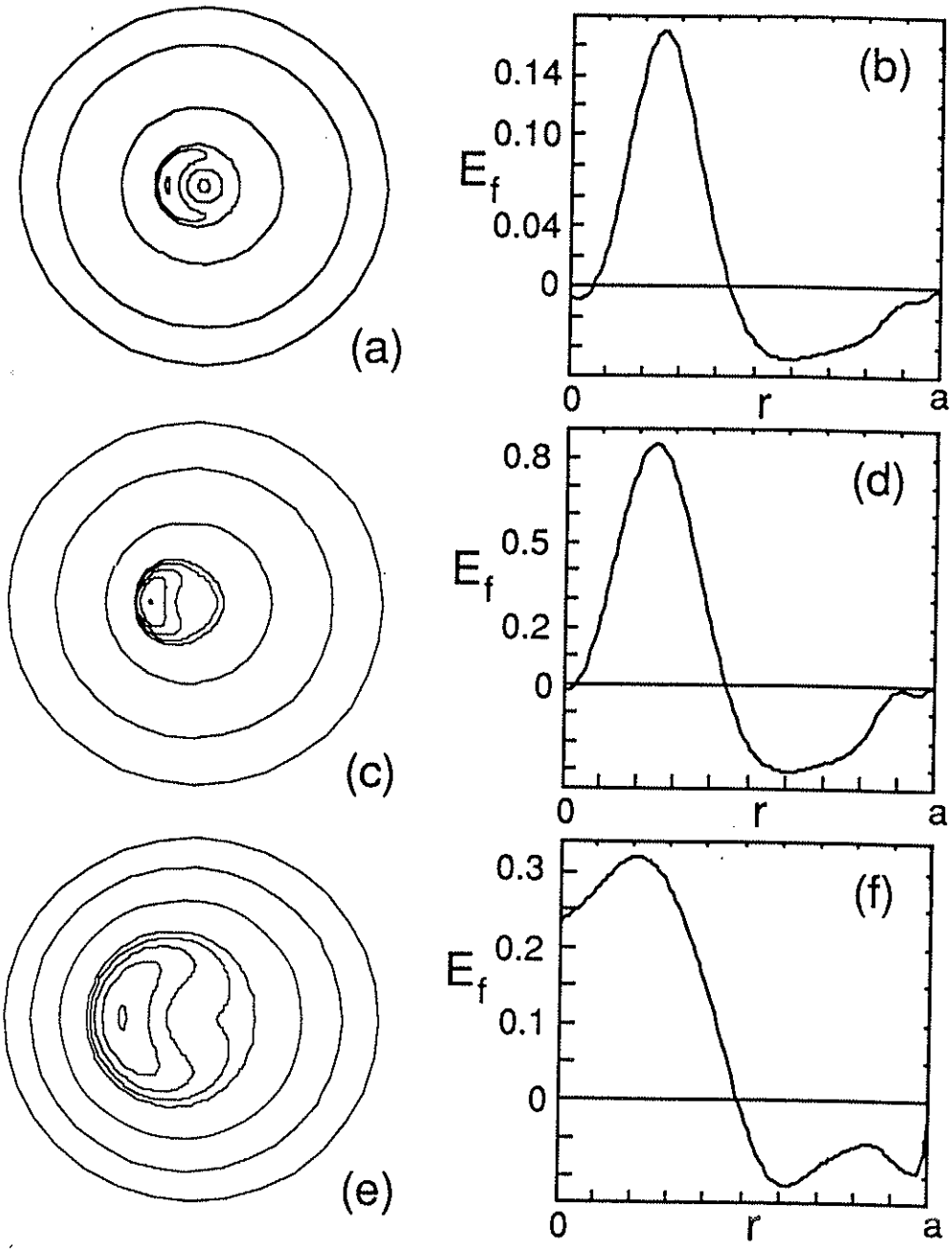

FIG. 3.18 Quasilinear evolution of the 1, -1 mode with R/a = 0.5 and close-fitting conducting wall: (a), (c), and (e) show helical flux plots at three different phases of the evolution; (b), (d), and (e) show the corresponding E_f profiles.

magnetic axis is expelled as the 1, -1 island reconnects to the center. The on axis radial magnetic field perturbations [$b_r(r=0)$] corresponding to the helical flux plots of Figs. 3.18(a) and (b) are ≈ .005 and .01 respectively. This aspect of the mode evolution is fairly standard. Afterwards, the mode continues to grow (with the same growth rate) as a nonresonant kink, and then finally saturates with radial magnetic energy about one order of magnitude larger than when the island reconnected. Not surprisingly, without nonlinear stabilization, the magnitude of b_r (~ .025 at r = 0) is larger than in the multiple helicity case (~ .017 at r = 0). No second reconnection is seen in this case [Fig. 3.18(e)]; thus, the 1,-5 island seen in Fig. 3.6 probably reconnected from multiple helicity effects. The E_f profiles corresponding to each of the helical flux plots of Fig. 3.18 is shown in Figs. 3.18(b), (d), and (f). The E_f initially drives $J_{||}$ on axis, becoming current-reducing as the mode evolves into a kink. Although the final state is a kink, E_f changes sign across the minor radius (which tends to flatten λ near the region where E_f crosses 0) as the nearly divergence-free flow resistively diffuses through the helically distorted steady state magnetic field. The distortion of the flow field from the boundary (v = 0) probably leads to the change in sign of E_f.

As the conducting wall radius is slowly expanded, the 1, -1 kink grows, but saturates at r_w ~ 1.2a with only a factor of 3 increase in the radial magnetic energy (Fig. 3.19). This is due to a E_f profile which does not become primarily $J_{||}$-reducing (Fig. 3.20), unlike the E_f or even just the 1, -5 contribution to E_f of multiple helicity runs. Consequently, the V_L is

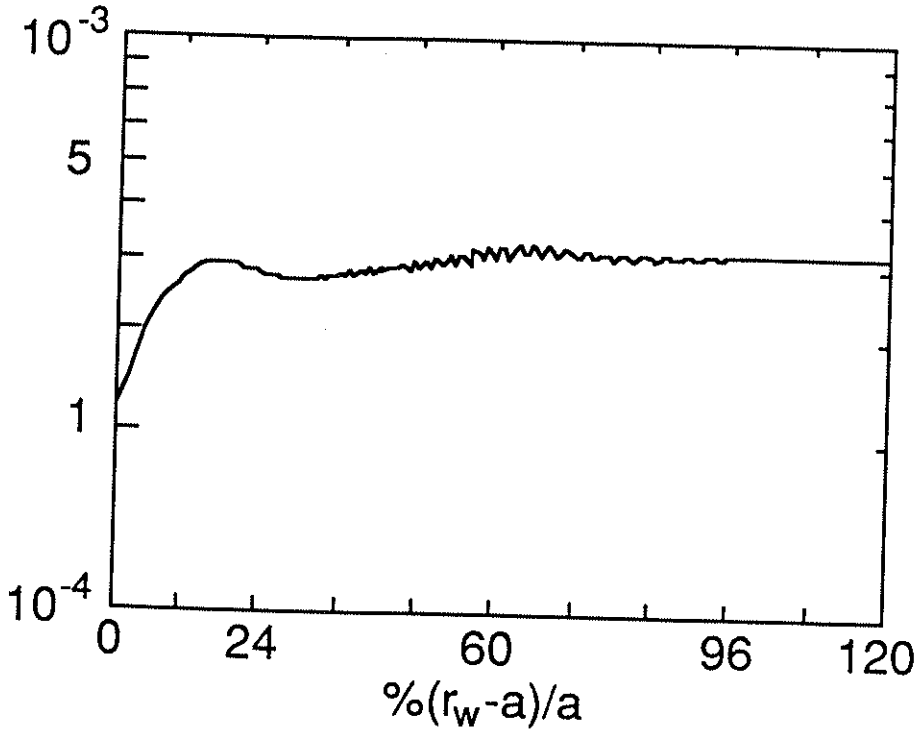

Fig. 3.19 Quasilinear evolution of the 1, -1 mode in a distant wall simulation. The mode energy is seen to saturate for vacuum regions larger than about 10%.

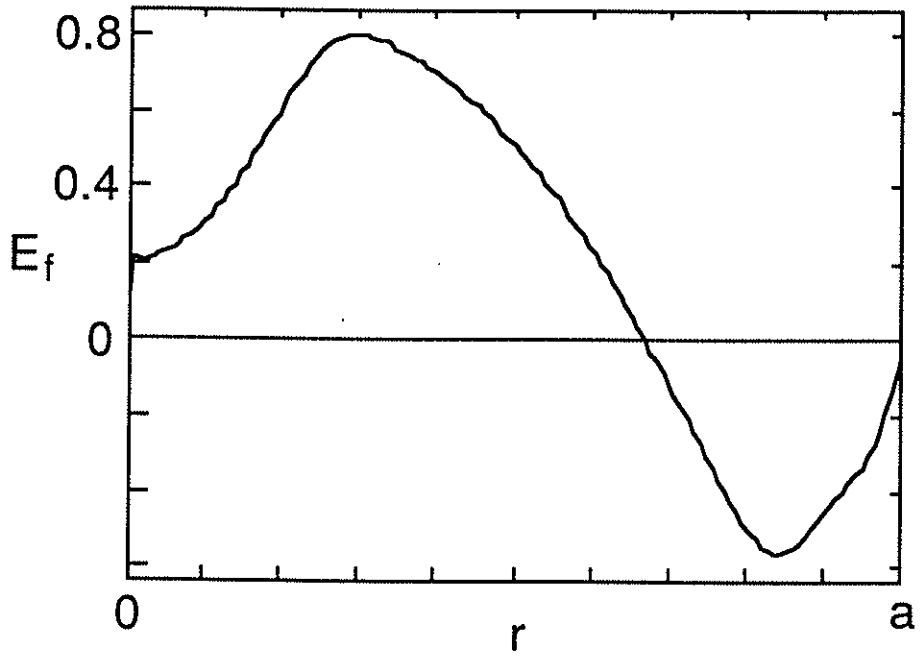

Fig. 3.20 The E_f profile due to the satuated 1, -1 mode for $r_w = 2.2$ (vacuum region of 120%).

minimally affected even with r_w at 2.2a. This result strongly suggests that an unstable E_f profile (one which primarily reduces $J_{||}$) is a result of quasilinear interactions (i.e., mode competition) between dynamo modes, which also suggests that aspect ratio effects may be large. Unlike the single mode evolution, the growth of the dynamo modes as a group do not modify the equilibrium so as to seek the stable state linearly predicted to exist for these modes. More detailed understanding of the dynamics of mode interaction is necessary to understand this behavior. Interestingly, the toroidal field self-reverses when the vacuum region reaches ~ 20% (Fig. 3.21); thus, dynamo action requires only a single helical mode given a large enough vacuum region.

b. ULQ tokamak kinks

In an earlier section (Sec. 3.3.c), we suggested that multiple-helicity, constant V_L, thin-shell evolution is composed of a sequence of quasilinear single mode evolutions. This is more clearly illustrated in this section where only a single ULQ tokamak mode is permitted to exist, and interact with the mean field. As an example, we show the evolution of the m, n = 1, -2 mode with R/a = 2.

Since this mode is basically a global kink, details of the current profile, S, η profile, etc. are not crucial to its evolution. We choose $\tau_S = .02\tau_R$, $S = 3 \times 10^3$, 63 radial grid points, and $\eta = (1 + 9r^{18})^2$. The initial q and λ profile are chosen to be unstable to the 1, -2 mode (Fig. 3.22). This state is not a resistive steady state; hence, artificial E_θ and E_z are applied to

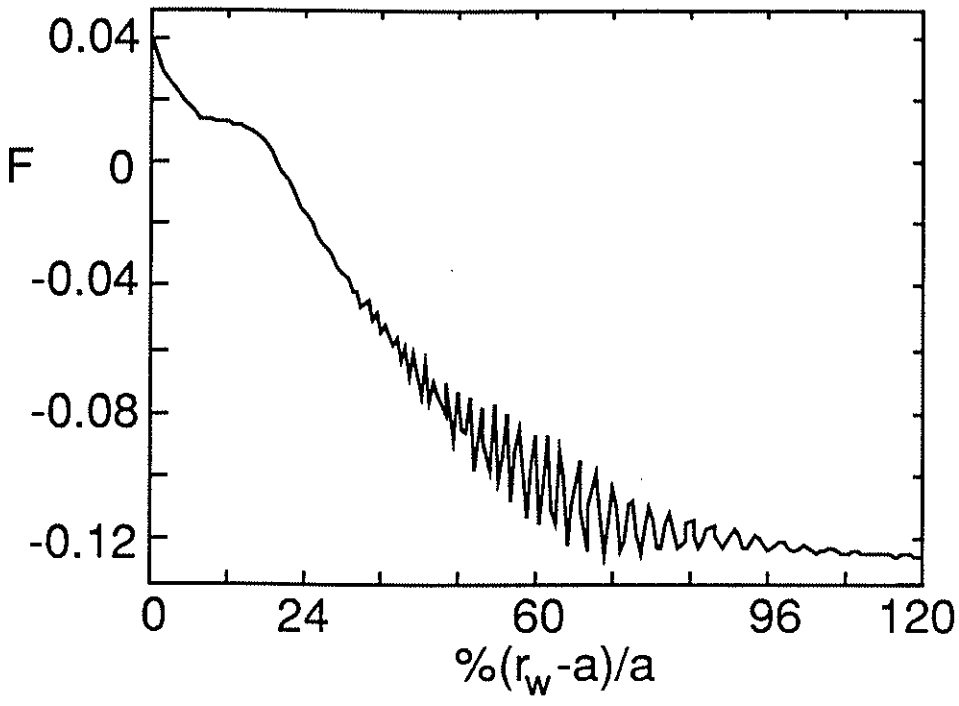

FIG. 3.21 The evolution of the reversal parameter F for the quasilinear 1, -1 mode distant wall simulation.

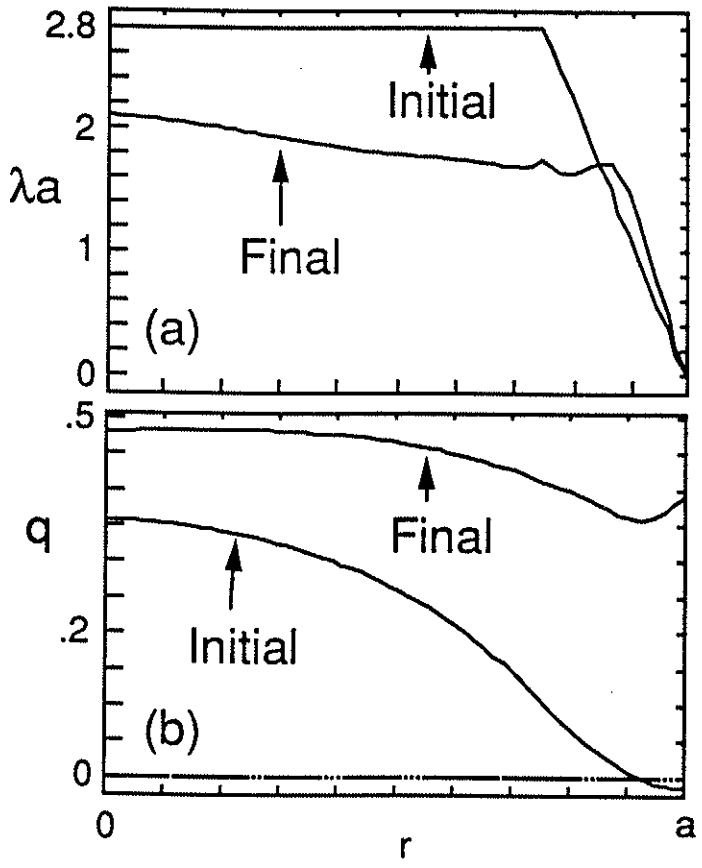

FIG. 3.22 Comparison of the initial and final λ (a) and q (b) profiles of the mean field for a quasilinear simulation. The change in the q and the λ profiles is due to the growth and saturation of a single mode (m = 1, n = -2).

counter resistive diffusion of the mean field. This ensures that the evolution of the mean field is due only to quasilinear interaction with the 1, -2 mode.

Figure 3.22 compares the q and λ profiles of the initial and final state of the simulation. The final state is a helical steady state containing a saturated 1, -2 kink. The 1, -2 kink saturates when q is raised to ~ 0.5 at all radii (by suppressing λ). This state is unstable to the 1, -1 kink, which would raise the q to ~ 1 at all radii if it is permitted to exist. This scenario confirms the earlier assertion that quasilinear effects determine constant V_L, thin-shell behavior.

c. n > 0 external kink

Although our results do not show a strong m = 1, n > 0 kink, preliminary simulations at higher Θ[16] and experimental results[17] indicate that these modes may be important. As described earlier, these modes are more unstable with deeper reversal and large r_w. In this section, we investigate the quasilinear behavior of the 1, 1 kink at R/a = 2.

For this case, we choose $\tau_S / \tau_R = 1/15$ and initial q and λ profiles as shown in Fig. 3.23. The relatively deep reversal ensures that the 1, 1 kink is unstable. Other parameters are the same as were used for the ULQ kink simulation. Artificial E_θ and E_z are also applied to prevent resistive diffusion of the chosen mean field.

The final q and λ profiles are shown in Fig. 3.23, where they are compared with the initial profiles. The n > 0 kinks clearly reduces $J_{||}$ (see

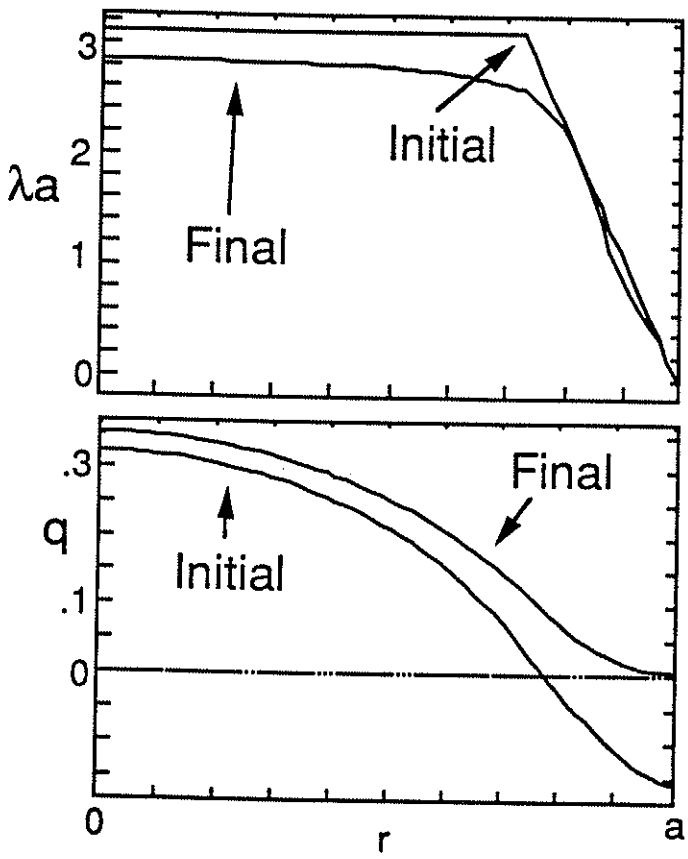

FIG. 3.23 Comparison of the initial and final q and λ profiles of the mean field for a quasilinear simulation; only the m = 1, n = 1 mode is present.

λ profile comparison), which removes reversal (see final q profile) and allows the kink to self stabilize. Thus, the presence of the $n > 0$ kinks can be expected to enhance the V_L if the total current is held constant. The anti-reversal effect is also expected to be quasilinearly destabilizing to the dynamo modes.

3.5. SUMMARY AND DISCUSSION

a. Preliminary comparison with experimental results

Experimental results on both the thin-shell and the distant wall problems have been reported recently. This section briefly summarizes the results of initial comparisons of theory and experiments. Qualitatively, our results reproduce many of the key features of the experiments; however, interesting disagreements are also seen.

For the distant wall cases (HBTX1B experiments[18]), we note the following agreements. The magnitiude of the V_L rise seen in the experiments (up to ~ 3 times the original level with) with varying boundary condition (insertion of limiters and tiles) can be accounted for in our model with vaccum region thickness between 0 and roughly 40% at $\Theta = 1.59$. Unfortunetly, we do not yet know the exact Θ values in experiments. If it is higher than 1.59, than the numerical results requires less than 40% vacuum width to triple theV_L. In addition, the F-Θ relationship is roughly unaltered as the V_L rises. This has important implication for the helicity and energy balance, which are described in Chap. 4 below. A more quantitative comparison is difficult since neither

experiments and simulations can determine the edge vacuum width accurately; the enhanced edge transport (expected, but not modeled) presumably has a large effect on the effective vacuum width in both the experiments and the simulations.

For the thin-shell cases (OHTE[19], HBTX1C[17] experiments), the experiments observed enhanced magnetic fluctuations, deeper reversal, and greatly enhanced V_L as in the simulations. In particular, large dynamo modes ($m = 1$, $na/R \sim 2$) are observed. Disagreements are found, however, in the presence of the $n > 0$ external kinks in experiments (discussed earlier), and in the temporal behavior. The experiments generally observe $m = 1$ modes growing at less than half the rates (in units of $1/\tau_s$) of our results. Moreover, the OHTE experiments displayed oscillatory type behavior; sometimes, the MHD modes grow, phase lock (slinky mode), appear to self-stabilize and disappear, and then grow again. This behavior is probably due to transport[19] or non-MHD effects[20].

b. Summary

In conclusion, the conducting wall is a key element in the nonlinear MHD evolution of the RFP. It is well-known that with a close-fitting conducting wall, the internally resonant $m = 1$ modes, through their $\mathbf{v} \times \mathbf{b}$ effect, drive current in the edge to sustain reversal; the effect flattens the $\lambda(=J/B)$ profile while increasing shear, which has a stabilizing effect on the modes. This fluctuation-induced electric field, along with nonlinear stabilization via mode coupling, is balanced by the applied electric field

which has the destabilizing effect of peaking λ. Removal of the wall disturbs this balance; the $m = 1$ modes grow, suppress the central current and thereby require an enhanced loop voltage to maintain the current. The increase in the $\mathbf{v} \times \mathbf{b}$ electric field, combined with the rising V_L, produces little increase in shear for self-stabilization of the $m = 1$ modes. Thus, $m = 1$ modes and V_L grow to a large amplitude. While direct nonlinear mode coupling is stabilizing, the principal destabilizing mechanism appears to be quasilinear mode coupling between dynamo modes (i.e., dynamo mode–mean field–dynamo mode interaction). If V_L is held constant, current falls as the plasma evolves toward a nonreversed state. Below $\Theta = 1.4$ (weakly reversed toroidal field), the global (thus strongly boundary condition dependent and difficult to self-stabilize) ULQ kinks continue to reduce the current density until q rises to ~ 1. The plasma evolves through a sequence of quasilinear ULQ kinks ($m = 1$, $n = -3$, to -2 to -1); each mode quasilinearly reduces and flattens the current, raises q, and self-stabilizes before another (lower $|n|$) mode takes over. These effects, to varying extent, occur with either a resistive or distant boundary. The anomalous loop voltage present in some RFP experiments with limiter insertion may result from such MHD effects. Many general features of thin-shell experiments can also be explained by the present model. Ironically, the conducting wall serves the useful purpose of preventing the dynamo modes from becoming too robust.

REFERENCES

[1]J. B. Taylor, Rev. Mod. Phys. **58**, 741 (1986).

[2]D. D. Schnack and J. Killen, J. Comput. Phys. **35**, 110 (1980).

[3]K. V. Roberts and D. E. Potter, in *Methods in Computational Physics*, Vol. 9, edited by B. Alder, S. Fernbach, and M. Rotenberg (Academic Press, New York, 1970), p. 340.

[4]T. Tajima, in *Frontiers in Physics*, Vol. 72, edited by D. Pines (Addison-Wesley, USA, 1989).

[5]See, for example: E. J. Caramana, and D. D. Schnack, Phys. Fluids **29**, 3023 (1986); A.Y. Aydemir, and D. C. Barnes, Phys. Rev. Lett. **52**, 930 (1984).

[6]D. D. Schnack, D. C. Barnes, Z. Mikic, D. S. Harned, and E. J. Caramana, J. Comput. Phys. **70**, 330 (1987).

[7]D. Gottlieb and S. A. Orszag, *Numerical Analysis of Spectral Methods*, (SIAM, Philadelphia, 1977).

[8]A. J. Robert, in *Proceedings of WMO/IUGG Symposium on Numerical Weather Prediction*, Tokyo, 1969.

[9]D. S. Harned and D. D. Schnack, J. Comp. Phys. **65**, 57 (1986).

[10]J. W. Eastwood and W. Arter, Phys. Fluids, **30**, 2774 (1987).

[11]E. J. Caramana, R. A. Nebel, and D. D. Schnack, Phys. Fluids, **26**, 1305 (1983).

[12]S. C. Prager and L. Turner, Phys. Fluids, **28**, 1155 (1985).

[13]J. A. Holmes, B. A. Carreras, P. H. Diamond, and V. E. Lynch, Phys. Fluids **31**, 1166 (1988).

[14]N. Asakura, et al., in *Proceedings of the 11th Int. Conference on Plasma Physics and Controlled Nuclear Fusion Research*, Kyoto, 1986 (IAEA, Vienna, 1987), Vol. 2, p. 433.

[15]K. Kusano, T. Sato, H. Yamada, Y. Murakami, Z. Yoshida, and N. Inoue, Nucl. Fusion, **28**, 89 (1988).

[16]D. D. Schnack, D. S. Harned, and S. Ortolani, Bull. Am. Phys. Soc. **33**, 2064 (1988).

[17]B. Alper, et al. in *Proceedings of the 12th Int. Conference on Plasma Physics and Controlled Nuclear Fusion Reasearch*, Nice, 1988 (to be published).

[18]B. Alper and H. Y. W. Tsui, in *Proceedings of the 14th European Conference on Controlled Fusion and Plasma Physics*, Madrid, 1987 (European Physical Society, Budapest, 1987), Vol. II, p. 434.

[19]T. Tamano, W. D. Bard, C. Chu, Y. Kondoh, R. J. La Haye, P. S. Lee, M. T. Saito, M. J. Schaffer, and P. L. Taylor, Phys. Rev. Lett. **59**, 1444 (1987).

[20]A. R. Jacobson and R. W. Moses, Phys. Rev. A **29**, 3335 (1984).

Chapter 4
DISCUSSION

4.1 HELICITY AND ENERGY BALANCE

Since the early work by Taylor[1], who minimized magnetic energy with a constant helicity constraint and predicted the RFP state, a class of theoretical MHD models has been developed which is based on helicity and energy conservation laws[1]. Underlying this apparent enthusiasm is the model's inherent simplicity. Proper understanding and utilization of these models, aside from the obvious benefit of simplicity, may lead to novel ideas for plasma stabilization, and sustainment (e.g., F-Θ pumping[2]).

The following sections discuss the helicity and energy balance properties of the numerical distant wall results (helicity is undefined without a conducting wall). We compare our evaluations with assumptions of helicity and energy balance properties used in other models of anomalous V_L[3]. The implications of our results as compared to the Taylor relaxation theory are also discussed. A helicity based model of nonideal boundary RFP behavior is beyond the scope of this thesis. Our goal is simply to point out some of the complications that need to be considered in such a model.

a. Helicity balance

The standard gauge invariant helicity is defined as[4]

$$K=\int_{r=0}^{r_w} \mathbf{A}_T \cdot \mathbf{B}_T d^3\mathbf{r} - \Phi_\theta^{r_w}\Phi_z^{r_w}, \tag{4.1}$$

where the second term is a product of the toroidal flux enclosed by the conducting wall and the poloidal flux linked by the toroidal flux. Near steady state, $\partial K/\partial t \sim 0$, we obtain the conservation relationship

$$V_L\Phi_z = \int \eta \mathbf{J} \cdot \mathbf{B}\, d^3\mathbf{r} + \int \eta \mathbf{j} \cdot \mathbf{b}\, d^3\mathbf{r} + \int_{ext} \mathbf{e} \cdot \mathbf{b}\, d^3\mathbf{r}, \tag{4.2}$$

where Φ_z is the toroidal flux in the plasma, the first two integrals extend over the plasma volume, and the last integral covers the volume external to the plasma. This relationship can be interpreted as the helicity injected into the plasma ($K_{inp} = V_L\Phi_z$) by external circuits balanced against the plasma dissipation ($\int \eta \mathbf{J} \cdot \mathbf{B}\, d^3\mathbf{r} + \int \eta \mathbf{j} \cdot \mathbf{b}\, d^3\mathbf{r}$), and dissipation from fluctuation electric fields external to the plasma ($\int_{ext} \mathbf{e} \cdot \mathbf{b}\, d^3\mathbf{r}$). Moreover, the component of the external electric field which has $\nabla \times \mathbf{e} \neq 0$ does not dissipate helicity (see Appendix); hence, the $\int_{ext} \mathbf{e} \cdot \mathbf{b}\, d^3\mathbf{r}$ term can be converted to a surface integral, and interpreted as surface fluctuation losses (i.e., $\int_{ext} \mathbf{e} \cdot \mathbf{b}\, d^3\mathbf{r} = \int_{ext} \nabla\chi \cdot \mathbf{b}\, d^3\mathbf{r} = -\int_S \chi \mathbf{b} \cdot d\mathbf{s}$, and the helicity loss is entirely electrostatic).

From the Ohm's law as applied to the parallel mean field in near steady state, we obtain

$$V_L\Phi_z = \int \eta \mathbf{J} \cdot \mathbf{B}\, d^3\mathbf{r} + \int E_f B\, d^3\mathbf{r}. \tag{4.3}$$

This relationship can also be obtained by balancing the helicity of the

mean fields, K_m, where K_m is defined as in Eq. 4.1 except that only the mean components **A** and **B** are used[5]. Comparing Eqs. 4.3 and 4.2, we further interpret the terms thus: the injected helicity first goes into K_m; the mean field dissipates an amount equal to $\int \eta \mathbf{J} \cdot \mathbf{B}\, d^3\mathbf{r}$, while the fluctuation extract the remainder (an amount equal to $\int E_f\, B\, d^3\mathbf{r}$); the amount extracted by the fluctuations is both dissipated (by $\eta \mathbf{j} \cdot \mathbf{b}$) in the plasma, as well as lost through the surface ($\int_{ext} \mathbf{e} \cdot \mathbf{b}\, d^3\mathbf{r}$).

The terms appearing in Eqs. 4.2 and 4.3 are numerically evaluated, and listed in Table 4.1; the parameters are $\Theta \approx 1.59$, $r_w/a = 1$, 1.15, and 1.455, and $\Theta \approx 1.73$, $r_w/a = 1$, and 1.05 for the cases shown. The fluctuation surface potential (for the $\int_{ext} \mathbf{e} \cdot \mathbf{b}\, d^3\mathbf{r}$ term) is evaluated by using the condition of continuity of electric fields parallel to the surface, then subtracting the $\nabla \times \mathbf{e} \neq 0$ component. Not surprisingly, K and K_m are roughly conserved as they must be. Equations 4.2 and 4.3 cannot be satisfied exactly due to the slab approximations used for the thin-shell boundary condition (affecting the $\int_{ext} \mathbf{e} \cdot \mathbf{b}\, d^3\mathbf{r}$ term), and since the plasma is not in a perfect steady state.

Most notably, TABLE 4.1 shows that helicity dissipation in the plasma (the $\int \eta \mathbf{J} \cdot \mathbf{B}\, d^3\mathbf{r}$ and $\int \eta \mathbf{j} \cdot \mathbf{b}\, d^3\mathbf{r}$ terms) increases negligibly with enhanced fluctuations. The increased helicity input to K_m is extracted by an enhanced $\int E_f\, B\, d^3\mathbf{r}$ (consistent with Chap. 2 results) and lost through the surface. The same conservation properties can be applied to experiments. Since the experimental mean field profiles remain about the same (F-Θ relationship ~ same) with rising V_L, the experimental $\int E_f\, B\, d^3\mathbf{r}$

TABLE 4.1. Evaluation of the terms appearing in the helicity balance equations (Eqs. 4.2 and 4.3) for different distant wall cases.

Θ, %Vacuum	$V_L\Phi_z$	$\int \eta \mathbf{J}\cdot\mathbf{B}\, d^3\mathbf{r}$	$\int E_f B\, d^3\mathbf{r}$	$\int \eta \mathbf{j}\cdot\mathbf{b}\, d^3\mathbf{r}$	$\int_{ext} \mathbf{e}\cdot\mathbf{b}\, d^3\mathbf{r}$
1.592, 0%	24.5	24.9	0.6	0.5	0
1.592, 15%	32.9	25.1	7.6	1.4	11.3
1.592, 45%	43.6	25.5	17.3	2.6	16.9
1.73, 0%	32.7	33.7	0.7	0.8	0
1.73, 5%	48.2	37	9.7	2.7	12

TABLE 4.1. Evaluation of the terms appearing in the energy balance equations (Eqs. 4.4 and 4.5) for different distant wall cases.

Θ, %Vacuum	$V_L I$	$\int \eta J^2\, d^3\mathbf{r}$	$\int -S\langle \mathbf{v}\times\mathbf{b}\rangle_{\theta,z}\cdot\mathbf{J}\, d^3\mathbf{r}$	$\int \eta j^2\, d^3\mathbf{r}$
1.592, 0%	78.1	72.9	8.2	5.9
1.592, 15%	104.8	70.6	32.3	20.3
1.592, 45%	138.7	68.2	68.1	31.3
1.73, 0%	113.3	100.3	16	11.4
1.73, 5%	166.8	103.4	58.9	32.5

(and hence E_f) must also be enhanced (assuming the Ohm's law of Eq. 3.1 is reasonably complete).

Given the apparent importance of the surface term, it becomes necessary to have a physical interpretation of its presence. In our model, this term comes from the capacitive charge separation across the insulating layer on the inside surface of the thin-shell. The charge polarization is induced by fluctuating electric fields at the surface. The electric field produced by the charges self consistently keeps $j_r = 0$ on the plasma surface, while maintaining continuity of e_θ and e_z. In most instances, continuity of j_r implies a discontinuity in e_r (i.e., surface charge) whenever materials of different current carrying properties are in contact. The entire picture can be interpreted as follows. Since the presence of the vacuum region causes instability, and current flow must be interrupted somewhere when perturbed magnetic fields enter a vacuum region (implying surface helicity loss), vacuum induced instability implies surface helicity leakage and vice versa. Not surprisingly then, E_f extracts just the amount of helicity to supply the surface loss. In this vein, it may be instructive to think of E_f as a helicity transport mechanism as suggested in Ref. 3.

Whether a different boundary condition (e.g., $j_r \neq 0$) would affect our results also becomes a valid concern, and should be investigated. For now, we argue heuristically that our results should remain the same. First of all, stability should be unaffected since the stabilizing effect of the shell depends on its magnetic field shielding properties (the thin shell boundary

condition, Eq. 2.3, is still valid). Moreover, since $j_r = 0$ on the outer surface of the thin-shell (regardless of the inner surface boundary condition), currents along field lines must still be interrupted somehow when perturbed magnetic fields penetrate the surface. The potential drop, which used to be across the insulating layer, can simply be redistributed with the same overall helicity dissipation (in this case, some charges would appear on the outer surface of the thin-shell). Thus, with stability unaffected and the channel of surface helicity outflow open (one should imply the other anyway), the overall picture cannot change.

b. Magnetic energy balance

Conserving the total and mean field magnetic energy near steady state, we obtain two equations similar to 4.2 and 4.3:

$$V_L I = \int \eta J^2 \, d^3r + \int \eta j^2 \, d^3r + D_V, \tag{4.4}$$

and

$$V_L I = \int \eta J^2 \, d^3r + \int -S\langle \mathbf{v} \times \mathbf{b} \rangle_{\theta,z} \cdot \mathbf{J} \, d^3r, \tag{4.5}$$

where I is the nondimensional current [$=2\pi B_\theta(r=a)$]. By analogy to the helicity balance equations, the fluctuations extract magnetic energy (in amount $= \int -S\langle \mathbf{v} \times \mathbf{b} \rangle_{\theta,z} \cdot \mathbf{J} \, d^3r$) from the mean field; this energy is converted to kinetic energy (the D_V term), and feeds ohmic dissipation (ηj^2). The external circuit supplies magnetic energy ($W_{inp}=V_L I$) to balance the mean field loses.

The various terms in Eqs. 4.4 and 4.5 are evaluated for the distant wall cases and shown in TABLE. 4.2. The most interesting observation is

that roughly half of the increased W_{inp} from the enhanced V_L is converted to kinetic energy, consistent with the equilibration of kinetic and magnetic energy for rising fluctuations as seen in Chap. 2 (Fig. 3.9). This energy is presumably viscously dissipated since the total energy must be conserved, although the viscous loss is currently not directly evaluated. Thus, viscosity is seen to play an important role in energy conservation (even though it was included primarily for numerical reasons). The anomalously high ion temperature seen in experiments may arise from such viscous heating. This topic is being investigated currently. The key issues addressed are: the roles played by small scale versus large scale fluctuations; the scaling of dissipation with ν; the effect of modifications to the viscous term [e.g., addition of $a\nabla(\nabla\cdot\mathbf{v})$ term]. The findings will be presented elsewhere.

c. Taylor relaxation process

In this section, we discuss the implications of the above results for the Taylor minimum energy state (described by $\nabla \times \mathbf{B} = \lambda\mathbf{B}$, where λ is a spatial constant, and is specified for a given Θ). In Taylor's theory, a plasma isolated from external influences by a conducting wall is presumed to seek a minimum energy state while preserving the total magnetic helicity. This occurs since resistive instabilities dissipate energy faster than helicity. References 6, and 7 should be consulted for possible dynamical explanations beyond simple scale length arguments [$\eta j^2 \sim \eta\delta^{-2}b^2 \gg \eta j\cdot b \sim \eta\delta^{-1}b^2$ for small scale (scale length $\sim \delta$) fluctuations]. Quantitatively, the

numerical results demonstrate this behavior; in TABLEs 4.1 and 4.2, $\eta j^2/\eta j\cdot \mathbf{b}$ is at least 10 in all cases (even greater if D_V included), while the typical ratio of total magnetic energy to helicity (ignoring the $\Phi_\theta\Phi_z$ term, which implies the absence of gaps in the conducting wall) ratio is ~ Θ (not shown). Thus, if the plasma is initially unstable, the inevitable fast time scale relaxation towards a lower energy state due to instabilities can be understood by Taylor's theory.

Experimental RFPs, however, are affected by external circuits through injection of W_{inp} and K_{inp}. For a given Θ, $W_{inp}/K_{inp} = 2\Theta$. In steady state, these inputs must be dissipated at the rates injected (Eqs. 4.2 and 4.4), i.e., the resistive dissipation of helicity and energy of the mean field (slow time scale diffusion) cannot be ignored. Hence, it is reasonable to expect that a more complete minimum energy theory would include additional constraints based on Eqs. 4.2 and 4.4.

We first consider the steady state close-fitting conducting wall case (surface helicity losses = 0). Since $W_{inp}/K_{inp} = 2\Theta$, and $(\int \eta j^2\, d^3r + D_V)$ / $\int \eta j\cdot \mathbf{b}\, d^3r \gg 2\Theta$, the mean field energy to helicity dissipation ratio $(\int \eta J^2\, d^3r$ / $\int \eta J\cdot \mathbf{B}\, d^3r)$ must be < 2Θ (as shown by all cases listed in TABs. 4.1 and 4.2). Not coincidentally, the Taylor state has $\int \eta J^2\, d^3r / \int \eta J\cdot \mathbf{B}\, d^3r = 2\Theta$, as with the unstable case where all fluctuations are artificially suppressed (Secs. 3.3a and 3.4a). Neither state can be the mean field of a dyanamo-sustained steady state. Thus, Taylor's theory may require an additional constraint on $\int \eta J^2\, d^3r / \int \eta J\cdot \mathbf{B}\, d^3r$. It may be an interesting exercise to find a mean field state that minimizes $\int \eta J^2\, d^3r$ with respect to

$\int \eta \mathbf{J} \cdot \mathbf{B}\, d^3r$; the solution should set an upper bound on the fraction of W_{inp} that can drive fluctuations in steady state. This ultimately constrains the amount of work that fluctuations can do on the mean field for self-stabilization, and presumably, how stable the mean field profile can be.

Furthermore, to more precisely determine how injected energies are divided between fluctuations and mean field dissipations, more detailed stability considerations may be required. For example, for sustainment the RFP must exist near some nonlinear marginal stability boundary for the dominant dynamo modes; however, it can be very stable for the other modes. Periodicity constraints, viscosity, and resistivity profiles can also preferentially weight the effect of different modes. To this end, the idea of Bhattacharjee et. al.[8] seems most promising: an additional constraint was introduced which depends on the mode number of an assumed dominant instability.

Deviations from the ideal boundary condition adds additional complications. Basically, the additional problem boils down to determining the ratio $\int -S\langle \mathbf{v} \times \mathbf{b} \rangle_{\theta,z} \cdot \mathbf{J}\, d^3r / \int_{ext} \mathbf{e} \cdot \mathbf{b}\, d^3r$ for a given vacuum width. Physically, this ratio determines the efficiency (in terms of K_{inp}) of nonideal boundary instabilities to self-stabilize. If this ratio is large, the instabilities, by the constraint of $(\int \eta J^2\, d^3r + \int -S\langle \mathbf{v} \times \mathbf{b} \rangle_{\theta,z} \cdot \mathbf{J}\, d^3r) / (\int \eta \mathbf{J} \cdot \mathbf{B}\, d^3r + \int_{ext} \mathbf{e} \cdot \mathbf{b}\, d^3r) = 2\Theta$ ($\eta \mathbf{j} \cdot \mathbf{b}$ is ignored), easily modifies the mean field (presumably towards a more stable state) with small K_{inp} enhancement. If $\int -S\langle \mathbf{v} \times \mathbf{b} \rangle_{\theta,z} \cdot \mathbf{J}\, d^3r / \int_{ext} \mathbf{e} \cdot \mathbf{b}\, d^3r = 2\Theta$, the mean field

must also have $\int \eta J^2 \, d^3r / \int \eta J \cdot B \, d^3r = 2\Theta$. This implies, from earlier discussions, an unstable mean field state (it's unlikely to be the Taylor state), and V_L would rise without bound.

d. Comments on the work of Tsui

Using essentially Eq. 4.2, Tsui[3] calculated the V_L rise for an RFP plasma in which a graphite tile was inserted at the edge. Assuming no increase in $\int \eta J \cdot B \, d^3r$ and $\int \eta j \cdot b \, d^3r$, the rise in V_L was determined by calculating the surface helicity leakage. As with our theory, he suggested that this leakage is due to obstruction of current flow through surfaces which magnetic flux can penetrate. Unlike our MHD based theory, he calculated the surface helicity loss from kinetic sheath effects. A relation between the surface potential and electron temperature was derived. His theory, however, did not include stability considerations, and hence could not account for an E_f which must become more positive (Eq. 4.3). If the sheath effect can be linked to the creation of a vacuum region, then the two theories can be combined.

e. Comments on the Kinetic Dynamo Theory

Jacobson and Moses[9] have proposed a theory in which the dynamo effect is caused by long collisional mean-free path electrons traveling along stochastic field lines (the Kinetic Dynamo Theory, KDT). With this theory, E_f is not required (rather, only low level fluctuations which cause field line stochasticity are necessary). Recently, the KDT has been extended by

Moses et. al.[10] to explain the dependence of V_L on boundary conditions. Basically, if fast streaming electrons carried significant energy along field lines to the wall or limiters, increased W_{inp} is required to balance the loss. A global helicity balance is also possible (Eq. 4.2) if the electrons causes surface potentials to be built up.

Upon examination of Eq. 4.3, we find possible inconsistencies. By definition, the collisionless electrons carry current without electric field. Thus, Eq. 4.3 remains valid, as long as the $\eta\mathbf{J}$ term is understood to include only MHD currents, while $\mathbf{B}$ is due to both MHD and KDT currents. Without large E_f, Eq. 4.3 implies that $\int \eta\mathbf{J} \cdot \mathbf{B}\, d^3\mathbf{r}$ at least doubles when V_L more than doubles with the insertion of limiters. Since the current profile due to a sum of MHD and KDT currents cannot be significantly changed (it would show up in the F-Θ relation), the collisionless electrons must then carry significant negative parallel current (on the order of the total toroidal current). This is an unlikely scenario for the steady state experiments (for which Eq. 4.3 applies) with inserted limiters. The KDT however, provides a plausible explanation for the oscillatory behavior (not a steady state, hence Eq. 4.3 does not apply) of the OHTE thin shell experiment. It may be that the KDT effect becomes significant when MHD fluctuations are large and phase–locked (the slinky mode), thus enhancing field line stochasticity[11]. Significant positive parallel current in the outer region due to the collisionless current can then stabilize the dynamo modes.

4.2 COMMENTS ON ANALYTICAL CALCULATIONS OF E_f

To date, analytical calculations of E_f using the MHD equations have usually ignored nonlinear mode coupling effects[12,13]. In principle, most of the important quasilinear effects can be included. In practice, however, only the shape of E_f due to a single mode, with assumed mode type (e.g., tearing mode), is derived from linear theory. The entire E_f profile is then assumed to be composed of contributions from a bath (across the minor radius) of such modes, each with an assumed saturation amplitude. The determination of saturation amplitudes (as a function of radius) can be guided by experiments, by 3D numerical simulation, or by physical arguments. The derived E_f usually flattens the λ profile, and successfully produces the dynamo effect. These calculations contribute to the understanding of the dynamo effect from a dynamical point of view. Thus, with suitable extension, they may help in understanding the quasilinear destabilization mechanism underlying the nonideal boundary effects. We do not as yet see an easy way to do the necessary extension, but additional work in this direction is still being considered.

4.3 SCALING TO EXPERIMENTAL PARAMETER REGIMES

From the MHD equations used in the numerical calculations (Eqs. 3.1 and 3.2), the only two parameters to be scaled are S and ν. In general, the numerical results are scaled by extrapolation from a few sample runs with different S and ν. This work is currently being performed. Here, we make simple predictions based on the MHD equations, and physical arguments.

Assuming $\mathbf{V}_T \sim 1/S$ and that $\mathbf{B}_T$ does not scale with S in the $S \rightarrow \infty$ limit, if $\mathbf{V}_T$ and $\mathbf{B}_T$ are solutions of the steady state MHD equations at one S value, then they are also solutions at another S value. This is the scale invariant property of the steady state MHD equations (see Ref. 14); it implies that the nondimensional electric fields (e.g., V_L) should be independent of S as $S \rightarrow \infty$. In addition, the viscous and nonlinear advection terms are unimportant in this large S limit.

If S is finite, the simple scaling laws described above do not hold if the viscous and nonlinear advection terms cannot be ignored. This occurs when **v** is relatively large, which is expected since viscous dissipation of energy can become significant as described earlier. The relative effect of viscosity, usually stabilizing, increases with decreasing S. Thus, for the high Θ cases, the large vacuum region distant wall cases, or in the latter stages of thin shell evolution, we expect the V_L to increase with S. This behavior has already been seen and reported elsewhere[15].

4.4 FUTURE WORK

In this section, we discuss some of the planned, initiated, or possible research topics to follow the work presented in this thesis. Roughly, the topics can be grouped under a few general areas: better understanding of present results, parameter testing, stabilization, and additional physics.

Towards better understanding of the present results, additional code diagnostics are being implemented. These diagnostics would track the flow of energy between modes, determine the relative importance of small

scale versus large scale fluctuation dissipation, and determine the nonlinear terms that are important for the quasilinear effects. In addition, analytical studies based on helicity balance and maybe quasilinear approximations of the MHD equations should be pursued.

Parameter testing is necessary to determine the extent of applicability of the current results, and in many cases, allows us to scale the results to realistic conditions. Clearly, parameter testing will also help to better understand our present results. To these ends, it would be appropriate to test the effects of increased mode resolution, and varying S, ν, τ_s, Θ, R/a. Initial results from runs with twice the number of toroidal and poloidal modes showed negligible changes with small vacuum regions (up to 30%). Since nonlinear stabilization becomes important as fluctuations increase, however, additional small scale modes are expected to be stabilizing with larger vacuum regions and during latter stages of thin-shell evolution. The necessity for testing the effects of varying the other parameters (S, ν, τ_s, etc.) are obvious, and will not be further discussed.

The same MHD computational tools developed to study the effect of nonideal boundary can also examine the possibility of alternative stabilization schemes. Some of the ideas to be considered are feedback stabilization through electrical means at the boundary, current profile modification, and means of controlling helicity and energy flow at the boundary. Among these ideas, feedback stabilization is the simplest and is already being planned for an experiment[16]. Current profile modification may work with weak reversal (which weakens external kink and $m = 0$

modes), and theoretically, can stabilize the dynamo modes for all boundary conditions. Thus, this method can conceivably improve the transport characteristics of the RFP beyond the ideal wall case. Although, admittedly, the method would be complicated. Controlling the edge helicity flow can be done through electrostatic feedback. This idea is only at the conceptual stage and could be considered sometime in the future.

The MHD computations performed have adequately depicted key physical mechanisms that influence the plasma as the boundary is varied. To obtain a comprehensive picture, even within MHD, will however require inclusion of other important effects. The ones often mentioned are equilibrium flow, pressure, the Hall effect, and transport. Some of these effects are already being examined by other researchers. For example, enhanced transport associated with nonideal boundary fluctuations was shown to limit the maximum beta attainable[17]. Flow was found to be ineffective against kink modes which can lock to the wall[18]. Against resistive modes, however, flow can slow down the mode growth (a mode cannot lock to both the rotating plasma and the stationary shell). Since both types of modes might be important, this issue is unresolved and need to be examined further.

REFERENCES

[1]J. B. Taylor, Rev. Mod. Phys. **58**, 741 (1986), and references cited therein.

[2]T. H. Jensen and M. S. Chu, Phys. Fluids **27**, 2881 (1984).

[3]H. Y. W. Tsui, in *Proceedings of the 14th European Conference on Controlled Fusion and Plasma Physics*, Madrid, 1987 (European Physical Society, Budapest, 1987).

[4]M. Bevir and J. Gray, in *Proceedings of the Reversed Field Pinch Theory Workshop*, Los Alamos, 1980, edited by H. R. Lewis and R. A. Gerwin (Los Alamos National Laboratory, Los Alamos, New Mexico), Session III, Paper A-3.

[5]A. Bhattacharjee and E. Hameiri, Phys. Rev. Lett. **57**, 206 (1986)

[6]E. Hameiri and J. H. Hammer, Phys. Fluids **25**, 1855 (1982)

[7]A. Bhattacharjee, R. L. Dewar, and D. A. Monticello, Phys. Rev. Lett. Phys. **45**, 347 (1980).

[8]A. Bhattacharjee, and R. L. Dewar, Phys. Fluids **25**, 887 (1982).

[9]A. R. Jacobson and R. W. Moses, Phys. Rev. A **29**, 3335 (1984).

[10]R. W. Moses, K. F. Schoenberg, and D. A. Baker, to be published in Phys. Fluids.

[11]T. Tamano, W. D. Bard, C. Chu, Y. Kondoh, R. J. La Haye, P. S. Lee, M. T. Saito, M. J. Schaffer, and P. L. Taylor, Phys. Rev. Lett. **59**, 1444 (1987).

[12]E. Hameiri and A. Bhattacharjee, Phys. Fluids **30**, 1743, (1987).

[13]H. R. Strauss, Phys. Fluids **29**, 3668 (1986).

[14]Z. G. An, P. H. Diamond, T. S. Hahm, G. S. Lee, B. D. Scott, B. A. Carreras, L. Garcia, J. A. Holmes, V. E. Lynch, in *Proceedings of the 11th International Conference on Plasma Physics and Controlled Nuclear Fusion Research*, Kyoto, 1986 (IAEA, Vienna, 1987), Vol. 2, p. 663.

[15]D. D. Schnack, D. S. Harned, and S. Ortolani, Bull. Am. Phys. Soc. **33**, 2064 (1988).

[16]C. M. Bishop, Bull. Am. Phys. Soc. **33**, 2064 (1988).

[17]H. R. Strauss, Bull. Am. Phys. Soc. **33**, 2064 (1988).

[18]C. G. Gimblett, Nucl. Fusion **26**, 617 (1986).

Chapter 5
CONCLUSION

We have studied both the thin shell and the distant wall problems linearly and nonlinearly. Similar physics dominates each case (the resistive shell affects only the time evolution, not the final state).

Linearly, five type of modes of potential import are identified: the dynamo modes, the ULQ tokamak kinks, the $n > 0$ external kinks, the $-B_Z$ tearing modes, and the $m = 0$ tearing modes. Of these linear modes, the dynamo modes are supposed to be least sensitive, while the kinks are the most sensitive to boundary condition variations.

Nonlinearly, without a close-fitting conducting wall, the plasma generally evolves to a state with enhanced fluctuations, primarily composed of the dynamo modes. The dynamo modes, due to quasilinear mode interaction, are more strongly affected by the boundary than the linear theory implies. The fluctuations increase as the radius of the conducting wall is increased. The increased amplitude of these modes (which ordinarily produce the dynamo effect) yields an increase in the induced electric field, given by $\mathbf{v} \times \mathbf{b}$. The electric field is mainly in a direction to oppose the current parallel to the magnetic field; hence, an increase in the applied loop voltage, V_L, is necessary to maintain the toroidal current constant. If the loop voltage is held constant, the current decreases as the plasma (through a sequence of ULQ kinks) evolves toward a nonreversed tokamak-like state. The nonlinear results indicate that the

dynamo modes are probably the principal cause of the anomalous loop voltage seen in recent experiments with limiter insertion (HBTX-1B). Some qualitative features of our thin shell results have recently been seen in experiments (e.g., large dynamo mode growth, V_L rise, deeper reversal). The implication is that it will be necessary to find means to aid the thin shell in stabilizing the various modes.

In the discussions of helicity balance, we showed that $\int E_f B \, d^3r$ in the plasma increases from zero as the vacuum region increases in thickness. This represents an enhanced helicity transport to the boundary, where it is electrostatically dissipated in the surrounding insulating layer. Virtually all of the enhanced injection of helicity due to the enhanced V_L is lost in this manner (i.e., we see negligible change in the helicity dissipated by the plasma). The mean field helicity dissipation is always significant, however, and should be considered in all steady state models of the RFP based on the helicity balance (which precludes the Taylor state). With these and other considerations, we think that relatively detailed stability considerations are necessary, especially in the nonideal boundary cases, to understand the RFP state. Hence, a realistic model of the RFP state is unlikely to be as simple as the Taylor model.

No real surprises are found in the energy balance properties: we find with nonideal boundary conditions that enhanced fluctuations enhance energy dissipation. Notably, from energy balance, we inferr that half of the enhanced Poynting flux input from the enhanced V_L are viscously dissipated.

The nondimensional V_L for the various quasi-steady state nonideal boundary cases should, from scale invariant properties of the force-free MHD equations, scale up with S, if it scales at all. Any scaling should occur when viscous dissipation is significant.

Appendix
THE THIN SHELL BOUNDARY CONDITION

A.1 INTRODUCTION

In this appendix, we derive the boundary conditions used in the thesis. There are two linearly independent thin shell boundary conditions: one is for b_r; the other is for j_r. The boundary condition for b_r has been derived and used by other researchers (Refs. 1–7). The purpose here is to clarify the derivations, and the assumptions used therein.

If the evolution of the applied magnetic perturbation on one side of the thin shell is known, the penetration rate of this magnetic field through the shell can be easily derived by the Laplace transform technique. In reality, the magnetic field produced by the induced eddy currents in the shell affects the electrical system (e.g., a plasma) which originally excited the eddy currents. Thus, the response of the source of the perturbation must be included in the calculation. This is not possible when the perturbation is caused by a complicated system such as an MHD modeled plasma; the Laplace transform of its temporal dependence do not exist.

Nevertheless, Laplace transform can still be used to understand the response characteristics of the shell, which allows use to derive the simplified thin shell boundary condition. Physically, the electric and magnetic responses of the shell is determined by the decay characteristics of the eddy currents excited by the applied magnetic perturbation. The eddy currents are a linear superposition of basis eigenstates, each with a

characteristic decay rate. The thin shell approximation amounts to keeping only the lowest order eigenstate solution, i.e., the one with the slowest decay rate. The higher order solutions are assumed to have decayed away in the time scale of interest. A jump condition on b_r, and a boundary condition on j_r are derived based on the current profile of the lowest order solution. The eigenstates and their characteristic decay rates are derived with the Laplace transform technique.

A.2 DERIVATION OF EIGENSTATES

We consider the slab geometry (as shown below) first.

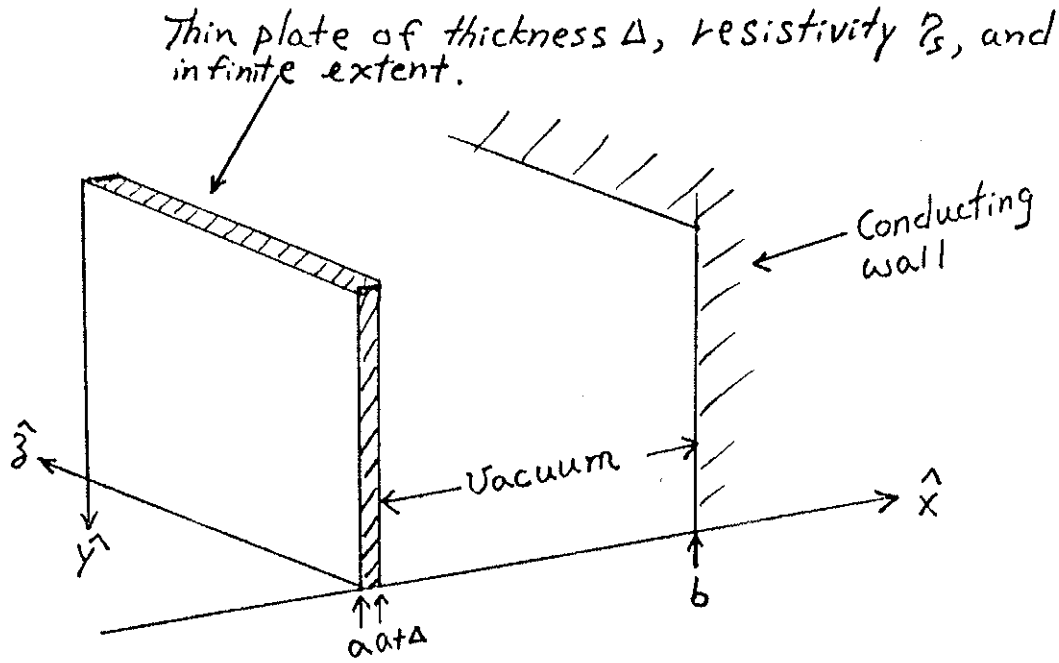

FIG. A.1

To find the magnetic field solutions, we solve a diffusion equation in the slab, and the standard Laplacian in the vacuum region. The diffusion equation is just

$$\eta_s \nabla^2 b = \partial b/\partial t, \tag{A.1}$$

which is derived from the Ohm's law ($\mathbf{e} = \eta_s \mathbf{j}$), and the dimensionless (see Chap. 3) Faraday's and Ampere's law ($\nabla \times \mathbf{e} = -\partial \mathbf{b}/\partial t$, and $\nabla \times \mathbf{e} = \mathbf{j}$). The boundary conditions are continuity of e_z, e_y, and b at the two interfaces at $x = a+\Delta$ and $x = a$. An assumed magnetic perturbation $[b_a(t)]$ is applied at $x = a$. We Fourier analyze in the z and y directions, and Laplace transform in time [i.e., $L(\partial b/\partial t) = p\hat{b}(p)$]. For the rest of the Appendix, $\hat{b}(p)$, $\hat{e}(p)$, and $\hat{j}(p)$ denote the magnetic field, electric field, and current density of a single Fourier harmonic in Laplace space. The eigenstates and characteristic decay rates are found by examining the magnetic field solution to Eq. A.1 in Laplace space. More specifically, the magnetic field solution in Laplace space can be generally written as

$$\hat{\mathbf{b}}(x,p) = \frac{F[\underline{U}(x,p),\ \hat{b}_a(p)]}{D(p)}$$

where $\underline{U}(x,p)$ and $D(p)$ are determined from the boundary conditions. By taking the inverse Laplace transform, one generally obtains a set of steady state and a set of transient solutions. These can be written as

$$\mathbf{b}(x,t) = \sum_{p_s} \frac{F[\underline{U}(x,p_s),\ \text{residue}\,\hat{b}_a(p_s)]}{D(p_s)} e^{p_s t} + \sum_{p_t} \frac{F[\underline{U}(x,p_t),\ \hat{b}_a(p_t)]}{\left(\frac{\partial D(p)}{\partial p}\right)\Big|_{p=p_t}} e^{p_t t}$$

where the p_t's locate the zeros of D(p), and the P_s's locate the poles of $\hat{b}_a(p)$. The characteristic decay rates of the eigenstates are equal to the $-P_t$'s. The Laplace space equivalent of Eq. A.1 is just

$$\nabla^2\hat{b}(p) = -\propto^2\hat{b}(p), \tag{A.2}$$

where $-\propto^2 = p/\eta_s$. For divergence-free vector fields, there are two sets of linearly independent solutions[8]–thereafter labeled R and Q. The R field satisfy the relationship

$$\mathbf{R} = \nabla\beta \times \hat{x} \tag{A.3}$$

where $\hat{x}$ is the unit vector in the x direction. The Q field satisfy

$$\mathbf{Q} = \propto\gamma\hat{x} + \propto^{-1}\nabla(\partial\gamma/\partial x). \tag{A.4}$$

The β and γ are scalar fields which are solutions of the Poisson equation, i.e.,

$$\nabla^2(\beta,\gamma) + \propto^2(\beta,\gamma) = 0, \tag{A.5}$$

where $\propto^2 = (k_x^2+k_y^2+k_z^2)$. The k_x, k_y, and k_z are mode numbers in the x, y, and z directions respectively. The vacuum solution for the region between x = a and x = a+Δ is just

$$\hat{b}(p,x) = \nabla\psi_{vac}(x), \tag{A.6}$$

where ψ_{vac} is a solution of the Laplacian. More importantly, we get

$$\hat{b}_x(a+\Delta,p) = -E(a+\Delta,b)\psi_{vac}(a+\Delta), \tag{A.7a}$$

$$\hat{b}_y(a+\Delta,p) = ik_y\psi_{vac}(a+\Delta), \tag{A.7b}$$

and

$$\hat{b}_z(a+\Delta,p) = ik_z\psi_{vac}(a+\Delta), \tag{A.7c}$$

where

$$E(a+\Delta,b) = (k_y^2+k_3^2)^{\frac{1}{2}} \left[\frac{e^{2(k_y^2+k_3^2)^{\frac{1}{2}}b} + e^{2(k_y^2+k_3^2)^{\frac{1}{2}}(a+\Delta)}}{e^{2(k_y^2+k_3^2)^{\frac{1}{2}}b} - e^{2(k_y^2+k_3^2)^{\frac{1}{2}}(a+\Delta)}} \right] \qquad (A.8)$$

The $\psi_{vac}(x)$ solution is known within a multiplicative constant at this point.

From the structure of the Q and the R fields, we find that the Q field determines the b_X (equivalent to b_r in cylindrical geometry) boundary condition to be derived, while the R field determines the j_X boundary condition. This is because the Q field has $j\hat{}_X = 0$ and the R field has $b\hat{}_X = 0$. Hence, the diffusion of magnetic field into the vacuum region is determined by the Q field only. Since the two fields are linearly independent, the R field can be force to vanish (e.g., by inserting an additional insulating layer on the x = a surface of the slab) without affecting the Q field.

We solve for the p_t's from the Q field solutions first. By continuity of $b\hat{}(x,p)$ at $x = a+\Delta$, the components of the $b\hat{}(x,p)$ solution in the slab are just

$$b\hat{}_r(x,p) = \left(\alpha - \frac{k_x^2}{\alpha}\right)\left(C_1 \sin k_x x + C_2 \cos k_x x\right) \qquad (A.9a)$$

$$b\hat{}_y(x,p) = \frac{i k_y k_x}{\alpha}\left(C_1 \cos k_x x + C_2 \sin k_x x\right) \qquad (A.9b)$$

and

$$b\hat{}_z(x,p) = \frac{i k_3 k_x}{\alpha}\left(C_1 \cos k_x x - C_2 \sin k_x x\right) \qquad (A.9c)$$

where the C_1 and C_2 coefficients are related by

$$C_2 = \frac{C_1 \left(\sin k_x\Delta + \frac{k_x E}{(k_y^2+k_3^2)} \cos k_x\Delta\right)}{\frac{k_x E}{(k_y^2+k_3^2)} \sin k_x\Delta - \cos k_x\Delta} \qquad \text{(A.10)}$$

From Eq. A.10, the set of p_t's are found from the k_x roots of the equations

$$\frac{k_x E}{(k_x^2+k_3^2)} \sin k_x\Delta - \cos k_x\Delta = 0 \qquad \text{(A.11)}$$

and

$$\sin k_x\Delta + \frac{k_x E}{(k_x^2+k_3^2)} \cos k_x\Delta = 0 \qquad \text{(A.12)}$$

The solutions can be found graphically as shown below for Eq. A.11.

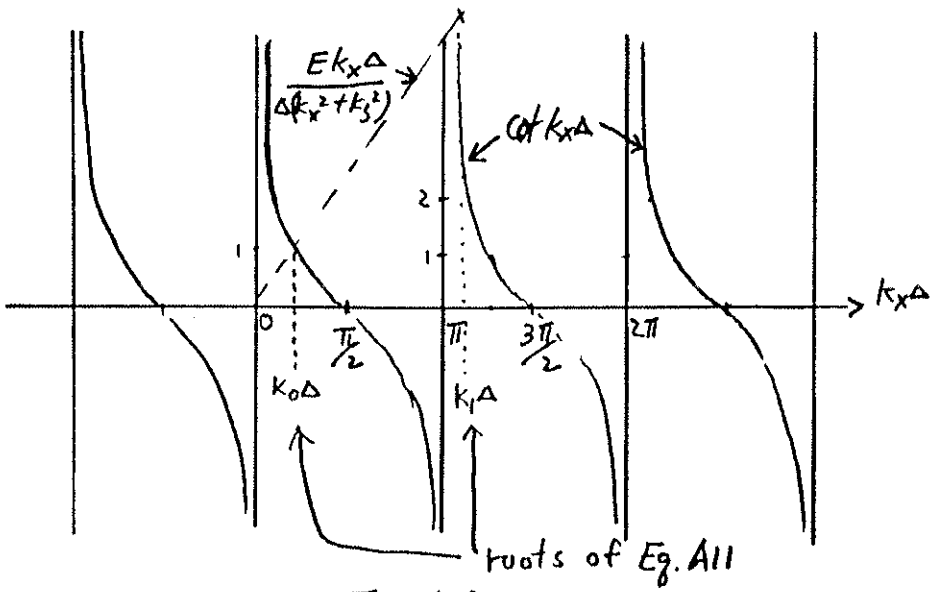

Fig A.2

For a thin shell $\Delta \ll (k_y^2 + k_z^2)^{-1/2}$, and since E has a minimum value of $(k_y^2 + k_z^2)^{1/2}$ as b approaches infinity, the solutions for k_i's are (excluding k_o) $k_i^2 \approx (i\pi/\Delta)^2$ for i = 1, 2, 3, etc. This corresponds to transient decay rates for the corresponding eigenstates of

$$-p_{t,i} = (k_i^2 + k_y^2 + k_z^2)\eta_s \approx \eta_s(i\pi/\Delta)^2 \text{ for } i = 1, 2, 3... \quad (A.13)$$

For small $k_o\Delta$ [assuming $\Delta \ll (k_y^2 + k_z^2)^{-1/2}$] the k_o solution can be estimated by Taylor's series expansion of the cotangent term, we get

$$k_o^2 \sim (k_y^2 + k_z^2)/E\Delta. \quad (A.14)$$

The k_x roots of Eq. A.12 can be found graphically as well. A different set of decay rates are associated with these roots; the decay rates are

$$-p^*_{t,l} \approx \eta_s[(l+1/2)\pi/\Delta]^2 \text{ for } l = 1, 2, 3... \quad (A.15)$$

The time scale for which the thin shell approximation is valid is now apparent. If the perturbation vary on a time scale slower than $\Delta/\eta_s(4\Delta/\pi^2)$, all except the lowest order eigenstate for the eddy current will have decayed away. The remaining lowest order eigenstate has current density which is nearly constant in the x direction (i.e., $k_o\Delta \ll 1$).

The solutions for $p_{t,i} \mid_{i=1,2,3...}$ and $p^*_{t,l} \mid_{l=1,2,3...}$, and the $k_o\Delta \ll 1$ condition are valid in the cylindrical geometry as long as the thin shell condition $\Delta \ll (k_\theta^2 + k_z^2)^{-1/2}$ is satified. This is due to the following reasons. If $\Delta \ll (k_\theta^2 + k_z^2)^{-1/2}$ the cylindrical thin shell than approximates a slab, hence the field solutions in the slab must be approximately the same as those in the shell. As for the differences in the vacuum field solutions, switching to the cylindrical geometry will affect the $p_{t,i} \mid_{i=1,2,3...}$, the $p^*_{t,l} \mid_{l=1,2,3...}$, and the $k_o\Delta$ solutions since the evaluation of E will be

affected. From the graphic solutions of k_x shown above, however, we see that the $k_i \mid_{i\neq 0}$ solutions are weakly dependent on the E term if $\Delta \ll (k_\theta^2 + k_z^2)^{-1/2}$. The k_o solution, and hence the decay rate corresponding to its eigenstate, show a greater dependence on the E term than the $k_i \mid_{i\neq 0}$ solutions. (Physically, this implies that the lowest order eigenstate governs the diffusion of magnetic fields into the vacuum, whereas the higher order eigenstates governs diffusion into the slab.) However, the key condition of $k_o\Delta \ll 1$ if $\Delta \ll (k_\theta^2 + k_z^2)^{-1/2}$ remains valid.

The cylindrical thin shell boundary condition can now be derived. If $k_o\Delta \ll 1$, the lowest order eigenstate solution has b_r, j_θ, and j_z roughly constant in the shell (see Eq. A.9). Thus, its possible to apply simple jump conditions on the θ and z components of the magnetic field across the shell (e.g., the jump in b_z is proportional to e_θ in the shell), which in conjunction with Faraday's law and the $\nabla \cdot \mathbf{b} = 0$ condition, leads to the thin shell boundary condition on b_r (Eq. 2.3).

The thin shell boundary condition on j_r, which is needed if there is no insulating layer on the inner surface of the shell, can be derived in the same manner as the boundary condition on b_r. The R field solutions need to be considered in this case. It turns out that on a time scale of $\Delta/\eta_s(\Delta/\pi^2)$ all the transient eigenstate solutions decay away. This does not imply that $j_r = 0$, however; we still need to consider the $\mathbf{e} = \nabla\chi$ solution, where χ is a scalar potential function. This is the electrostatic solution, which by continuity of e_z, e_θ and b_r, leads to the boundary condition on j_r.

$$\left(\frac{a \cdot S V_r}{\gamma(r=a)} - \frac{\beta_s a}{\Delta \gamma(r=a)} \right) j_r = \frac{\partial}{\partial r}(r j_r)\Big|_{r=a} \qquad \text{(A.16)}$$

REFERENCES

[1]M. D. Kruskal, J. L. Johnson, M. B. Gottlieb, and L. M. Goldman, Phys. Fluids **1**, 421 (1958).

[2]M. Tanaka, T. Tuda, and T. Takeda, Nucl. Fusion **13**, 119 (1973).

[3]V. F. Alaksin and S. S. Romanov, Sov. Phys. Tech. Phys. **18**, 734 (1973).

[4]V. F. Alaksin and S. S. Romanov, Sov. Phys. Tech. Phys. **19**, 1171 (1975).

[5]G. F. Nalesso and S. Costa, Nucl. Fusion **20**, 443 (1980).

[6]J. P. Goedbloed, D. Pfirsch, and H. Tasso, Nucl. Fusion **12**, 649 (1972).

[7]C. G. Gimblett, Nucl. Fusion **25**, 617 (1986).

[8]P. M. Morse and H. Feshbach, *Methods of Theoretical Physics*, (McGraw–Hill, New York, 1953), p. 1765.